LASER BEAM SHAPING OPTICAL SYSTEM DESIGN METHODS AND THEIR

APPLICATION IN EDGE-EMITTING SEMICONDUCTOR

LASER-BASED LIDAR SYSTEMS

Except where reference is made to the work of others, the work described in this dissertation is my own or was done in collaboration with my advisory committee. This dissertation does not include proprietary or classified information.

_____
Mert Serkan

Certification of Approval:

_____   _____
Thaddeus A. Roppel   Hulya Kirkici, Chair
Associate Professor   Associate Professor
Electrical and Computer Engineering   Electrical and Computer Engineering

_____   _____
John Y. Hung   Lloyd S. Riggs
Professor   Professor
Electrical and Computer Engineering   Electrical and Computer Engineering

_____
George T. Flowers
Interim Dean
Graduate School

LASER BEAM SHAPING OPTICAL SYSTEM DESIGN METHODS AND THEIR

APPLICATION IN EDGE-EMITTING SEMICONDUCTOR

LASER-BASED LIDAR SYSTEMS

Mert Serkan

A Dissertation

Submitted to

the Graduate Faculty of

Auburn University

in Partial Fulfillment of the

Requirements for the

Degree of

Doctor of Philosophy

Auburn, Alabama
December 17, 2007

LASER BEAM SHAPING OPTICAL SYSTEM DESIGN METHODS AND THEIR

APPLICATION IN EDGE-EMITTING SEMICONDUCTOR

LASER-BASED LIDAR SYSTEMS

Mert Serkan

_____

Signature of Author

_____

Date of Graduation

VITA

Mert Serkan, son of Varol Serkan and Eyyube Sevgi Serkan, was born on February 26, 1979 in Istanbul, Turkey. He graduated from Huseyin Avni Sozen Anatolian High School in 1996. He received the Bachelor of Science degree in Electronics and Telecommunications Engineering from Istanbul Technical University, Turkey in 2000. After graduation, he worked as a Research and Development Engineer in Nortel Networks/Netas for about a year. He started his M. Sc. degree in Satellite Communications and Remote Sensing Graduate Program at Istanbul Technical University in 2001. He worked as a Research Assistant in Satellite Ground Receiving Station at Istanbul Technical University between 2001 and 2003. He earned his M. Sc. degree in 2003 and started his Ph. D. degree at Auburn University, AL in 2003. He worked as a Teaching/Research Assistant at Auburn University between 2003 and 2007.

DISSERTATION ABSTRACT

LASER BEAM SHAPING OPTICAL SYSTEM DESIGN METHODS AND THEIR

APPLICATION IN EDGE-EMITTING SEMICONDUCTOR

LASER-BASED LIDAR SYSTEMS

Mert Serkan

Doctor of Philosophy, December 17, 2007
(M. Sc. Istanbul Technical University, Turkey, 2003)
(B. Sc. Istanbul Technical University, Turkey, 2000)

148 Typed Pages

Directed by Hulya Kirkici

LIDAR (Light Detection And Ranging) systems are employed for numerous applications such as remote sensing, military applications, optical data storage, display technology, and material processing. Furthermore, they are superior to other active remote sensing tools such as RADAR systems, considering their higher accuracy and more precise resolution due to their much shorter wavelengths and narrower beamwidth. Several types of lasers can be utilized as the radiation source of several LIDAR systems. Semiconductor laser-based LIDAR systems have several advantages such as low cost, compactness, broad range of wavelengths, and high PRFs (Pulse Repetition Frequency).

However, semiconductor lasers have different origins and angles of divergence in the two transverse directions, resulting in the inherent astigmatism and elliptical beam shape. Specifically, elliptical beam shape is not desirable for several laser-based applications including LIDAR systems specifically designed to operate in the far-field region. In this dissertation, two mirror-based and two lens-based beam shapers are designed to circularize, collimate, and expand an edge-emitting semiconductor laser beam to a desired beam diameter for possible application in LIDAR systems. Additionally, most laser beams including semiconductor laser beams have Gaussian irradiance distribution. For applications that require uniform illumination of an extended target area, Gaussian irradiance distribution is undesirable. Therefore, a specific beam shaper is designed to transform the irradiance distribution from Gaussian to uniform in addition to circularizing, collimating, and expanding the semiconductor laser beam.

For the design of beam shapers, aperture sizes of the surfaces are preset for desired power transmission and allowed diffraction level, surface parameters of the optical components and the distances between these surfaces are determined. Design equations specific to these beam shaping optical systems are determined using geometrical optics principles. It is also verified that the geometrical optics is a valid approximation to the physical optics for each designed system. The design equations are derived analytically and MATLAB codes are developed to solve for the unknown quantities of the optical systems. ZEMAX and MATLAB software programs are used to analyze the designed systems with particular design examples and the results are presented.

ACKNOWLEDGMENTS

First and foremost the author would like to thank Dr. Hulya Kirkici for her guidance and support. He would like to extend his thanks to Dr. Thaddeus A. Roppel, Dr. John Y. Hung, Dr. Lloyd S. Riggs, and Dr. Anwar Ahmed for their valuable suggestions and constructive comments on his dissertation. He thanks his parents Varol and Eyyube Sevgi and his brother Tevfik Murat for always pushing him in the right direction and for all the years of encouragement. He thanks Yusuf Bahadir Anafarta for his guidance and support. He thanks Selda Taskin for giving him the support, help, and encouragement he needed. His thanks also go to all the professors, classmates, and friends in Auburn.

Style manual or journal used IEEE Transactions on Geoscience and Remote Sensing (together with the style known as "auphd").

Computer software used MS Word.

TABLE OF CONTENTS

LIST OF TABLES

LIST OF FIGURES

xvi

CHAPTER 1

INTRODUCTION

Semiconductor lasers have advantages in some applications over other lasers such as CO_2 and Nd-YAG due to low cost, compactness, electronic compatibility, broad range of wavelengths, and high Pulse Repetition Frequency (PRF) values. However, they have different origins and angles of divergence in the two transverse directions, resulting in the inherent astigmatism and elliptical beam shape, as illustrated in Figure 1.1 (x – perpendicular transverse direction, y – parallel transverse direction). For some applications, this elliptical beam is acceptable. However, when a minimum beam spread is needed in both directions, it becomes necessary to reshape the beam into a circular form. In addition, some applications require a circular laser beam due to the usage of various optical components such as fiber optics.
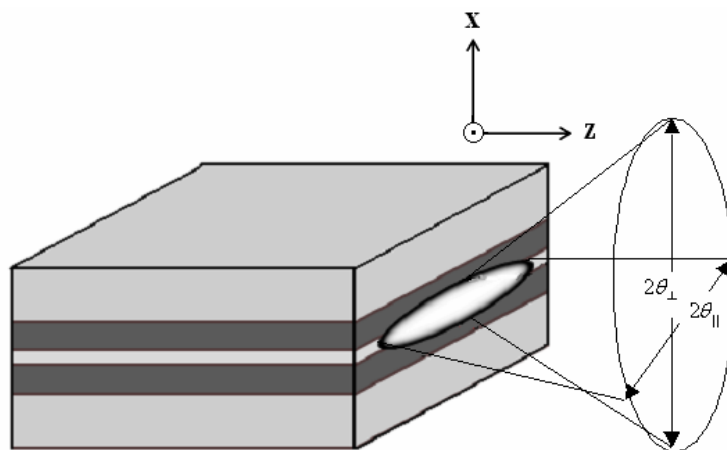
Figure 1.1(a) Free-space radiation pattern of a semiconductor laser with an elliptical beam profile.

parallel beam waist

perpendicular beam waist

astigmatism

elliptical with major axis in the
parallel transverse direction

circular

elliptical with major axis in the
perpendicular transverse direction
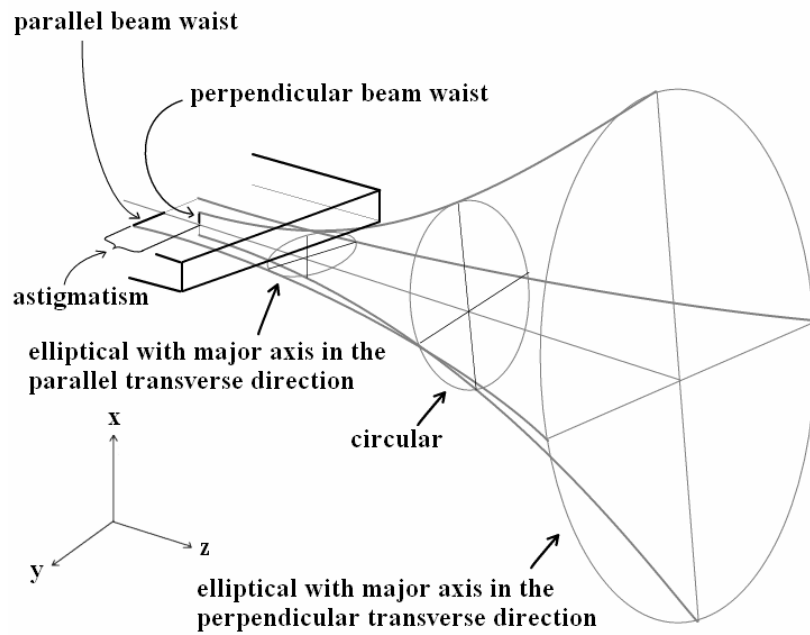
Figure 1.1(b) Illustration of propagation of a semiconductor laser beam.

perpendicular direction

$2w_{0\perp}$

$2\theta_\perp$

astigmatism

$2w_{0\parallel}$

$2\theta_\parallel$

parallel direction
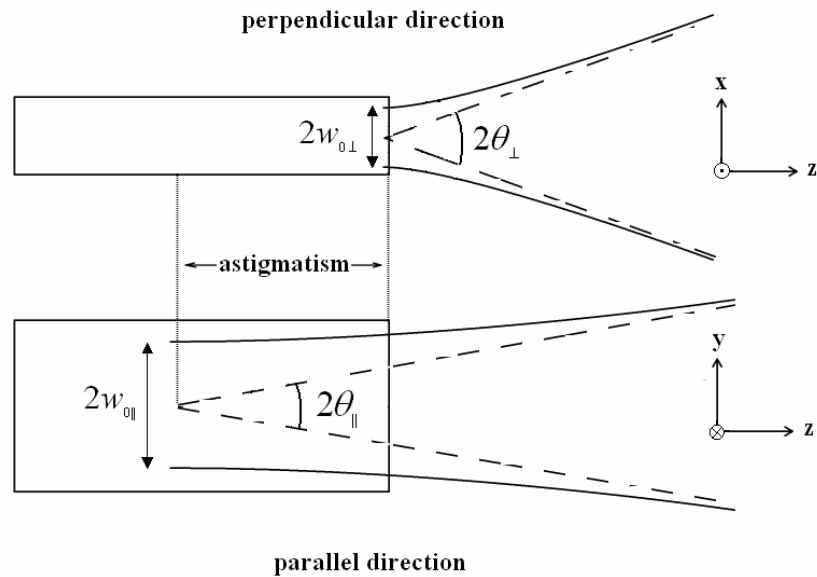
Figure 1.1(c) Semiconductor laser beam in two transverse directions (x – perpendicular, y – parallel) as a function of propagation distance (z - optical axis).

Lasers are used in several scientific and commercial applications. One application that the author is concentrated on in this study is **L**ight **D**etection **A**nd **R**anging (LIDAR) systems. LIDARs can be employed for several applications such as remote sensing, military applications, optical data storage, display technology, and material processing. Nevertheless, they are superior to several other remote sensing tools such as radar systems specifically in atmospheric studies since LIDARs operate at much shorter wavelengths. Hence, they are capable of higher accuracy and more precise resolution than radars perform within the microwave range of the electromagnetic spectrum.

On the other hand, most LIDAR systems are not easily transportable for commercial purposes due to large-scale lasers such as CO_2 or Nd-YAG lasers [1]. These LIDARs that use lasers with kW and MW output power levels are preferred over LIDARS that use semiconductor lasers. High output power levels are essential especially for atmospheric studies due to the intense background noise from sunlight and multiple atmospheric scattering. Recent scientific and technological advances in pulsed semiconductor lasers increase the usage of them more efficiently in LIDARs for other appications. Semiconductor lasers have higher output power levels and higher PRF values nowadays. Semiconductor laser-based LIDARs have also improved light emission efficiency, electronic control compatibility, and reduced system size and cost [2]. However, highly divergent elliptical beam profile of semiconductor lasers is not suitable for LIDAR systems specifically utilized in long-range applications such as atmospheric studies.

For LIDAR systems, the laser beam must be expanded to reduce the beam divergence caused by diffraction. By expansion, the author refers to increasing the beam

waist radius. Expansion also increases the size of the beam spot on the target plane. Thus, a larger area can be scanned within a shorter time.

For most LIDAR systems a circular beam profile is required. This is due to the usage of optical components such as fiber optics. In addition to this, LIDARs might be used in the far-field region [3]. If the laser source has a non-circular beam shape, at the far field the difference between the radii of the beam in the two directions causes highly elliptical beam shape after long-range propagation. Therefore, circularization is essential for such applications.

A minimum beam spread is desired for LIDAR systems that require long-range propagation. For such applications, collimating the beam limits the beam spread. By collimation, the author refers to making the beam parallel in the diffraction limit. A collimated beam also allows the receiver to have low **F**ield-**O**f-**V**iew (FOV) value, which reduces background noise and susceptibility to multiple scattering. To summarize, a beam shaper must be designed to address three aspects before transmitting the beam long distances:

- expansion,
- circularization,
- collimation.

Astigmatism is important for the optical systems designed to focus the laser beam to a small spot [4- 6]. On the contrary, for applications such as most LIDAR systems where the beam is expanded to cm to m levels and collimated, astigmatism in μm levels can be neglected.

4

Several other applications where lasers are used can be listed as display technology, lithography, laser printing, and material processing. Most laser output beams possess Gaussian irradiance distribution and this is undesirable for listed applications since such applications require uniform illumination of an extended target area [7]. Therefore, a beam shaper is required to transform Gaussian irradiance distribution of such beams to uniform distribution. Many studies in the literature cannot be directly applied to highly divergent edge-emitting semiconductor lasers. This is due to the assumption of these studies that the laser beam is already collimated. Moreover, most of them assume that the beam has a circular profile. Therefore, an optical system designed to transform irradiance distribution of such lasers in addition to circularizing, collimating and expanding it to a desired output beam diameter is also of interest in this research.

CHAPTER 2

RESEARCH OBJECTIVES AND DISSERTATION OUTLINE

As stated in the previous chapter, edge-emitting semiconductor lasers have advantages over other lasers such as CO_2 and Nd-YAG such as low cost, compactness, electronic compatibility, broad range of wavelengths, and high Pulse Repetition Frequency (PRF) values in LIDAR systems. However, CO_2 and Nd-YAG are still preferred in LIDAR systems especially employed in atmospheric studies due to the high power levels. With recent advances in semiconductor laser technology, moderately high output power levels and higher PRFs are available making such lasers feasible for LIDAR systems. In addition, advances in detector technology improve the receiver's ability to process the weak return signal. This allows a LIDAR system to operate with the lower power level of pulsed semiconductor lasers.

LIDAR systems utilizing semiconductor lasers are much more compact and easier to transport. However, elliptical beam profile of such lasers must be corrected in long-range applications such as atmospheric studies. An appropriate optical beam shaper must be designed for this purpose. On the other hand, most of the research on beam shaping optics topic is based on other applications such as laser printing and optical data storage. Indeed, these studies are not directly applicable to semiconductor laser-based LIDAR systems. Thus, there is ample room for an academic study for the understanding of this problem and designing beam shapers for semiconductor laser-based LIDAR systems. As

a result, the main contribution of this dissertation is to design the optics required to circularize, collimate, and expand the elliptical semiconductor laser beam, used as the radiation source of a LIDAR sensor, and transmit it towards the target. Atmospheric studies are chosen as the main application type for the design examples throughout the dissertation because beam shaping is a fundamental and inevitable step for edge-emitting semiconductor laser-based LIDAR systems utilized for such applications. On the other hand, several other applications such as material processing, cutting, medical procedures, and optical data processing utilize laser beams, and it is also usually required to reshape the beam for these applications. For these applications, a beam shaper is required to transform Gaussian irradiance distribution of such beams to uniform distribution, as stated in the previous chapter. This type of beam shaper is different than the one designed for LIDAR system, which does not alter the Gaussian beam profile. Both types of beam shapers are discussed and such beam shapers are developed by the author. For some other industrial applications such as CD players and robotics, beam shaping may not be that much of importance due to short distance propagation and low-power level requirements. Therefore, such applications are out of scope of this research.

As mentioned earlier, since semiconductor laser-based LIDAR systems are still not very common, there are not many optical design studies about beam shapers specific to these systems either. Therefore, the author intends to create a scientific resource for feasibility of such LIDAR systems and designing necessary optics for these systems. Two different off-axis mirror systems and two different lens systems are developed to circularize, collimate, and expand the elliptical beam of edge-emitting semiconductor laser-based LIDAR systems are developed. In addition to these systems, a separate lens-

based beam shaper is developed to transform the irradiance distribution of such lasers from Gaussian to uniform in addition to circularizing, collimating, and expanding the beam. Even though this beam shaper is not specifically designed for LIDAR systems, it can still be employed in a LIDAR system where illuminating the receiver detector (or detector array) with a uniform beam is desired, similar to the system discussed in [8]. The author presents the principles and tools used to design these systems explicitly in order to create a guideline for the ones working with similar problems or further improving the proposed designs. The equations specific to these systems are derived analytically and computer package programs such as ZEMAX and MATLAB are utilized to simulate the optical designs. These equations are derived based on optics principles and geometrical relationships. These analytical equations are placed in equation systems and solved with MATLAB codes to determine the parameters of the optical components. The author expects that these beam-shaping systems can be used while manufacturing an edge-emitting semiconductor laser-based LIDAR system and be easily modified to address other issues related to laser beam shaping. These systems can be commercialized as the next step since they will be much more compact and lighter than the conventional LIDARs due to the advantages of semiconductor lasers. The author also expects that this dissertation and the analysis methods developed will be a valuable resource for the scientific community interested in LIDAR systems and/or beam shaper systems.

The background information for this dissertation together with literature survey of beam shaping methods and LIDAR applications is presented in Chapter 3. Basic principles of lasers with an emphasis on semiconductor lasers are introduced in Section 3.1. The details of laser beam physics are not covered here because this research focuses

on the beam shaping methods of edge-emitting semiconductor lasers. The irradiance distribution of such lasers is assumed to have a Gaussian profile. Therefore, Gaussian beam analysis is also presented in this section. The design methods discussed in this dissertation are based on geometrical ray optics approximating the physical optics propagation. As a result of this, physical optics propagation principles are not covered in this section.

Beam shaping might be either circularization, collimation, and expansion of a divergent elliptical beam or transformation of the irradiance distribution to another distribution type such as Gaussian distribution to uniform distribution. Section 3.2 briefly discusses the beam shaping in both senses and provides examples from the literature.

The main application type that this research focuses on is remote sensing using LIDAR systems. Therefore, Section 3.3 is devoted to discussion of such systems, providing an overview and literature review for the LIDAR systems and their applications, including a brief discussion of edge-emitting semiconductor laser based LIDAR system design. An example of a coherent LIDAR system design is also presented in this section.

Chapter 4 presents the general methodology for the design and analysis of the beam shaper systems. Section 4.1 discusses the geometrical ray optics approximation to physical optics propagation. The optical surfaces of the designed systems are mostly designed aspheric surfaces. Therefore, aspheric surfaces and conic sections are briefly discussed in Section 4.2.

ZEMAX and MATLAB software programs are used both in design and analysis of the optical systems discussed in this dissertation. ZEMAX is a software tool for optical design [9, 10]. Section 4.3 discusses how ZEMAX is involved in the design and analysis steps of the optical systems.

As mentioned earlier, two mirror-based systems are developed: an off-axis hyperbolic/parabolic mirror system and an off-axis parabolic mirror system. Both design methods consist of three aspheric mirrors. The design approach and the equations specific to these mirror-based systems are presented in Section 4.4. Two design methods using aspheric lenses are also designed. The first system consists of two aspheric lenses; whereas, the second system has a single aspheric lens. The design approach and the equations specific to the lens-based beam-shaper systems are presented in Section 4.5. Section 4.6 presents the design approach and the equations of the beam shaping system of two aspheric lenses developed to circularize, collimate, and expand a semiconductor laser beam and to transform its irradiance distribution from Gaussian to a uniform distribution.

Chapter 5 provides design examples to the systems presented in Chapter 4. Results of these examples are also presented and discussed. The sixth chapter provides a summary to the design methods presented, concludes this dissertation, and discusses the issues left for future study.

CHAPTER 3

BACKGROUND

This chapter presents the background information for this dissertation together with literature survey of beam shaping methods and LIDAR applications. Basic principles of laser beams and their propagation characteristics are discussed briefly in Section 3.1. Section 3.2 briefly discusses the beam shaping types and methods and provides examples from the literature. Section 3.3 is devoted to discussion of the LIDAR systems. Section 3.3.1 provides an overview and literature review for the LIDAR systems and their applications. In Section 3.3.2, edge-emitting semiconductor laser based LIDAR system design is briefly discussed. An example of a coherent LIDAR system design is also presented in this section.

3.1 Basic Principles of Laser Beams and Their Propagation Characteristics

LASER is the acronym used for "**L**ight **A**mplification by the **S**timulated **E**mission of **R**adiation". Lasers are optical sources that emit coherent, nearly monochromatic, and unidirectional beams [11]. Here, coherent beam term is used for a beam having constant frequency and phase for a significantly long duration. It is nearly monochromatic since no laser beam can have an infinitely narrow linewidth. However, laser beams can be assumed as monochromatic when compared with several other light sources.

Lasers mainly consist of three parts, namely, the active medium, the optical cavity, and the pumping mechanism. The active medium is the part where the lasing starts and sustained in the form of gases, liquids, solids, or semiconductor junctions. The optical cavity is a cavity resonator mostly designed with reflective surfaces to provide the optical feedback mechanism to amplify radiation generated in the active medium. Proper design of the cavity along with the active medium and the pumping mechanism, directly affects the spectral purity and directionality of the laser beam [12]. The pumping medium is responsible for supplying the necessary energy to the active medium to excite the electrons from the ground energy state to a higher energy state.

When the atomic spacing is large in a material, such as in gases, the electron energies are discrete and the energy states are formed. With an increase in the number of neighbor atoms, the number of split energy states is increased while the energy differences in the adjacent states are reduced. In the semiconductor crystals, there are approximately $10^{22}/\text{cm}^3$ atoms, and the spacing of energy states is on the order of 10^{-18} eV. This energy spacing is much smaller than the bandgap of the semiconductor material; therefore, the energy states are considered to be continuous forming energy bands [13].

In order for the lasers to operate, it is necessary to create a population inversion between the valence and conduction bands. Population inversion basically means having more electrons in an upper energy level compared with the number of electrons in a lower energy level [14]. Such a population inversion can be created by external pumping (lasers, electron beams, or flashlamps) or by electron injection (with a PN-junction) [14]. Electrons and photons exchange energy in the absorption and emission steps of lasing such that the total energy is conserved.

This research is interested in the type of semiconductor lasers termed as edge-emitting semiconductor lasers. The output beam of such lasers emerges in the plane of PN-junction throughout a horizontal cleaved construction, as illustrated in Figure 1.1(a). The rectangular slab of semiconductor material has two polished surfaces called cleaved facets, functioning as resonator mirrors. The best method to define such lasers' output beam and propagation is approximating the radiating field as the superposition of fundamental and higher modes, where each mode is most conveniently expressed as the product of a Hermite or a Laguerre polynomial and a Gaussian function [15]. The simplest, and the lowest order mode, is called the fundamental Gaussian beam, and is also the most stable and preferred beam type in many applications. A complete understanding of laser beam propagation requires a treatment based on Maxwell Equations. Therefore, in this section, only the basics of the fundamental Gaussian beam analysis are presented, as presented in [16].

The scalar wave equation for the electric field in free space, which is sufficient to model diffraction and interference, is given by:

$$\nabla^2 E(\boldsymbol{r}, t) + -\frac{1}{c^2} \frac{\partial^2}{\partial t^2} E(\boldsymbol{r}, t) = 0 \qquad (3.1)$$

In order to model monochromacity of the laser beams the solutions to Equation 3.1 considered are in the following form:

$$E(\boldsymbol{r}, t) = \varepsilon(\boldsymbol{r}) e^{-jwt} \qquad (3.2)$$

When Equation 3.2 is substituted in 3.1, the Helmholtz Equation for $\varepsilon(\boldsymbol{r})$ is obtained:

$$\nabla^2 \varepsilon(\boldsymbol{r}) + k^2 \varepsilon(\boldsymbol{r}) = 0 \tag{3.3}$$

where k is the wave number (or phase constant) of the wave.

Ideally, a laser beam propagates as a unidirectional wave with a finite cross-sectional area. However, a spherical wave is not unidirectional and a plane wave has an infinite cross-sectional area. Therefore, neither plane nor spherical waves can be considered as laser beams. Hence, a solution in the form as given in Equation 3.4 is sought:

$$\varepsilon(\boldsymbol{r}) = \varepsilon_0(\boldsymbol{r}) e^{jkz} \tag{3.4}$$

which differs from a plane wave by the fact that its amplitude is not a constant. This equation represents a unidirectional wave with a finite cross-sectional area. The solution in Equation 3.4 must satisfy the Helmholtz Equation given in Equation 3.3. Thus, Equation 3.4 is substituted in Equation 3.3, yielding in the following equation:

$$\left(\frac{\partial^2}{\partial x^2} + \frac{\partial^2}{\partial y^2} + \frac{\partial^2}{\partial z^2} \right) \varepsilon_0(\boldsymbol{r}) e^{jkz} + k^2 \varepsilon_0(\boldsymbol{r}) e^{jkz} = 0 \tag{3.5}$$

$\varepsilon_0(\boldsymbol{r})$ term is called "slowly varying part" and e^{jkz} term is called "rapidly varying part". Slowly varying part means that:

$$\left| \frac{\partial^2 \varepsilon_0}{\partial z^2} \right| << k \left| \frac{\partial \varepsilon_0}{\partial z} \right| \tag{3.6}$$

Using the expression given in Equation 3.6, the following approximation can be made:

$$\frac{\partial^2}{\partial z^2} \varepsilon_0(\boldsymbol{r}) e^{jkz} = \left(\frac{\partial^2 \varepsilon_0}{\partial z^2} + 2jk \frac{\partial \varepsilon_0}{\partial z} - k^2 \varepsilon_0 \right) e^{jkz} \approx \left(2jk \frac{\partial \varepsilon_0}{\partial z} - k^2 \varepsilon_0 \right) e^{jkz} \tag{3.7}$$

, and therefore we have:

$$\left(\frac{\partial^2}{\partial x^2} + \frac{\partial^2}{\partial y^2} + 2jk\frac{\partial}{\partial z} \right)\varepsilon_0(\mathbf{r}) \cong 0 \qquad (3.8)$$

The solutions to Equation 3.8 must be sought. This equation yields to:

$$\nabla_T^2 \varepsilon_0 + 2jk\frac{\partial \varepsilon_0}{\partial z} = 0 \qquad (3.9)$$

which is the paraxial wave equation and $\nabla_T^2 = \dfrac{\partial^2}{\partial x^2} + \dfrac{\partial^2}{\partial y^2}$.

A solution to Equation 3.9 must be sought, having the following form:

$$\varepsilon_0(\mathbf{r}) = Ae^{jk\left(x^2+y^2\right)/2q(z)}e^{jp(z)} \qquad (3.10)$$

where A is a constant and $q(z)$ and $p(z)$ are to be determined.

$q(z)$ is given by:

$$\frac{1}{q(z)} = \frac{1}{R(z)} + \frac{j\lambda}{\pi w^2(z)} \qquad (3.11)$$

The designation $z = 0$ is arbitrary, therefore the plane $z = 0$ is chosen so that R_0 is infinitely large. As a result of this, Equation 3.11 yields to:

$$\frac{1}{q_0} = \frac{j\lambda}{\pi w_0^2} \qquad (3.12)$$

Equation 3.10 is a solution for Equation 3.9 if $p(z)$ and $q(z)$ satisfy:

$$\frac{dq}{dz} = 1 \qquad (3.13)$$

$$\frac{dp}{dz} = \frac{j}{q} \qquad (3.14)$$

These equations have the solutions:

$$q(z) = q_0 + z \qquad (3.15)$$

15

$$p(z) = j \ln\left(\frac{q_0 + z}{q_0}\right) \quad \frac{dp}{dz} = \frac{j}{q}$$ (3.16)

where $q_0 = q(0)$ and it is assumed that $p(0)=0$.

If Equation 3.11 is substituted in Equation 3.10, the following equation is determined:

$$e^{jk\left(x^2+y^2\right)/2q(z)} = e^{jk\left(x^2+y^2\right)/2R(z)}e^{-\left(x^2+y^2\right)/w^2(z)}$$ (3.17)

Solving Equation, 3.15 it is found that:

$$e^{jp(z)} = \frac{1}{1 + z/R_0 + j\lambda z/\pi w_0^2}$$ (3.18)

where R_0 and w_0 are the values of R and w at $z = 0$.

Using Equation 3.15, the following equation can be derived:

$$\frac{1}{q(z)} = \frac{1}{q_0 + z} = \frac{1/q_0}{1 + z(1/q_0)} = \frac{j\lambda/\pi w_0^2}{1 + jz\lambda/\pi w_0^2} = \frac{j\lambda/\pi w_0^2 + 1/z(\lambda z/\pi w_0^2)^2}{1 + (\lambda z/\pi w_0^2)^2}$$ (3.19)

When Equations 3.11 and 3.19 are equated to each other: the "radius of curvature" at an arbitrary point is determined as:

$$R(z) = z + \frac{z_0^2}{z}$$ (3.20)

the spot size (radius) at an arbitrary plane is found as:

$$w(z) = w_0\sqrt{1 + z^2/z_0^2}$$ (3.21)

where z_0 is called the Rayleigh range and given by:

$$z_0 = \frac{\pi w_0^2}{\lambda}$$ (3.22)

$q(z)$ defined in Equation 3.11 is termed as the complex radius of curvature.

16

Substituting Equations 3.20- 3.22 in Equation 3.18, the following equation is determined:

$$e^{jp(z)} = \frac{1}{1 + jz/z_0} = \frac{1}{\sqrt{1 + z^2/z_0^2}} e^{-j\phi(z)}$$ (3.23)

where $\phi(z) = \tan^{-1}(z/z_0)$

Substituting Equations 3.17 and 3.23 in Equation 3.10:

$$\varepsilon_0(r) = \frac{Ae^{-j\phi(z)}}{\sqrt{1 + z^2/z_0^2}} e^{jk(x^2+y^2)/2R(z)} e^{-(x^2+y^2)/w^2(z)}$$ (3.24)

is determined. As a result, the solution to the Helmholtz Equation can be determined as:

$$\varepsilon(r) = \frac{Ae^{j[kz-\phi(z)]}}{\sqrt{1 + z^2/z_0^2}} e^{jk(x^2+y^2)/2R(z)} e^{-(x^2+y^2)/w^2(z)}$$ (3.25)

The plane $z = 0$ is called the beam waist plane and the radius w_0 at this plane is the minimum beam radius. The relationship between the beam spot radius at Rayleigh range and the beam waist radius is related such that:

$$w(z_0) = w_0 \sqrt{2}$$ (3.26)

The smaller the spot radius, the smaller the Rayleigh range, thus the greater the rate of growth of the spot size from the waist with propagation in z direction. The distance equal to $10z_0$ is considered to be the separating plane between the near-field and the far-field regions. The beam approximates to two asymptotic lines in the far-field region. These asymptotic lines intersect the propagation axis forming a virtual point source in the beam waist plane.

Finally, the divergence of a Gaussian beam in the far-field region is given by the beam divergence half angle:

17

$$\theta \approx \frac{w(z)}{z} \approx \frac{w_0}{z_0} = \frac{\lambda}{\pi w_0} \quad , \quad z >> z_0 \qquad (3.27)$$

The characteristic parameters of a Gaussian beam are demonstrated in Figure 3.1.
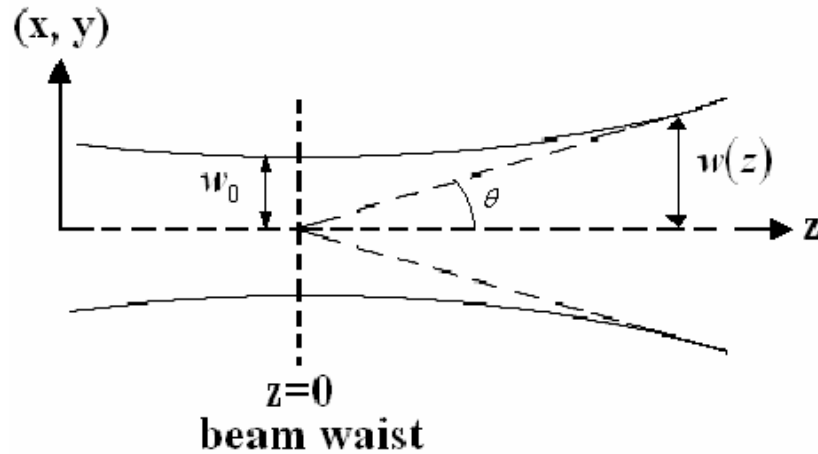
Figure 3.1: The characteristic parameters of a Gaussian beam.

As mentioned earlier, the lowest order transverse mode is the fundamental mode and denoted as TEM_{00} [17].   Higher order modes are expressed as the superposition of fundamental Gaussian function and Laguerre polynomial for lasers with circular symmetry, whereas, the superposition of Gaussian function and Hermite polynomial is used to express lasers with rectangular symmetry. Higher modes are denoted as TEM_{mn} where m = 1, 2, 3, … and n = 1, 2, 3, …The beam spots for modes with circular and rectangular symmetry are displayed in Figure 3.2 and Figure 3.3, respectively [17].
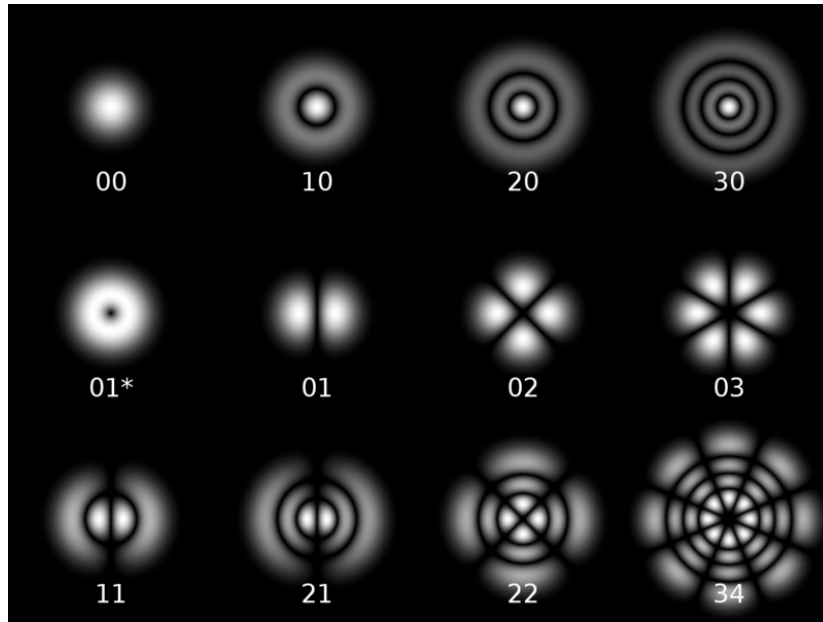
Figure 3.2: Transverse modes for lasers with circular symmetry
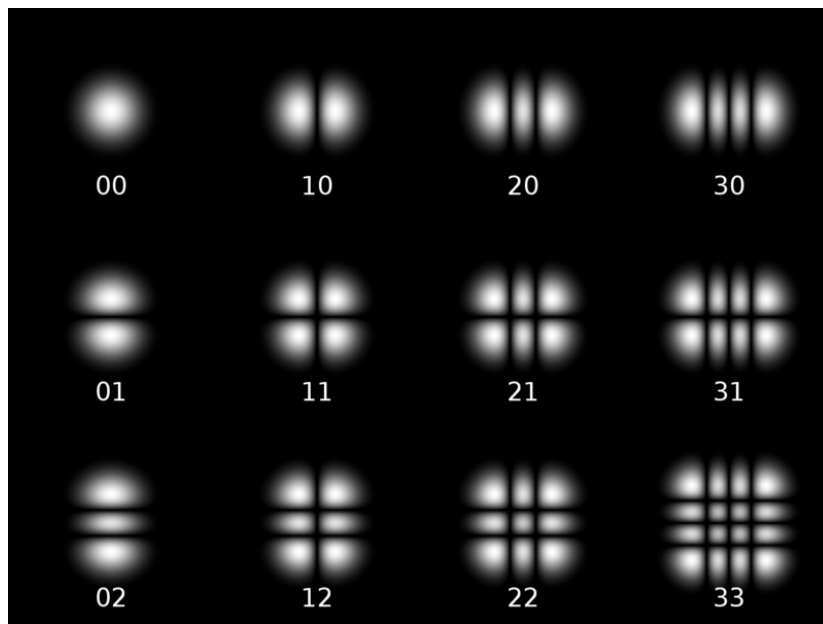
Figure 3.3: Transverse modes for lasers with rectangular symmetry

3.2 Beam Shaping Optical System Design in the General Sense

Beam shaping is basically modifying a laser beam to another form as required by a specific application. This might be circularizing and collimating a divergent elliptical beam or transforming a laser beam's irradiance distribution such as from Gaussian to uniform. These two types of beam shaping may also be handled simultaneously if required.
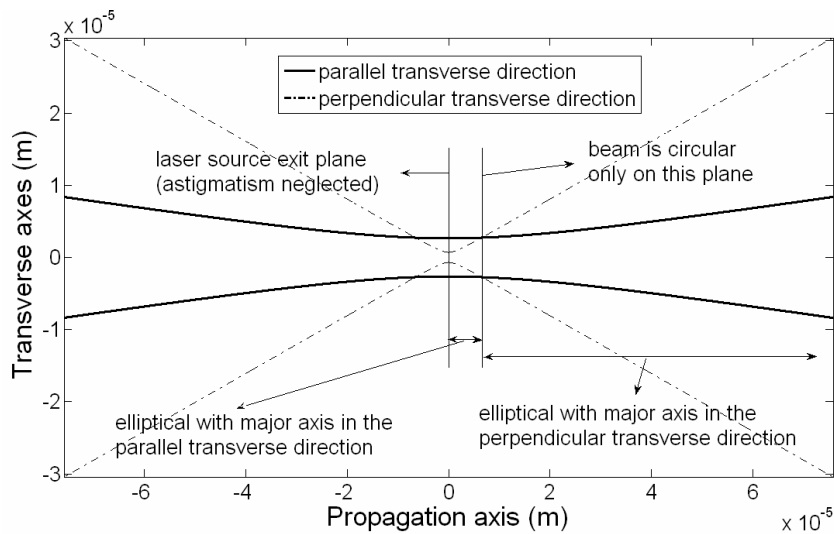
Figure 3.4: Beam profile plot of a laser beam with 46° divergence angle in the perpendicular transverse direction, 12° divergence angle in the parallel transverse direction, and neglected astigmatism.

Edge-emitting semiconductor lasers have inherent astigmatism and elliptical beam profile, as stated earlier. Elliptical beam emitted from the laser source forms a circular beam at a specific target plane and as it further propagates it becomes a beam having an elliptical beam profile again due to the different divergence angles in the two transverse directions (see Figure 3.4). When designing a beam shaper, the divergence angles at the output of the beam shaper must be made equal, satisfying that the beam radii in the two

transverse directions are the same at any arbitrary target plane after propagating through the optical system.

One method to transform an elliptical beam to a circular beam is to use reflective optics such as mirrors. Reflective optics such as mirrors is preferred over the refractive optics such as lenses in some cases to avoid light feedback to the laser due to imperfect antireflection coatings used in refractive systems [18]. In these instances, the mirrors are designed as off-axis mirrors to avoid obscuration through the system. Two different mirror systems, off-axis hyperbolic/parabolic and off-axis parabolic mirror systems for possible applications in LIDAR systems have been investigated [19].

Refractive optics might be preferred to reflective optics in some cases because it is possible to design an on-axis lens transmitter / receiver system without obscuration caused the optical components. A "cruciform" cylindrical lens, which is a combination of two separate cylindrical lenses with their symmetry axes perpendicular to one another, developed for this purpose has been presented in [20]. Also in [21], a pair of cylindrical lenses is crossed to control the focus and the length of the image of the source. After traveling through this optical system, the diverging laser beam becomes an effectively thin plane of light. The cylindrical lenses are mounted so as to be rotatable simultaneously or with respect to each other. A single aspherical lens approach has also been used for circularization and collimation purposes in [22]. In [23], two optical system designs using aspherical lenses for possible application in LIDAR systems are presented. The first system consists of two lenses; whereas, the second one has a single aspherical lens.

21

Another widely used method is to employ an anamorphic prism pair [24]. In this case, the beam entering the prism is collimated and the prism pair serves to change the beamwidth in one transverse direction to make the beamwidth equal in both transverse directions, thus, circularizing the beam. Depending on the orientation of the prisms, the beam size may be either reduced or expanded and the amount of change is variable depending on the angular position of the prisms.

Both reflective [25– 27] and refractive [7, 27- 29] beam shapers to transform the beam's irradiance profile to a different profile have been proposed in the literature. In most of these studies, the input beam is assumed to be a collimated Gaussian beam and the irradiance distribution is converted to uniform distribution. Moreover, the refractive systems discussed in these studies assume that the input beam has a circular profile having the same beam radius and divergence angle values in the two transverse directions [7, 27- 29]. In [30], a two aspheric lens-based beam shaper is presented to convert the Gaussian irradiance distribution of an elliptically divergent edge-emitting semiconductor laser beam into a uniform-square distribution while circularizing and collimating it. The output beam radius is also expanded to a desired value.

Several analytical functions with a uniform central region to an almost null region have been studied in the literature [31]. The most common ones are Super Gaussian, Flattened Gaussian, and Fermi-Dirac functions. These functions allow for a gradual transition from the central uniform intensity region of the output beam to a null region at the edge of the beam, reducing the diffraction effects in regions of sharply changing intensity. The diffraction effects become more and more significant as the beam propagates after exiting the beam shaper.

3.3 Literature Review

3.3.1 LIDAR Applications

LIDAR systems are used in numerous remote-sensing applications. Only a few of them are discussed here. One of the main application areas of LIDAR systems is atmospheric research such as measuring the chemical constituents in the atmosphere [32]. **DI**fferential-**A**bsorption **L**IDAR (DIAL) systems are based on the fact that the absorption of light by the gases and particles in the atmosphere is different at different wavelengths [33]. This type of LIDAR uses two different laser wavelengths one of which is absorbed by the target particle, termed as the "on wavelength;" whereas, the other one is not absorbed and is termed as the "off wavelength". The wavelength separation between the on and off wavelengths is minimized to avoid differences in the atmospheric backscatter at the two wavelengths [34]. The returned signals at both wavelengths are compared in intensity to determine the concentration of the target. It is mainly used to measure the concentration of ozone, water vapor, and aerosols.

Another common atmospheric application of LIDAR systems is measurement of the wind velocity. In order to measure the velocity of an arbitrary target, Doppler LIDAR is utilized, operating based on the Doppler principle [35]. There is an increase in the wavelength if the target is moving away from the LIDAR whereas the wavelength is decreased if the target is moving towards the LIDAR. The wind velocity is measured by measuring the Doppler shifts caused by dust and aerosol particles carried by the wind. The coherent (heterodyning) LIDAR is a receiver technique that can be applied to determine the Doppler shift as explained in [36]. This technique does not require

determining the full spectrum of the returned signal; instead Doppler shift of only the peak frequency is measured. This is advantageous to non-coherent receiver systems since only a few photons are enough for measurement. The heterodyning technique is utilized at the detector, where the returned light is mixed with the beam from "the local oscillator" (LO). The frequency difference, caused by the Doppler shift, provides the wind velocity. Numerous studies of coherent LIDAR can be found in the literature [1, 37- 42].

The detection mechanism utilized at the receiver is as of importance as the type of the detector. By combining a weak optical signal with a strong, frequency-stable Local Oscillator (LO) laser beam, radio frequency beats are produced at the frequency difference between the two optical beams [40]. A LIDAR employing such coherent (heterodyne) detection is called a coherent LIDAR, as stated earlier. Compared with incoherent (direct) detection LIDARs, coherent detection LIDAR has the advantages of greater sensitivity and the straightforward measurement of the velocity of a target [41].

The platform choice of a LIDAR system depends on the application and the laser type. Most LIDAR systems are placed on the ground or airborne platforms. On the other hand, the first spaceborne LIDAR system designed for atmospheric studies was named **L**idar **I**n-space **T**echnology **E**xperiment (LITE) [43] and was designed with the capability to make measurements of aerosols and specifically clouds in the stratosphere and troposphere [44]. Due to their better space and time resolution characteristics than the other satellite-based passive remote sensing tools possess, LIDARs are excellent systems to investigate the clouds. By enabling accurate measurement of cloud height and

structure, LITE provides the necessary means for the numerical models used in climate study and weather forecasting [45].

In another study, a CO_2 LIDAR, operating at 10.59 μm, is used since multiple scattering occurring in clouds is eliminated [46]. The sensitivity of the LIDAR is not altered by natural background light because of its extremely narrow optical passband. This LIDAR is mainly used to measure the drop size distribution in water clouds, averaged over the penetration depth of the LIDAR. Further, it is shown in [47] that a longer wavelength covers a wider range of size distributions. Another application is discriminating between water and ice clouds. The CO_2 LIDAR uses the ratio of backscattered signal at two wavelengths for this discrimination process.

LIDAR systems are also suitable for the spatially continuous measurement of air pollution, and it is desirable to develop a LIDAR which can cover a wide area [48]. However, airborne LIDAR is not useful for the instantaneous measurement over an area and its running cost is great compared to a ground-based LIDAR. For these reasons, a large-scale station-type LIDAR is developed [48]. This LIDAR has a wide-area observation capability and it can respond to rapidly varying phenomena such as stack plume dispersion by the use of a pulsed laser with a high PRF.

In general, most LIDARs and conventional radars are based on similar fundamentals. The biggest advantage of the LIDAR systems is that the LIDARs operate at much shorter wavelengths so that they are capable of higher accuracy and more precise resolution than the radars. This is the main reason that the LIDARs are preferred to radars in atmospheric studies that especially include interaction with significantly small particles. LIDARs can also be operated as multi-wavelength tools as radars do. In [49], a LIDAR

working at 7 wavelengths within the range $0.38 - 1.0$ μm is presented. This system is used to determine the atmospheric aerosols at different regions such as continental background and industrial areas, deserts, and ocean regions. The obtained data are used in radiation transfer calculations for the atmosphere to improve atmosphere correction methods in observing the Earth from satellites and aircrafts.

There are several applications of LIDAR systems other than atmospheric research. One application type is the **L**aser **R**ange**F**inder (LRF), which displays the distance of a target [50]. A low-cost, handheld LRF system based on a pulsed GaAs laser diode for automotive speed detection and law enforcement is presented in [51]. LRF systems have several advantages over microwave Doppler police radar systems such as narrow angle beam adjustment with proper optical system design and fewer false speed-readings. In addition to this, they are harder to detect than the radar detectors are. It is shown in [52] that the laser diode LIDAR systems are also promising as sensors for autonomous targeting guided weapons due to their ranging and 3D profiling capabilities improving target recognition and reducing false alarms. Profiling also permits determination of optimum aim point on the target improving the destruction capability.

LIDAR systems can also be used in on-board automotive applications for monitoring the target distance to the host vehicle and their relative velocities [53]. These systems can be utilized in **A**daptive **C**ruise **C**ontrol (ACC), **C**ollision **W**arning / **C**ollision **A**voidance (CW/CA), **L**ane **K**eeping **A**ssistance (LKA), **P**re-**C**rash **S**ensing (PCS), pedestrian detection, reversing aid, and blind zone checking applications. Each system needs to recognize different targets such as the relevant vehicle for ACC, the lane mark for LKA, and in-front objects for PCS. Moreover, LIDAR and **G**lobal **P**ositioning

26

System (GPS) units can be utilized in coordination for highly accurate automatic navigation [54].

LIDAR systems are also used in several civil planning applications. In [55], an automatic LIDAR based approach is proposed to update building information in a GIS (Geographic Information System) database in a dense urban area. An up-to-date building inventory database is a crucial requirement for a reliable damage assessment specifically for earthquake-prone and dynamically changing urban areas such as Tokyo and Istanbul. Aerial photography for these urban areas has unavoidable drawbacks such as shadows of tall buildings over the scene and leaning of the buildings due to the perspective projection. An important application is to carry out two LIDAR surveying flights before and after an earthquake, assessing the damage by a change detection process. In addition, reconstruction of building geometry in an urban environment has several other important applications such as urban planning, surveillance, wireless network planning, and virtual tourism [56].

In [57], two airborne LIDAR systems are utilized for ocean and terrain remote sensing purposes. In one configuration, the LIDAR uses two laser transmitters with different wavelengths to perform experiments over the ocean, and in the other only one transmitter is used to perform experiments over the terrain. During airborne experiments, the laser pulse time-of-flight information, as a function of the LIDAR platform position, are used to derive 2-D ocean and land profiles.

Airborne LIDAR bathymetry has also proven its worth as a hydrographic survey tool [58]. Airborne LIDAR bathymetry is especially superior to conventional methods in shallow water regions that are costly, hazardous, and time consuming for ship operations.

Water depth is calculated from the time difference of laser returns reflected from the sea and seabed. In most systems, an infrared transmitter is used for surface detection whereas a blue-green transmitter is utilized for seabed detection.

Scanning **H**ydrographic **O**perational **A**irborne **L**IDAR **S**urvey (SHOALS) system, including a bathymetric LIDAR component, a topographic LIDAR component, and a digital imagery capability, produces high-density measurements of the coastal zone. This enables engineers and scientists to quantify volumes of navigation channel shoaling, track movement of sand placed for beach nourishment, aid in coral reef mapping, and provide depths and navigation hazard locations for nautical charting [59]. Another application, observing and characterizing the spectral behavior of sea ice roughness using **A**irborne **T**opographic **M**apper (ATM) LIDAR system, is defined in [60]. Surface roughness is a basic input for the classification of the sea ice development stages. The ATM LIDAR measures the round-trip travel time of the laser pulse between the aircraft and the surface, and combines this information with GPS and on-board laser gyro. Height distributions and roughness spectral densities are derived from surface profiles measured over a variety of sea ice types.

A pulsed laser-based LIDAR together with a GPS and an **I**nertial **N**avigation **S**ystem (INS) unit provides a very efficient remote sensing imaging tool. In [61], a pulsed laser beam is directed out of the aircraft and when this laser pulse is intercepted by a target on earth, it is reflected back to the aircraft. The time interval between the laser pulse leaving the aircraft and reflecting from the target back to the sensor is measured very accurately. In post-flight data processing, the time interval measurements are converted to distance and the calculations are finalized along with the data from the GPS and the INS units.

The GPS unit determines the aircraft longitude, latitude and altitude; whereas, the INS unit determines the aircraft pitch, yaw, and roll providing the laser beam exit geometry relative to the earth coordinates. Laser pulses may reflect from trees or penetrate holes in the canopy and reflected from the ground level. Remote sensing techniques that utilize such LIDAR systems are proved to provide unique data on forest canopy geometry and subcanopy topography [62]. Most remote sensing systems, although providing images of the horizontal organization of canopies, do not provide direct information on the vertical distribution of canopy elements. In this study, a 3-D model is developed to understand the relation between canopy structure and the LIDAR return signal.

Another important application of LIDAR systems is the vegetation status control. Fluorescence LIDAR is an efficient tool used for this purpose giving information about stresses [63]. Vegetation fluorescence is due to the pigments enclosed in the leaf and mainly clorophyll is engaged in the complex electron-exchange, which is the basis of photosynthesis. The resulting spectrum depends on the plant status allowing information extraction on the content of the leaf pigments and the plant health.

In addition to vegetation studies, fluorescence LIDAR systems are also used to investigate oil pollution at sea along with passive hyperspectral imagery [64]. **S**ynthetic **A**perture **R**adar (SAR) tool is mainly used in oil pollution detection based on radiometric properties induced by oil slicks in the resultant images [65]. However, this method suffers from high false detection rates due to environmental parameters such as sea state and wind that can induce similar radiometric properties as oil spills do in SAR images. Location, extent, and volume of the spilled oil and its spatial distribution are the mainly sought parameters. Data fusion from hyperspectral imagery and fluorescence LIDAR

sensors allows the high-resolution spatial distribution of oil thickness to be geographically mapped.

3.3.2 LIDAR System Design

Even though LIDAR systems are efficient tools for applications such as environmental and atmospheric remote sensing, they are not easily transportable for commercial purposes [1]. On the other hand, recent technological advances in edge-emitting semiconductor lasers and detectors permit realization of low cost, easily transportable, and eye-safe LIDARs [66]. Such lasers also offer the advantage of several available wavelengths for the LIDAR operation. Tuning in to several wavelengths can be accomplished by varying the bulk temperature or the injected current into the active junction of the laser [67].

A coherent edge-emitting semiconductor lased-based Doppler LIDAR system is chosen as a design example in this section, as shown with a block diagram in Figure 3.5.
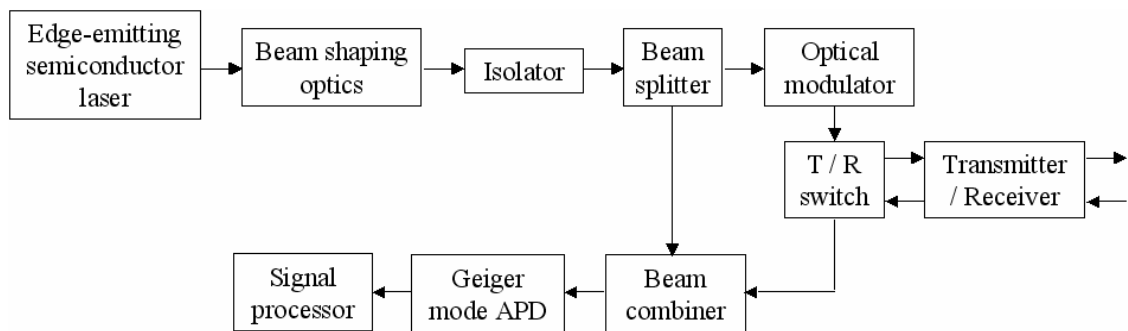
Figure 3.5: Block diagram of a coherent edge-emitting semiconductor laser based Doppler LIDAR system design example.

Most LIDAR systems make use of μJ level pulse energies and PRFs of several thousand Hertz [68]. While the eye-safe maximum permissible exposure levels for

visible and near infrared wavelengths are quite low, eye-safety can be achieved by restricting pulse energies to about a μJ level or even less and expanding the laser beam to a diameter of several centimeters [69]. The low pulse energy permits transmitted beam energy densities that are within the eye safety standards. The reduced signal level drawback due to low transmitted pulse energies is overcome by operating at higher PRFs. Many pulses are averaged in reasonable time periods provided that the lasers can be operated with kHz or higher PRFs. The energy of the beam is further reduced while it propagates through the atmosphere. As a result, the return signal is generally weak and can be best detected by photon counting and summing Avalanche Photodiode Detectors (APD) operating in the Geiger mode; whereas, most conventional methods employed bulky Photo-Multiplier Tube (PMT) detectors with low quantum efficiencies.

A photodiode is basically a semiconductor diode with a p-i-n structure that functions as a light sensor. It can be used either with zero bias (photovoltaic mode) or reverse bias (photoconductive mode). An APD is a special type of photodiode that amplifies the photocurrent via an electron avalanche process [70]. A larger reverse bias voltage generates a larger gain with the cost of increased noise level. Furthermore, the detectors, based on a single photon avalanche diode operating in Geiger mode, utilize avalanche multiplication to enhance detection of the returned LIDAR light [71]. In Geiger mode, the diode is biased a few volts above the breakdown voltage. When a free carrier is generated, it is accelerated and a large current surge is generated by impact ionization. The current reaches saturation for a single-generated carrier [72]. Since the absorption of a photon results in the generation of an electron hole pair, the start of a breakdown indicates the absorption of a photon [73].

31

Even though APDs are quite effective with weak return signals, they have a small active area that might not be sufficient for many applications. In order to enlarge the active area of the detectors and enhance their sensitivity for LIDAR applications, arrays of Geiger-mode APDs might also be integrated [74]. Two other drawbacks of the Geiger-mode APDs are that they need a finite reset time after triggering and that the carriers are generated not only by the signal but also by dark currents and background radiation, sometimes killing the detector before the returned pulse reaches the detector.

Transmitter / receiver choice for a LIDAR system is also of great importance. Most LIDAR systems employ a single optical system used for both transmitting and receiving the laser beam. This optical system must be designed to satisfy the required output beam characteristics for LIDARs using edge-emitting semiconductor lasers. For LIDARs using edge-emitting semiconductor lasers, circularization is required since an elliptical beam profile is not appropriate for an optical system that employs rotationally symmetric optical components and / or fiber optics. Besides this, most LIDAR systems transmit the laser pulses in the far field. Thus, ellipticity of the laser beam would cause highly elliptical footprint on the target plane after long distance propagation. Collimation is necessary since minimum beam spread is required for most LIDAR systems operating at high altitudes. In addition to this, collimation allows the receiver to have low Field of View values. This is required especially for LIDAR systems utilized in atmospheric studies since a receiver with a low FOV value collects less background noise and is less susceptible to multiple scattering caused by the atmosphere. Finally, expansion is needed to reduce the beam divergence caused by diffraction (the minimum beam divergence angle in the diffraction-limit is reduced with increasing beam waist radius). Expansion is

also required to achieve eye-safety without significantly reducing the total transmitted power and larger target area scanning as well.

On the other hand, beam shaping optics and transmitter optics might also be chosen as separate units. This is especially required for coherent LIDAR systems since a portion of the laser source beam is split up with a beam splitter and used as the LO beam. Moreover, the return signal might be further propagated to the detector unit with fiber optics or other optical components. There are also systems with separate transmitter and receiver units, as discussed in the literature [66].

The wavelength choice of a LIDAR system depends on the application type. For instance, infrared region is mostly preferred in atmospheric studies since most gases and atmospheric particles have strong absorption bands in this region. (The atmosphere contains certain gases whose absorption resonances are so strong that some spectral regions are nearly opaque.) One particular example is that the 700 – 900 nm region is useful for atmospheric water vapor measurements [67].

CHAPTER 4

METHODOLOGY

This chapter presents the general methodology for the design and analysis of the beam shaper systems. Section 4.1 discusses the geometrical ray optics approximation to physical optics propagation. The optical surfaces of the designed systems are mostly designed aspheric surfaces. Therefore, aspheric surfaces and conic sections are briefly discussed in Section 4.2. Section 4.3 discusses how ZEMAX is involved in the design and analysis steps of the optical systems. Section 4.4, Section 4.5, and Section 4.6 present the design approaches and the equations specific to the developed beam shapers.

4.1 Geometrical Ray Optics Approximation to Physical Optics Propagation

Optical design of a beam shaper can be achieved using either physical or geometrical ray optics [75]. It is customary to design an optical system with geometrical ray optics instead of Gaussian beam analysis when ray optics is a good approximation to the physical optics beam propagation. Rays generally characterize the direction of the flow or propagation of radiant energy, except near the focus or an edge point where interference and diffraction takes place. Thus, a ray is a mathematical concept rather than a physical entity. They may also be defined as lines normal to the geometrical wavefront of a beam. As an analogy, the direction of radiant energy propagation is given by the Poynting vector in the electromagnetic theory [76].

The amount of divergence or convergence of a laser beam is measured by the divergence angle, which is the angle subtended by the $1/e^2$ asymptotes of the beam irradiance profile [12]. These asymptotes approach the real beam in the far field, which is defined with the Rayleigh range. In the far field, for $z \gg z_0$, the waves approximate to two $1/e^2$ rays emanating from a point source centered at the waist [77] as shown in Figure 1.1(b). In addition, the author also calculates a dimensionless parameter, β, which provides a quantitative measure of the diffraction effects and the validity of the geometrical ray optics design [76]. This parameter is defined as:

$$\beta = \frac{2\pi w_i w_o}{d\lambda},$$

(4.1)

where w_i, w_o, d, and λ are the incoming beam radius, the beam radius at the target plane, the distance between the optical component and the target plane, and the wavelength of the laser beam, respectively. This equation is derived for simple geometries such as a circle. In general, for $\beta \gg 1$, the diffraction effects are negligible.

Designing optical systems based on geometrical ray optics approach involves the laws of reflection and refraction, Snell's Law, ray tracing techniques, conservation of energy within a bundle of rays, and the constant optical path length conditions. The constant optical path length condition is based on Fermat's Principle, which states that each ray follows the path of shortest time passing through an optical system [78].

4.2 Aspheric Surfaces and Their Usage in Beam Shaping Optical Systems

The design methods that will be discussed in this dissertation basically consist of lens and mirror design. These lens and mirror surface functions are mostly chosen to be conic sections such as a parabola, a hyperbola, or an ellipse, rather than spherical surfaces. This reduces the aberrations caused by spherical surfaces [79]. Conic sections are basically aspheric surfaces defined with radius of curvature and conic constant parameters. In general, an aspheric surface can also be defined with even polynomial deformation terms together with radius of curvature and conic constant values. These polynomial terms increase the accuracy of the representative surface function. However, these even aspheric surfaces are harder to optimize and manufacture than conic sections. In this section the mathematical equations for these conic sections are explained here briefly [79, 80].

The focal length or the power of a spherical optical surface is defined by the radius of curvature of the surface, which is correct only for paraxial rays. As the angle of the rays with the propagation axis increases, this paraxial refraction equation does not give accurate results. Due to this inaccuracy, a spherical surface aberrates a beam with high field angle. The use of an aspheric surface permits selective variation in the refractive power of the surface as a function of the coordinate location, reducing the aberrations induced.

The most common general aspheric can be described as a power-series departure from a simple base surface, such as a sphere. The base surface may be a conic section too, but the aspheric departure is generally defined relative to a spherical reference surface with the same radius of curvature.

An important parameter of an optical surface is the "surface sag", which is illustrated in Figure 4.1, as reproduced from [81]. The exact definition of surface sag is given by:

$$\text{sag} = R - \sqrt{R^2 - y^2} \qquad (4.2)$$
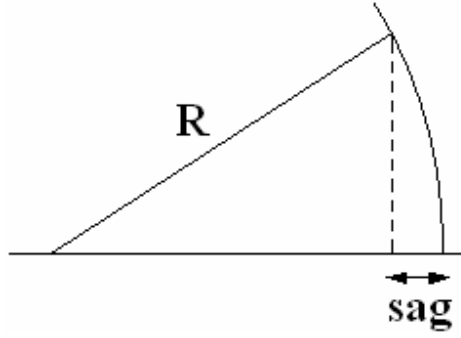
Figure 4.1: Illustration of the definition of surface sag.

The general surface equation for an even aspheric surfaces is given by:

$$z_s = \frac{Cr^2}{1 + \sqrt{1 - (1+K)C^2 r^2}} + \sum_{i=1}^{N} A_{2i} r^{2i} , \qquad (4.3)$$

where z_s is the sag in the direction of the propagation , r is the coordinate in one of the transverse directions, C is the curvature (the reciprocal of the radius of curvature), K is the conic constant, and A_{2i} are the coefficients of the polynomial deformation terms. K and A_{2i} can have several solutions which are dependent on each other. Generally, $i = 1$ is not used and $i = 2, 3, 4, \ldots, N$ are used where $2N$ is the polynomial term with the highest degree for a particular even aspheric surface. However, from a numerical point of view, it is desirable to use the least number of deformation terms meaning that the surface shape is closer to a conic section, which will also simplify the surface manufacturing.

A special class of aspheric surfaces is the conic sections, where all the polynomial deformation terms are equal to 0; whereas, the conic constant is not equal to zero. For a hyperbola $K < -1$, for a parabola $K = -1$, and for an ellipse $K > 0$ (sometimes referred to as oblate ellipse [81]) or $-1 < K < 0$ (sometimes referred to as prolate ellipse [81]). The conic sections can be described in a closed form by the sag formula given by Equation 4.4. The mathematical details of conic sections can be found in [81].

$$z_s = \frac{Cr^2}{1 + \sqrt{1 - (1+K)C^2 r^2}} \tag{4.4}$$

4.3 Implementation of ZEMAX in Design and Analysis

ZEMAX is a software tool for optical design [9, 10]. It contains features and tools to design, optimize, and analyze any optical system. This software along with MATLAB is used for both design and analysis purposes. In addition to geometrical ray tracing techniques, ZEMAX supports physical optics for laser beam propagation. The author is mainly interested in sequential ray tracing to model the optical systems where light travels from one surface to the next in a defined order. If needed, ZEMAX also supports non-sequential ray tracing, which is a technique for tracing rays in systems where there are multiple optical paths. ZEMAX can be further used for optimization of the system parameters determined with analytical calculations, and codes created with MATLAB.

If a surface is a rotationally symmetric surface, it is defined by a "Standard" surface type in ZEMAX lens data editor; whereas, the cylindrical surfaces are defined with "Toroidal" or "Biconic" surface types. The designs that are discussed in this dissertation do not contain any physical apertures other than the mirror and lens surfaces for the

design methods (will be discussed in the following chapter) so that the "Stop Surface" option of ZEMAX is chosen to be at the vertex of the first mirror surface in the lens data editor. Radius and conic constants of the surfaces and thickness values between each surface are calculated analytically and inserted in this editor. For spherical surfaces, radius of curvature is directly the radius of the surface and the conic constant equals to 0. For aspheric surfaces, the calculations of the values of radius of curvature and conic constant are directly determined by the surface parameters. With ZEMAX, it is also possible to define polynomial deformation terms for even aspheric surfaces.

For visualization purposes, several rays are traced through the optical system. Most of the designs include cylindrical surfaces requiring different ray tracing parameters. Therefore, rays are traced in parallel and perpendicular directions separately. Input values of the "Entrance Pupil Diameter" and the "Apodization Factor" in the General System Dialog Box of ZEMAX specify the geometrical rays representing the laser beam. Since Entrance Pupil Diameter values are different in the parallel and perpendicular transverse directions, multi-configuration property of ZEMAX is used for that value. The value of the "Entrance Pupil Diameter" is calculated separately for both directions. The "Apodization Factor" refers to the rate of decrease of the beam amplitude (or intensity) as a function of radial pupil coordinate, and is the same in both directions. The beam amplitude is normalized to unity at the center of the pupil in ZEMAX. The amplitude at the other points in the entrance pupil is given by:

$$A(\rho) = e^{-G\rho^2} , \tag{4.5}$$

where G and ρ are the "Apodization Factor" and the normalized pupil coordinate at the "Stop Surface" respectively. ρ is equal to zero at the center of the "Stop Surface" and 1

at the margin of the "Stop Surface". Therefore, if G is equal to 1, then the beam amplitude falls to the $1/e$ value (intensity falls to the $1/e^2$ value) at the margin of the "Stop Surface". For instance, approximately 98% energy transmission corresponds to G = 1.96. For accurate geometrical ray representation of the beam, the value of the "Entrance Pupil Diameter" is then calculated using the equation below:

$$EPD = \frac{2w_{st}}{\sqrt{1/G}},$$ (4.6)

where EPD and w_{st} are the "Entrance Pupil Diameter" and the beam radius at the "Stop Surface" respectively. For a fundamental TEM_{00} Gaussian beam, the spot size at a particular propagation distance and far field divergence angle are determined by Equations 3.21 and 3.27. As a result, the w_{st} and the EPD are calculated for both directions separately using Equations 3.21, 3.22, and 4.6.

The parameter β, defined in Section 4.1 can be calculated easier with the help of ZEMAX Analysis – Calculations – Ray Trace tool for an off-axis system design simplifying the calculation of path lengths between consecutive surfaces. The rays representing the center of the beam incident on the center of each surface are referred to as the "chief rays", as mentioned earlier. The chief ray is traced by setting the value of the "Px" and "Py" (the normalized pupil coordinates in the x and y axes respectively) to zero in the settings menu of this tool window. The "Stop Surface" "Semi-Diameter" value must be set automatically by ZEMAX in the lens data editor allowing $1/e^2$ rays to pass through this surface. The path lengths from one surface to the next surface are displayed in this analysis window. These path length values provide the parameter d in

Equation 4.1 for each surface. In an on-axis optical system, the path length of the beam between two consecutive surfaces is simply equal to the distance between the vertex points of these surfaces. Therefore, Ray Trace tool is not necessary for on-axis systems.

Analysis – Physical Optics Propagation tool can also be used to assess the output beam. It must not be forgotten that the results of this tool tend to be inaccurate as the divergence angle of the laser beam is increased.

4.4 Off-Axis Mirror-Based Optical System Design for Circularization, Collimation, and Expansion of Elliptical Laser Beams

4.4.1 Overview and Design Approach

Two optical system design methods for beam circularization, collimation, and expansion of the beam of an edge-emitting semiconductor laser are presented. These three aspects can be managed simultaneously or separately by several individual optical components. Two different optical mirror systems are investigated: an off-axis hyperbolic/parabolic mirror system and an off-axis parabolic mirror system. Both design methods consist of three aspheric mirrors as shown schematically in Figure 4.2. The symbols i, j, and k (=1, 2, 3, 4, 5) denote the rays from the laser source to the first mirror, from the first mirror to the second mirror, and from the second mirror to the third mirror, respectively.
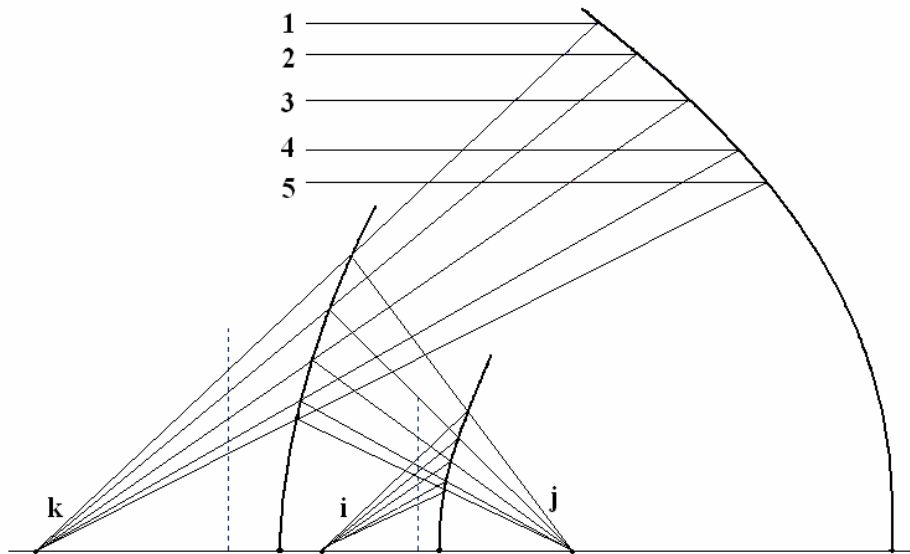
Figure 4.2: Illustration of the general design approach.

In both design methods, the beam is circularized and expanded simultaneously at first, then collimated later. Circularization and expansion steps are accomplished with two cylindrical hyperbolic off-axis mirrors for the first design method; whereas, two cylindrical parabolic off-axis mirrors are used for the second design method for this purpose. A rotationally symmetric off-axis parabolic mirror is employed for collimation step in both design methods.

In the first design method, cylindrical mirror parameters are attuned to expand the beam further in the parallel transverse direction to have the same divergence angle as in the perpendicular transverse direction. In the second method, they are attuned to reduce the beam divergence angle in the perpendicular transverse direction to have the same value as in the parallel transverse direction. One should note that the divergence of a beam can not be eliminated entirely in an optical system; thus, it is not possible to have a

perfectly parallel beam. In this dissertation, the term "collimated beam" refers to a beam with a significantly reduced divergence angle, approaching the diffraction limit.

Most imaging systems are designed with on-axis components to prevent off-axis aberrations. In this design method, however, an off-axis design approach is used and all the analytical equations are derived accordingly rather than using solely paraxial ray optics [18]. The aberrations introduced by an off-axis system designed for laser beam circularization and collimation can be tolerated to a degree as long as the irradiance distribution of the original beam and the transformed beam are approximately the same. Also, in order to reduce aperture diffraction effects while minimizing the mirror sizes, only the portions of the mirrors where approximately 98% of the beam irradiance is reflected are assumed to be the surface diameter. A detailed discussion on aperture diffraction effects can be found in [12].

Laser source is placed with an angle, called the field angle, on the optical axis. Field angle is defined as the angle between the bottom $1/e^2$ ray of the beam and the optical axis (z-axis). This prevents the on-axis obscuration, but keeping the field angle as small as possible limits the off-axis aberrations.

4.4.2 First Design Method

In this design method, the first two mirrors are cylindrical hyperbolic mirrors, the first is convex and the second is concave, specifically used to circularize and expand the elliptical laser beam. Each is defined by its own focal length in the parallel transverse direction while they are optically flat in the perpendicular transverse direction. Figure 4.3 and Figure 4.4 display the position of the mirrors with respect to each other on the x-z

and y-z planes, respectively. The hyperbola function is illustrated in its local coordinate system in Figure 4.5.
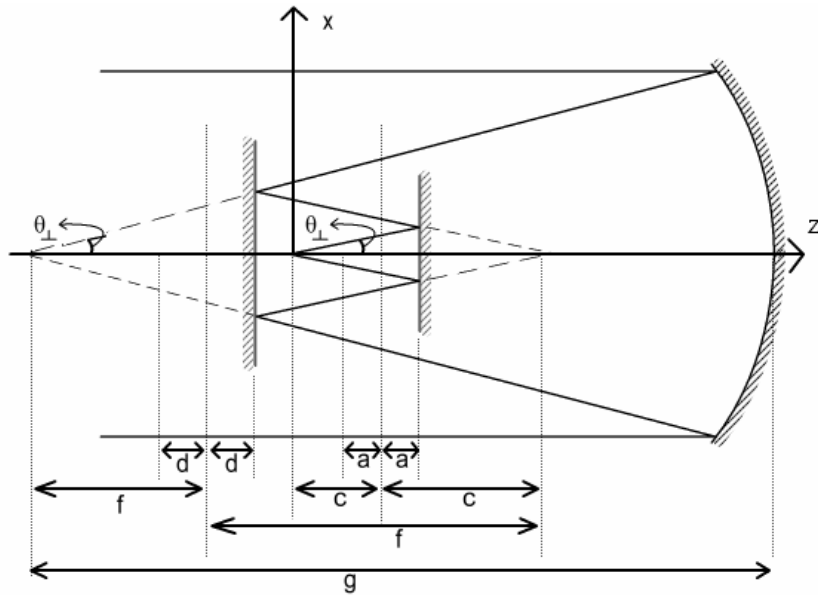
Figure 4.3: x-z plane illustration of the first design method.
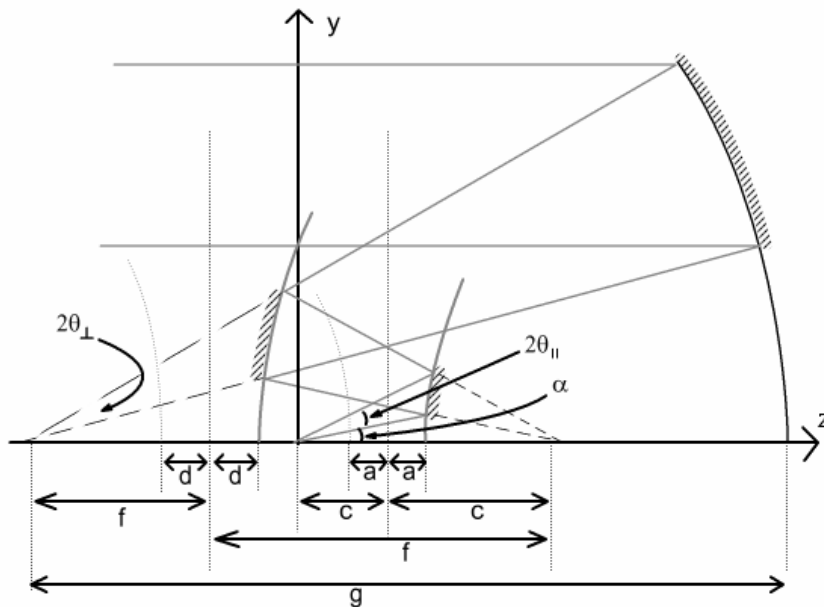
Figure 4.4: y-z plane illustration of the first design method.
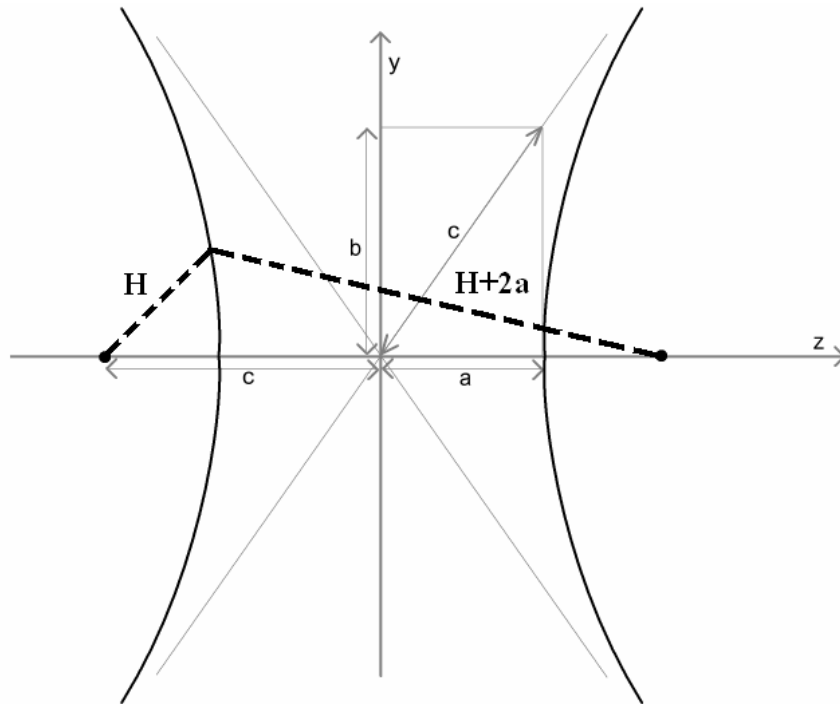
Figure 4.5: Illustration of the hyperbola function.

In order to circularize an elliptical laser beam, two conditions must be satisfied: (1) the two transverse divergence angles of the beam must be equal after reflection from the second mirror, (2) the source points for both transverse directions must coincide at the same point of origin after reflecting from the second mirror, as seen in Figure 4.3 and Figure 4.4.

Constant optical path length condition according to Fermat's Principle [78] states that all the rays traced through an optical system must have the same optical path length. Using this fact, the second condition results in Equation 4.7 (see also Figure 4.6):

$$|A, E| = |B, D| + |D, E| \qquad (4.7)$$
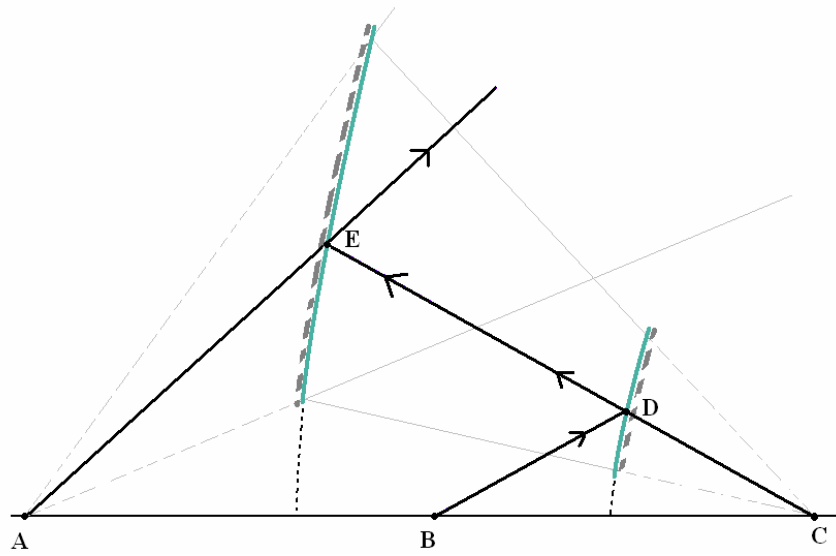
Figure 4.6: Optical path of the "chief ray" of the beam.

The path lengths [A, B], [B, D], and [D, E] in Figure 4.6 and in Equation 4.7 are the rays representing the center of the beam incident on the center of each reflecting surface. These rays are referred to as the "chief rays" throughout the dissertation. It is also known from the primary property of hyperbolas that the difference between the distances from an arbitrary point on the hyperbola curves to the two foci always equals $2a$, as seen in Figure 4.5. Therefore, referring to Figure 4.5 and Figure 4.6, the following equation for the first hyperbolic mirror is derived:

$$|B, D| = |C, D| + 2a \qquad (4.8)$$

The mirror parameters for the second hyperbola have the same meaning except they are named d, e, and f respectively. Also, the equations derived above are the same for the second hyperbolic mirror and are given as:

$$|A, E| = |C, E| + 2d \qquad (4.9)$$

If Equations 4.8 and 4.9 are substituted in Equation 4.7, the following equation is obtained:

46

$$a = d \tag{4.10}$$

The third mirror is chosen as a rotational symmetric parabolic mirror to collimate the laser beam. The parabola function is characterized by only one parameter, g, and is shown in Figure 4.7 in its local coordinate system.
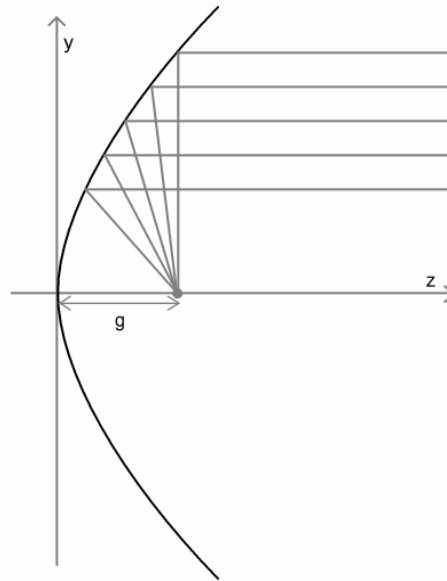
Figure 4.7: Illustration of the parabola function.

The rays in the parallel and perpendicular directions have a common source point at the virtual focal point of the second mirror. This source point is also the focal point of the rotationally symmetric parabolic mirror serving to collimate the laser beam in both transverse directions. In addition, the virtual focal point of the first mirror must be chosen to coincide with the real focal point of the second mirror for the intended reflection of the beam at the mirrors.

Table 4.1 shows the general hyperbola and parabola equations (Equations 4.11 – 4.13), the distance between the laser source and the first mirror vertex (Equation 4.11), and the distances between the vertexes of each mirror respectively (Equations 4.12, 4.13).

Table 4.1: General mirror equations for the first mirror-based design method

	Surface Equation (in local coordinates)	Distance between Surfaces	Incident Ray Slope	Eq
Hyperbolic Mirror-1	$\dfrac{z^2}{a^2} - \dfrac{y^2}{b^2} = 1$	$a + c$	m_i	(4.11)
Hyperbolic Mirror-2	$\dfrac{z^2}{d^2} - \dfrac{y^2}{e^2} = 1$	$a + f - (c + d)$	m_j	(4.12)
Parabolic Mirror	$y^2 = 4gz$	$g - (d + f)$	m_k	(4.13)

As stated earlier, the beam divergence angle in the parallel transverse direction (y-axis) is further increased and kept constant in the perpendicular direction. Therefore, the mirror parameters are calculated and presented only in the y-z plane. The equations seen in Table 4.1 are used to determine the equations of the coordinates of the mirrors in their local coordinates.
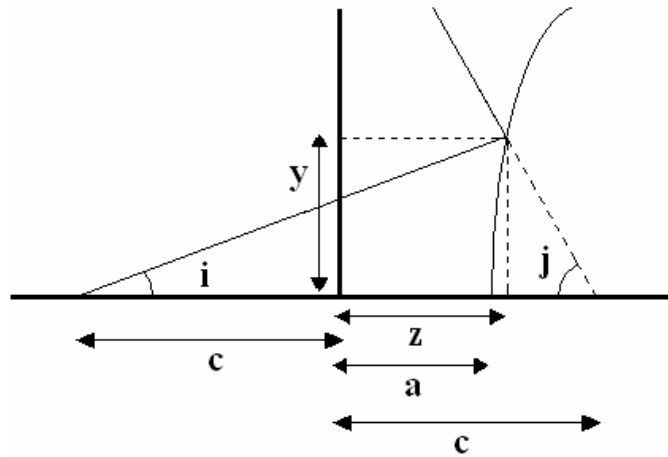
Figure 4.8: Illustration of the first hyperbolic mirror in its local coordinates.

The first hyperbolic mirror is illustrated in its local coordinates in Figure 4.8. The following trigonometric relationship is determined:

$$y = m_i(z + c) \tag{4.14}$$

The above equation and Equation 4.11 ($\frac{z^2}{a^2} - \frac{y^2}{b^2} = 1$) are equated to each other and solved for *z,* as follows:

$$z = -c + \frac{b^2 c + ba\sqrt{b^2 + m_i^2(c^2 - a^2)}}{b^2 - m_i^2 a^2} \tag{4.15}$$

It is also known from the hyperbola definition that:

$$c = \sqrt{a^2 + b^2} \tag{4.16}$$

Equation 2.10 is substituted in Equation 4.15:

$$z = \frac{a^2 m_i^2 c + b^2 a\sqrt{m_i^2 + 1}}{b^2 - m_i^2 a^2} \tag{4.17}$$

The slope m_j is solved as:

$$m_j = \frac{y}{c - z} = \frac{m_i b^2 \left(a\sqrt{m_i^2 + 1} + c\right)}{cb^2 - b^2 a\sqrt{m_i^2 + 1} - 2a^2 m_i^2 c} \tag{4.18}$$
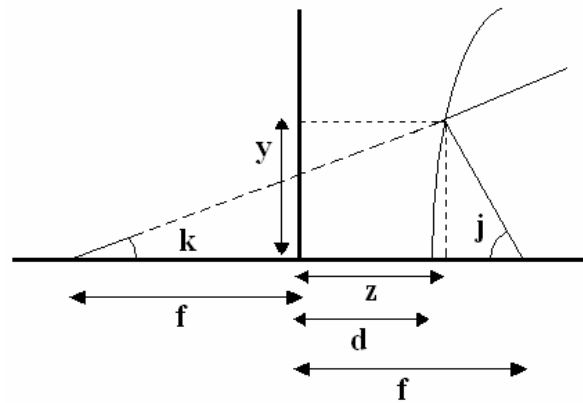
Figure 4.9: Illustration of the second hyperbolic mirror in its local coordinates.

The second hyperbolic mirror is illustrated in its local coordinates in Figure 4.9. The trigonometric relationship in Equation 4.19 is determined:

$$z = f - \frac{y}{m_j} \tag{4.19}$$

$$f = \sqrt{d^2 + e^2} \tag{4.20}$$

Equation 4.19 and Equation 4.12 are equated to each other and solved for y. Equation 4.20 is substituted in this solution and the following equations are obtained:

$$y = \frac{m_j \left(e^2 f - de^2 \sqrt{m_j^2 + 1} \right)}{e^2 - m_j^2 d^2} \tag{4.21}$$

$$z = \frac{-d^2 m_j^2 f + de^2 \sqrt{m_j^2 + 1}}{e^2 - m_j^2 d^2} \tag{4.22}$$

$$m_k = \frac{m_j \left(e^2 f - de^2 \sqrt{m_j^2 + 1} \right)}{e^2 f + de^2 \sqrt{m_j^2 + 1} - 2d^2 m_j^2 f} \tag{4.23}$$
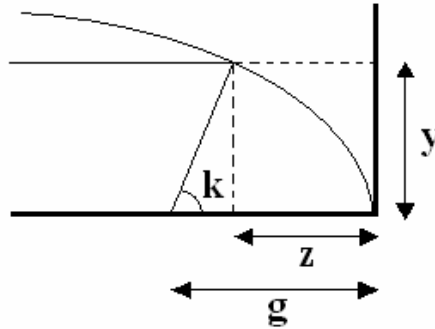
Figure 4.10: Illustration of the parabolic mirror in its local coordinates.

The parabolic mirror is illustrated in its local coordinates in Figure 4.10. The trigonometric relationship is determined:

$$z = g - \frac{y}{m_k} \qquad (4.24)$$

Equation 4.24 and Equation 4.13 are equated to each other and solved for y:

$$y = \frac{2g}{k}\left(\sqrt{m_k^2 + 1} - 1\right) \qquad (4.25)$$

The local coordinates are transformed to a global coordinate system where the source (the laser output beam) is located at (0,0,0) and is chosen as the reference point of the global coordinate system. Using these equations and coordinate transformation, mirror coordinate equations are derived and presented in Table 4.2 (Equations 4.26 – 4.28). Table 4.3 shows the equations of the slopes of the rays reflected from each surface.

Table 4.2: Global coordinate equations of the mirrors for the first mirror-based design method

	Coordinates (in global coordinate system)		Eq
Hyperbolic Mirror-1	$z_1 = \dfrac{a^2 m_i^2 c + ab^2\sqrt{m_i^2 + 1}}{b^2 - a^2 m_i^2} + c$	$y_1 = m_i z_1$	(4.26)
Hyperbolic Mirror-2	$z_2 = \dfrac{de^2\sqrt{m_j^2 + 1} - d^2 m_j^2 f}{e^2 - d^2 m_j^2} + 2c - f$	$y_2 = m_j(2c - z_2)$	(4.27)
Parabolic Mirror	$z_3 = 2\left[c + \dfrac{g\left(\sqrt{m_k^2 + 1} - 1\right)}{m_k^2} - f\right]$	$y_3 = m_k[z_3 + 2(f - c)]$	(4.28)

Table 4.3: Slopes of the rays for the first mirror-based design method

	Reflected Ray Slope	Eq
Hyperbolic Mirror-1	$$m_j = \frac{m_i\left(cb^2 + ab^2\sqrt{m_i^2+1}\right)}{cb^2 - ab^2\sqrt{m_i^2+1} - 2a^2m_i^2c}$$	(4.18)
Hyperbolic Mirror-2	$$m_k = \frac{m_j\left(fe^2 - de^2\sqrt{m_j^2+1}\right)}{fe^2 + de^2\sqrt{m_j^2+1} - 2d^2m_j^2f}$$	(4.23)
Parabolic Mirror	$$m_r = 0$$	(4.29)

It should be noted that the laser output beam size is on the order of a few μm, and that the design presented here is expected to expand this beam to a collimated circular beam of 10 cm after reflection from the third (parabolic) mirror. With this and other conditions in mind, the mirror sizes are chosen so that 98% of power is reflected by the system. This corresponds to the beam size equal to 1.4 times the $1/e^2$ rays. These rays will be called "1.4 rays" throughout this chapter.

The system variables are the field angle, the parameters a and b of the first hyperbolic mirror, the parameters d and e of the second hyperbolic mirror, and the parameter g of the parabolic mirror. The beam (waist) radius w_f at the parabolic mirror is a constant depending on the particular application and chosen to be 10 cm as the design constraint for this design method. The parameter g of the parabolic mirror depends on the parameters of the first two hyperbolic mirrors. The parameter c and f of the hyperbolic mirrors depend on a, b, d and e of the two hyperbolic mirrors and can be determined by Equations 4.16 and 4.20.

Based on the design constraint, the beam full divergence angle equals to $2\theta_\perp$ after reflection from the second mirror, where the beam is defined with the representative $1/e^2$ rays k_2 and k_4, as shown in Figure 4.7. This provides a relationship between m_{k2} and m_{k4} equations, determined by substituting these particular rays in Equation 4.29. Then, the first and second mirror parameters are determined by iteration. Another constraint is that w_f is chosen at the beginning depending on the particular application, as stated earlier. This provides a relationship between y_3 values of k_2 and k_4 rays.

4.4.3 Second Design Method

The second mirror-based design method consists of three off-axis cylindrical parabolic mirrors and satisfies the same two conditions as in the first method in order to reshape an elliptical laser beam. The first two mirrors in this method are parabolic in the perpendicular direction and flat in the parallel direction. The third one is a rotationally symmetric parabolic mirror with a real focal point that coincides with the virtual focal point of the second mirror collimating the beam in both transverse directions as in the first method.

Figure 4.11 and Figure 4.12 display the beam shaping system in the perpendicular transverse direction – optical axis (x-z) and the parallel transverse direction - optical axis (y-z) planes respectively.
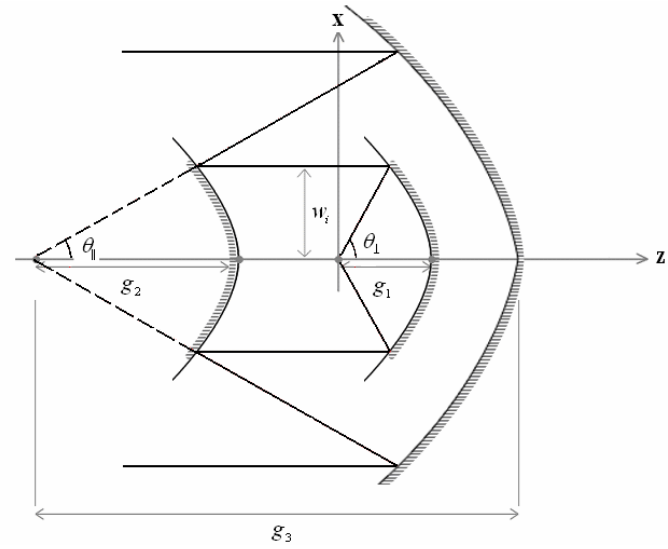
Figure 4.11: x-z plane illustration of the second design method.
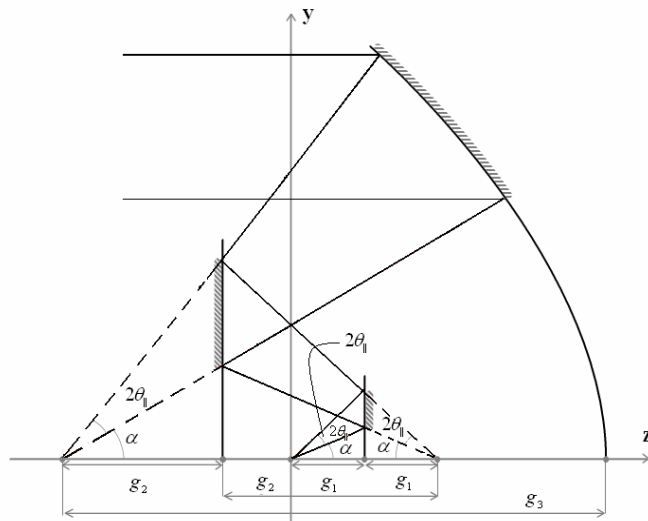
Figure 4.12: y-z plane illustration of the second design method.

It is seen in Figure 4.11 that the rays are reflected parallel from the first mirror in the x-z plane. This also means that m_j equals zero. The variables in this system are the mirror parameters g_1, g_2, and g_3, the parallel and perpendicular half divergence angles ($\theta_\parallel$ and $\theta_\perp$), and the field angle (α) of the laser.

Similar to the first design, the mathematical equations of the surfaces of this design method are derived in their local coordinate systems and then modified to function accurately in a global coordinate system where the laser beam starts as a point source at (0, 0, 0). All of the mirrors are parabolic and the local coordinate equations of these mirrors are determined the same way as for the parabolic mirror of the first design method. Therefore, these equations are not reproduced here and the global coordinate equations are directly presented in Tables 4.4 and 4.5 (Equations 4.30 – 4.36). The distance between the laser source and the first mirror vertex (Equation 4.31) and the distances between the vertexes of each mirror respectively (Equations 4.32, 4.33) are also presented in Table 4.4.

Table 4.4: General mirror and ray equations for the second mirror-based design method

Surface Equation for All Mirrors (in local coordinates) $\rightarrow$ $x^2 = 4gz$				Eq (4.30)
	Incident Ray Slope	Distance between Surfaces	Reflected Ray Slope	
Mirror-1	$m_i = \tan(\theta_\perp)$	g_1	$m_j = 0$	(4.31)
Mirror-2	m_j	$g_2 - g_1$	$m_k = \tan(\theta_\parallel)$	(4.32)
Mirror-3	m_k	$g_3 - g_2$	$m_r = 0$	(4.33)

Table 4.5: Global coordinate equations of the mirrors for the second mirror-based design method

	Coordinates (in global coordinate system)		Eq
Mirror-1	$z_1 = \dfrac{2g_1\left(\sqrt{m_i^2+1}-1\right)}{m_i^2}$	$x_1 = m_i z_1$	(4.34)
Mirror-2	$z_2 = 2\left[g_1 - g_2\left(1 - \dfrac{\sqrt{m_k^2+1}-1}{m_k^2}\right)\right]$	$x_2 = x_1$	(4.35)
Mirror-3	$z_3 = 2\left(g_1 + \dfrac{g_3\left(\sqrt{m_k^2+1}-1\right)}{m_k^2} - g_2\right)$	$x_3 = m_k\left[z_3 + 2(g_2 - g_1)\right]$	(4.36)

In this method, different from the first method, the beam divergence angle in the perpendicular transverse direction (x-axis) is compressed and kept the same in the parallel transverse direction. Therefore, the mirror parameters are calculated and presented only in the x-z plane. Incident and reflected ray slopes in the x-z plane are directly related to the divergence angles of the beam because the field angle is in the y-z plane. Hence, the slope equations in Table 4-4 are presented for the "upper" $1/e^2$ ray that represents the beam.

As in the first design method, the distances between the mirrors depend on the mirror parameters and the field angle. As seen in Figure 4.11, the beam reflected from the first mirror propagates as a collimated beam to the second mirror. The Rayleigh range of the beam must be high compared to the distance between the two mirrors. The beam waist in the perpendicular direction after reflecting from the first mirror is defined by w_i, as seen in Figure 4.11. The value of w_i must be chosen such that a long Rayleigh range is

ensured. On the other hand, in order to design a more practically feasible system, the mirrors should be chosen as small as possible setting an upper limit for w_i. As a result, w_i is chosen to be 1 cm in this design. Once the coordinate transformation is done, using the design constraints for w_i and w_f, the mirror parameters g_1, g_2, and g_3 are determined by using Equations 4.34 – 4.36.

4.5 Aspherical Lens-Based Optical System Design for Circularization, Collimation, and Expansion of Elliptical Laser Beams

4.5.1 Overview and Design Approach

Two optical system designs using aspherical lenses to circularize and collimate an edge-emitting semiconductor laser output beam for possible application in LIDAR systems. These systems employ two aspherical lenses and a single aspherical lens, respectively.

In order to reduce aperture diffraction effects while minimizing the lens sizes, only the portions of the lenses where approximately 99.78% of the beam irradiance is reflected are assumed to be the surface diameter. To determine the lens aperture radius, the power transmission equation [15] is used:

$$\frac{P_a}{P_T} = 1 - e^{-2a^2/w^2(z)}$$

(4.37)

where, a is the aperture radius, $w(z)$ is the beam spot radius at position z, P_T is the total power of the input beam, and P_a is the transmitted power through the aperture. For 99.78% power transmission, $a = 1.75 w_f$ is required, where w_f is the final circularized

and collimated beam radius. In both design methods, same lens aperture size is chosen for all the lens surfaces.

In order to calculate the position of the lens surfaces with respect to the source, and the radii of surfaces as the starting point, the general refraction equation for spherical waves is used as follows:

$$\frac{n_1}{s_1} + \frac{n_2}{s_2} = \frac{n_2 - n_1}{R}$$ (4.38)

where n_1 and n_2 are the refraction index of the first and second media separated by the refractive surface, s_1 is the object distance, s_2 is the image distance, and R is the radius of curvature of that refractive surface [78]. Aspheric surfaces in both design methods are defined with conic constant values along with radius of curvature values.

4.5.2 Two-Lens Design Method

This design method employs two aspherical lenses, as shown schematically in Figure 4.13 for a laser beam with $\theta_\perp > \theta_\parallel$. First, the beam is collimated in both perpendicular and parallel transverse directions at the front surface of the first lens (S_{11}) only. The beam at this stage is still has the elliptical shape while propagating within the lens. Then only the beam in the parallel transverse direction is allowed to diverge at the back surface of the first surface (S_{12}) while the beam in the perpendicular transverse direction propagates with no refraction. The second lens is positioned at a distance from the first where the beam shape becomes circular. Then this surface (S_{21}) is designed to collimate the beam only in the parallel perpendicular beam allowing the beam to continue to propagate as a collimated circular beam in both transverse directions. The back surface

58

of the second lens (S_{22}) is designed to be flat, so the output beam has the desired circular, collimated, and expanded beam shape.
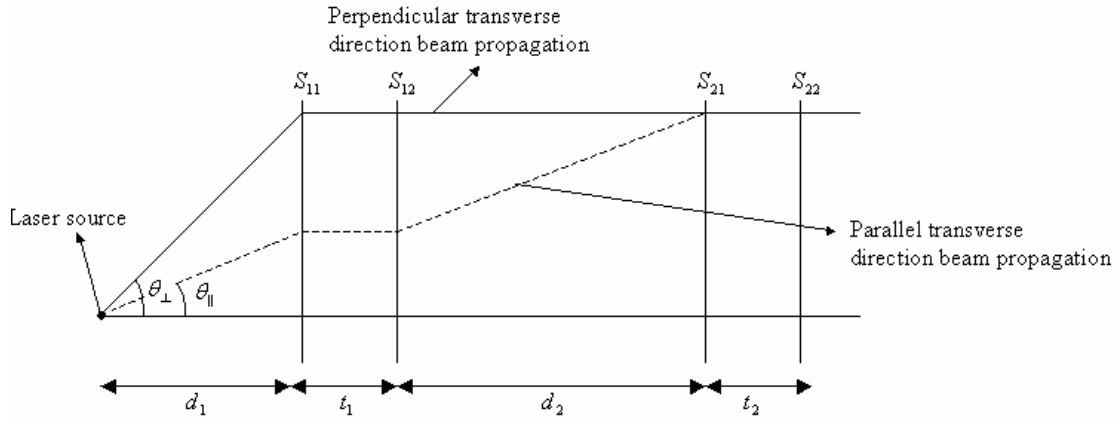
Figure 4.13: A schematic diagram of two-lens system. Here S_{ij} represents each refractive surface of the lenses used in this design. S_{11} is rotationally symmetric, S_{12} is cylindrical symmetric (flat in the perpendicular direction), S_{21} is a cylindrical symmetric (flat in the perpendicular direction), and S_{22} is flat (in both directions) surfaces.

As a first step, the front surface of the first lens (S_{11}) is designed. Once the surface parameters of this surface are determined, then the parameters of the back surface of this lens (S_{12}) and the front surface of the second lens (S_{21}) are determined. As a design constraint, the output beam radius w_f is specified (to be approximately 2.0 cm).

Figure 4.14 shows a representation of the surfaces in the perpendicular transverse direction (x-z plane) and variables used to calculate lens parameters for the front surface of the first lens. In Figure 4.14 and the following equations, L is the directrix of the conic section, e is eccentricity of the conic section, a is the semi-major axis parameter, b is the semi-minor axis parameter, and $c = \sqrt{a^2 + b^2}$. Also, the subscript $ij = 1,2$ refers to as follows: i is the first or second lens, and j is the first (front) or second (back)

surface, and x_{s11} is the sag of the (S_{11}) surface in perpendicular direction. Also, the refractive index for air is designated as n_0 and is equal to 1 and for glass (BK7) medium it is designated as n and it is equal to 1.5095 (at 870 nm) in the equations derived throughout this paper.
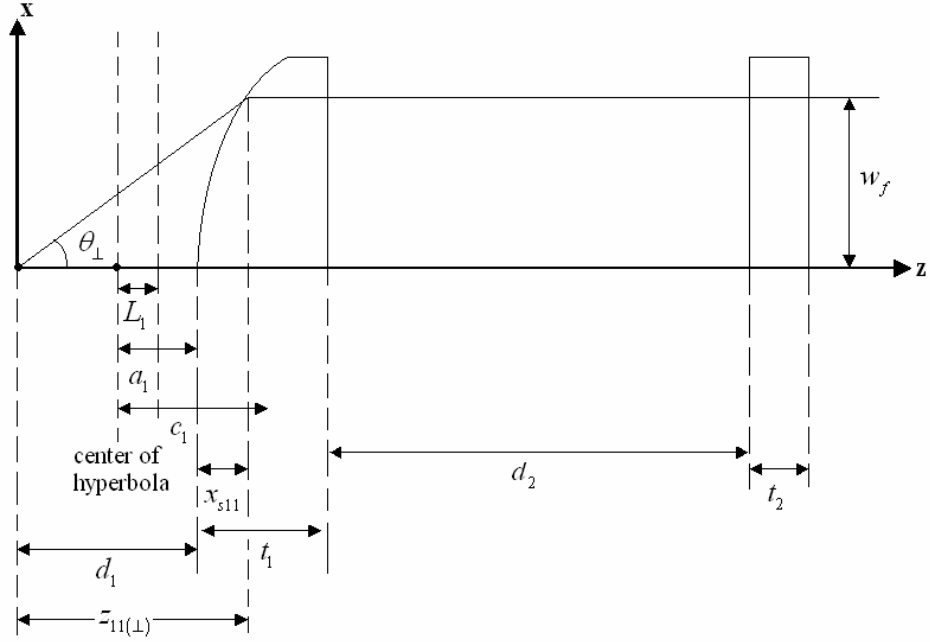
Figure 4.14: A schematic representation of the surfaces in the x-z plane.

The S_{11} surface is a rotationally symmetric surface, and only the x-z plane calculations are shown in this section. The y-z plane calculations are the same as x-z plane.

From a trigonometric relation:

$$z_{11(\perp)} = \frac{w_f}{\tan(\theta_\perp)}$$

(4.39)

From Fermat's Principle, we have:

$$n_0 d_1 + n x_{s11} = n_0 \sqrt{w_f^2 + z_{11(\perp)}^2} \tag{4.40}$$

Using $d_1 = z_{11(\perp)} - x_{s11}$ and Equation 4.40:

$$n_0 \left(z_{11(\perp)} - x_{s11} \right) + n x_{s11} = n_0 \sqrt{w_f^2 + z_{11(\perp)}^2} \tag{4.41}$$

Solving simultaneously Equation 4.39 and 4.41 provides the numeric value of the distance, d_1, between the source and the vertex of S_{11}. Using Equation 4.38, the radius of curvature of the front surface is determined as S_{11} as $R_{11} = R_{11(\perp)} = R_{11(\parallel)} = 0.5095 d_1$ for the object and image distance values of $s_1 = d_1$, $s_2 = \inf$.

As stated earlier, Equation 4.38 is valid only for paraxial rays and the laser beam in this study is a highly divergent elliptical beam. Therefore, determining only the radius of curvature is not sufficient for the beam to propagate as desired within the lens. The S_{11} surface is intended to be a rotationally symmetric hyperbolic surface as a design constraint, and the hyperbolic surface definition is used to determine the conic constant of the surface. It is known from the hyperbola definition that the locus of points whose distance from the focus is proportional to the horizontal distance from the conic section directrix. The ratio is given with the eccentricity of the hyperbola. Therefore:

$$\frac{\sqrt{\left(z_{11(\perp)} - (d_1 - a_1) - c_1 \right)^2 + w_f^2}}{\left(a_1 - L_1 + x_{s11} \right)} = e_1 \tag{4.42a}$$

Furthermore, the hyperbola parameters are:

$$R_1 = \frac{b_1^2}{a_1} \tag{4.42b}$$

$$c_1 = \sqrt{a_1^2 + b_1^2} = \sqrt{a_1^2 + a_1 R_1} \tag{4.42c}$$

61

$$e_1 = \frac{c_1}{a_1} = \frac{\sqrt{a_1^2 + a_1 R_1}}{a_1} \qquad (4.42\text{d})$$

$$L_1 = \frac{a_1^2}{c_1} = \frac{a_1^2}{\sqrt{a_1^2 + a_1 R_1}} \qquad (4.42\text{e})$$

$$K_1 = -1 - \frac{b_1^2}{a_1^2} \qquad (4.42\text{f})$$

Substituting Equations 4.42b-e in Equation 4.42a, an equation with only one variable a_1 is obtained, as given below:

$$\frac{\sqrt{\left(x_{s11} + a_1 - \sqrt{a_1^2 + a_1 R_1}\right)^2 + x_0^2}}{\left(a_1 - \dfrac{a_1^2}{\sqrt{a_1^2 + a_1 R_1}} + x_{s11}\right)} = \frac{\sqrt{a_1^2 + a_1 R_1}}{a_1} \qquad (4.43)$$

a_1 is found solving the above equation. Then, b_1 is found solving Equation 4.42b. Then the conic constant of the hyperbola is found using Equation 4.42f.

Next, the aperture diameter (physical diameter of the surface of the lenses in both transverse directions) and the lens thickness are determined using the energy transmission criteria of over 99% as stated earlier. For simplicity, the aperture sizes of both lenses are decided to be the same. In general the energy transfer through an aperture is given by $\frac{P_a}{P_T} = 1 - e^{-2a^2/w^2(z)}$, where P_T is the total input power, P_a is the transmitted power through the aperture, a is the aperture radius, and $w(z)$ is the beam spot radius at a position z. In our case, we define the parameters $a = h$ defined and assumed both lenses have the same aperture size. Rewriting the power transmission equation yields to:

$$\frac{h}{w_f} = \sqrt{-0.5\ln\left(1 - \frac{P_a}{P_T}\right)} \qquad (4.44)$$

From this, the aperture radius is calculated as $h = 1.75w_f$. for 99.78% power transmission.

The thickness of the first lens is determined in order to design the back surface of the first lens (S_{12}). The two surfaces, S_{11} and S_{12}, are highly curved surfaces. Therefore, the thickness of the lens is calculated while making sure that S_{11} does not intersect with S_{12} at any x and y coordinate points. When h is substituted for x and z_h for z in the general hyperbola equation $\frac{z^2}{a^2} - \frac{x^2}{b^2} = 1$ in the x-z plane, the equation for minimum thickness for the first lens is obtained as:

$$t_1 = z_h - a_1 = a_1\left(\sqrt{\left(\frac{h}{b_1}\right)^2 + 1} - 1\right) \qquad (4.45)$$

One should remember that S_{11} is a rotationally symmetric surface, and the beam is collimated by this surface in both transverse directions, but not yet circularized. Therefore, S_{12} is designed to allow the beam to propagate without any refraction in the perpendicular direction while allowing it to diverge further in the parallel direction. That mens, S_{12} is flat in perpendicular direction (see Figure 4.14), but is not flat in parallel direction (see Figure 4.15). The second lens is positioned at a distance when the beam profile becomes circular in both transverse directions (see Figure 4.13). The variables used to calculate lens parameters in the parallel transverse direction (y-z plane) for both surfaces are shown in Figure 4-15.

63

After exiting the S_{12} surface, the beam diverges with an angle θ in the parallel direction (see Figure 4.15). The corresponding ray is extended so as to intersect the optical axis forming the virtual object location for this ray on the left hand side of the first lens. This distance between the intersection point (virtual object) and the vertex of the S_{12} surface is defined as q_1. As a result, there are five unknown quantities: y_{11}, y_{s11}, q_1, y_{s12}, and y_{s21}.
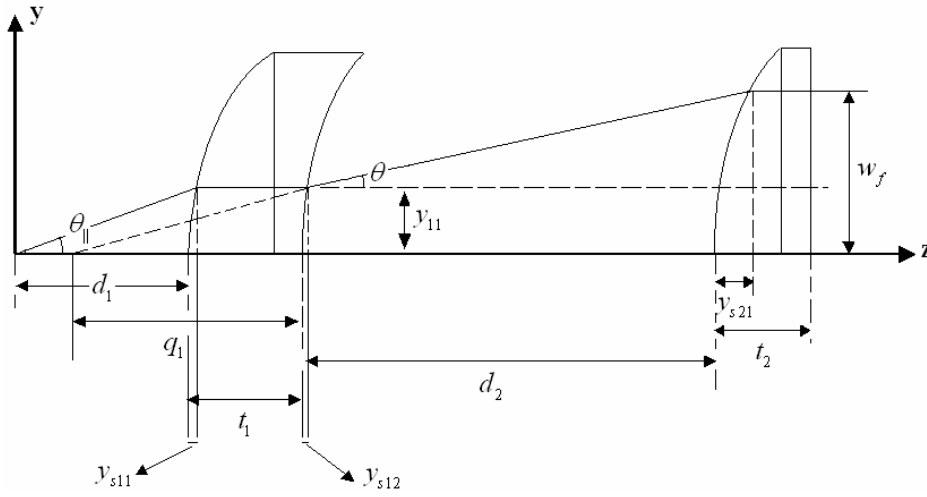
Figure 4.15: A schematic representation of the surfaces in the y-z plane.

Five equations are needed to solve these five unknown quantities.

From Fermat's principle:

$$n_0 d_1 + n y_{s11} = n_0 \sqrt{y_{11}^2 + (d_1 + y_{s11})^2} \qquad (4.46)$$

From a trigonometric relation:

$$\tan(\theta_{\parallel}) = \frac{y_{11}}{d_1 + y_{s11}} \qquad (4.47)$$

Equation 4.46 and Equation 4.47 are solved together for y_{11} and y_{s11}. Three more equations are needed to determine the remaining unknown quantities q_1, y_{s12}, and y_{s21}.

64

From a trigonometric relation:

$$\tan(\theta) = \frac{w_f - y_{11}}{d_2 - y_{s12} + y_{s21}} = \frac{y_{11}}{q_1 + y_{s12}}$$ (4.48)

From Fermat's principle:

$$n(t_1 - y_{s11}) + n_0 d_2 + n y_{s21} =$$
$$n(t_1 - y_{s11} + y_{s12}) + n_0 \sqrt{(d_2 - y_{s12} + y_{s21})^2 + (w_f - y_{11})^2}$$ (4.49)

We need one more equation to solve for all the unknowns. This can be derived by assuming the left side of S_{12} surface to be air and the right side of to be glass medium. Then a "real" ray originating from the location of the virtual object point on the left of the lens would be collimated after exiting the S_{12} surface of the lens. Using this fact and the Fermat's principle, the following equation is derived:

$$n_0 q_1 + n y_{s12} = n_0 \sqrt{y_{11}^2 + (q_1 + y_{s12})^2}$$ (4.50)

Then, Equations 4.48, 4.49, and 4.50 are solved simultaneously for q_1, y_{s12}, and y_{s21}. Again, from Equation 4.38, for the object distance of $s_1 = \inf$ and the image distance of $s_2 = -q_1$ the radius of curvature of the S_{12} surface is determined as $R_{12(\|)} = 0.5095 q_1$. For S_{21} surface, the radius of curvature of is calculated as $R_{21(\|)} = 0.5095(q_1 + d_2)$ for the object distance of $s_1 = q_1 + d_2$ and the image distance of $s_2 = \inf$.

One should remember that S_{12}, and S_{21} surfaces are both cylindrical (have refractive powers in the y-z plane only and flat in the x-z plane). Using the hyperbola definition,

similar to the ones in Equation 4.42, the parameter a_2 of S_{12} and the parameter a_3 of S_{21} are determined as follows:

$$\frac{\sqrt{\left(y_{s12} + a_2 - \sqrt{a_2^2 + a_2 R_{12(\parallel)}}\right)^2 + y_{11}^2}}{\left(a_2 - \dfrac{a_2^2}{\sqrt{a_2^2 + a_2 R_{12(\parallel)}}} + y_{s12}\right)} = \frac{\sqrt{a_2^2 + a_2 R_{12(\parallel)}}}{a_2} \qquad (4.51)$$

$$\frac{\sqrt{\left(y_{s21} + a_3 - \sqrt{a_3^2 + a_3 R_{21(\parallel)}}\right)^2 + w_f^2}}{\left(a_3 - \dfrac{a_3^2}{\sqrt{a_3^2 + a_3 R_{21(\parallel)}}} + y_{s21}\right)} = \frac{\sqrt{a_3^2 + a_3 R_{21(\parallel)}}}{a_3} \qquad (4.52)$$

The conic constants of these two surfaces are determined as for the S_{11} surface. Similarly from the hyperbola equation for the y-z plane, the minimum thickness of the second lens is obtained as:

$$t_2 = z_h - a_3 = a_3 \left(\sqrt{\left(\frac{h}{b_3}\right)^2 + 1} - 1\right) \qquad (4.53)$$

The lens thickness values must be chosen to satisfy the minimum condition determined for both lenses with Equations 4.45 and 4.53. As mentioned earlier, no calculations are needed for the back surface of the second lens since the beam is already circular and collimated before interacting with this surface. Hence, this last surface is chosen to be flat in both transverse directions.

4.5.3 Single-Lens Design Method

This design method uses a single asymmetrical lens. The front surface (S_1) is anamorphic with two different refractive powers and surface functions in the two

66

transverse directions. The back surface (S_2) is a cylindrical surface (has refractive power in the y-z plane and is flat in the x-z plane). Figure 4.16 shows the schematic diagram of these surfaces. Similar to the two-lens system, the beam is collimated in the perpendicular direction only at the S_1 surface. However, the beam in the parallel direction is allowed to propagate with a different divergence angle within the lens after refraction at S_1 surface. The S_2 surface is flat in the perpendicular direction allowing the beam propagate through with no refraction in this direction, while the surface in parallel direction collimates the beam, so the output beam has the desired circular, collimated, and expanded beam shape.
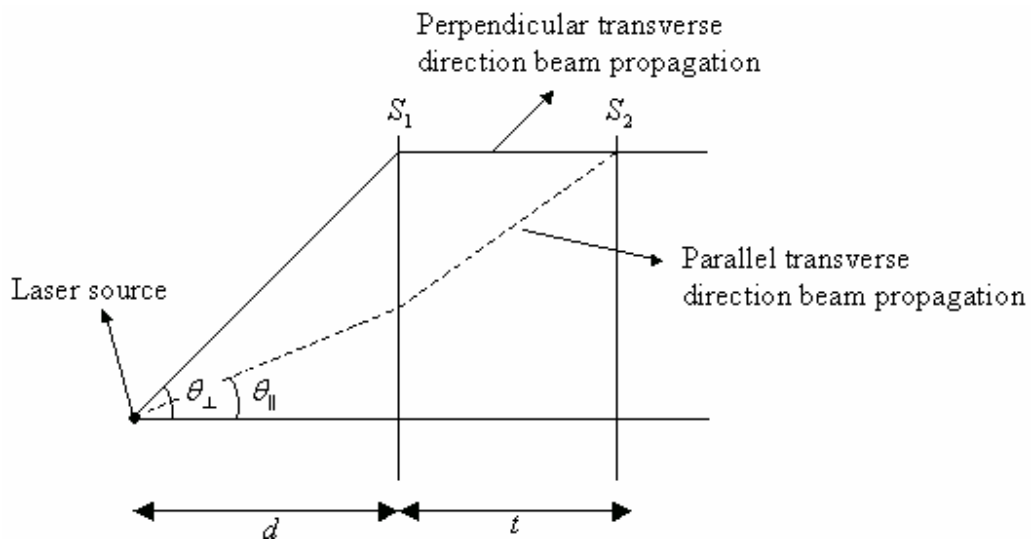
Figure 4.16: A schematic diagram of single lens system. Here, S_1 is a hyperbolic surface in the perpendicular direction and is elliptical in the parallel direction. The surface S_2 is an elliptical surface in the parallel direction and flat in the perpendicular direction.

Figure 4.17 displays the schematic representation of the surfaces in the perpendicular transverse direction (x-z plane) including the lens variables used in the calculations. The x-z plane calculations are the same as in the two-lens system. Therefore, the x-z plane

67

calculations are not repeated here. There are only a few notation changes as the surfaces are defined by single subscript. The distance from the laser source to the vertex of the front surface and the lens thickness are d and t respectively (no subscript).
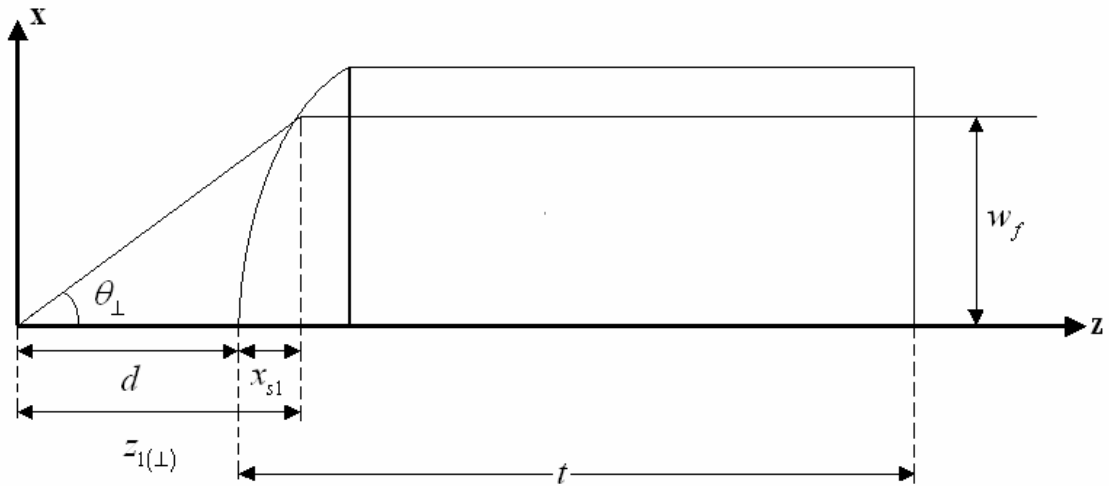
Figure 4.17: A schematic representation of the surfaces in the x-z plane.
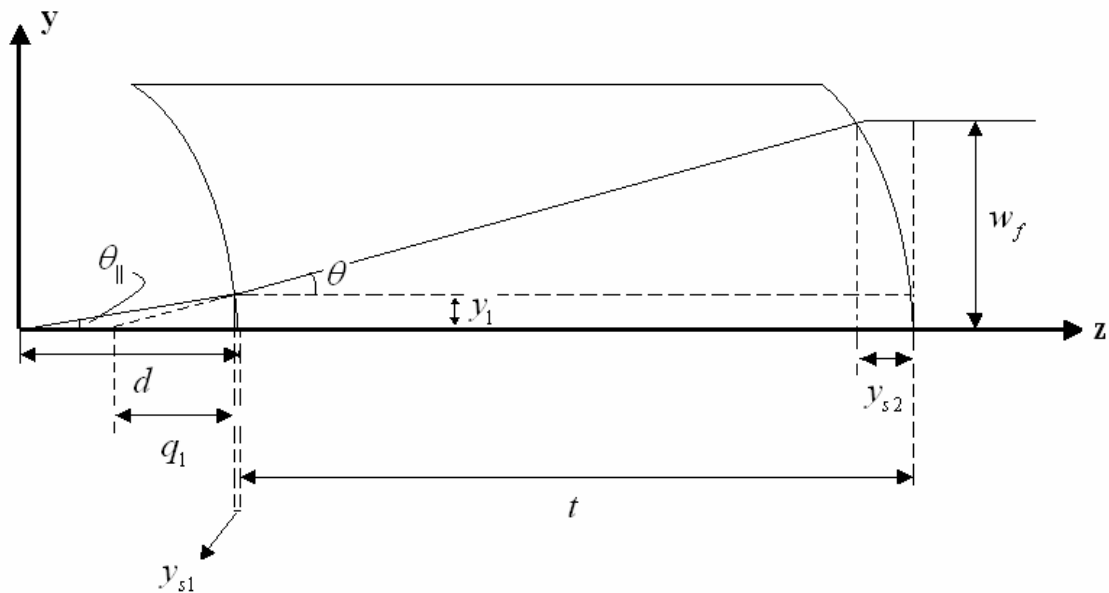
Figure 4.18: A schematic representation of the surfaces in the y-z plane.

68

Figure 4.18 shows the schematic representation of the surfaces in the parallel transverse direction (y-z plane) and the variables used to calculate lens parameters. Fermat's Principle and trigonometric relationships are used to determine the surface parameters. The parallel transverse direction divergence angle ($\theta_\parallel$), the final output beam radius (w_f), and the thickness of the lens (t) are chosen quantities as the design constraints. The distance d has already been found in the x-z plane calculations.

y_1, y_{s1}, and y_{s2} must be calculated to determine the surface parameters. At the S_1 surface, the beam further diverges in the parallel direction, and the virtual object point is formed on the optical axis between the laser source and the vertex of the first surface. The distance between the virtual object point and the vertex of the front surface is $q_1 + y_{s1}$. Under the circumstances, there are four unknown quantities y_1, q_1, y_{s1}, and y_{s2} meaning that four equations are needed to solve for them.

First equation is derived applying the Fermat's principle for the S_2 surface. For this, it is assumed that the left side of this surface is glass whereas the right side of it is air. Tracing the ray propagating on the optical axis and the representative $1/e^2$ ray from virtual object point up to the exit plane we obtain have the following equation for constant optical path length (OPL):

$$n(q_1 + y_{s1} + t) = n\sqrt{(q_1 + y_{s1} + t - y_{s2})^2 + w_f^2} + n_0 y_{s2} \qquad (4.54)$$

From a trigonometric relation:

$$\tan(\theta_\parallel) = \frac{y_1}{d - y_{s1}} \qquad (4.55)$$

The third equation also derived from the trigonometric relationship for the ray diverged at the S_2 surface and given by:

$$\tan(\theta) = \frac{w_f - y_1}{t - y_{s2} + y_{s1}} = \frac{y_1}{q_1} \qquad (4.56)$$

Finally, the last equation is determined again from Fermat's Principle tracing the rays from the laser source to the exit plane of the lens.

$$n_0 d + nt = n_0 \sqrt{(d - y_{s1})^2 + y_1^2} + n\sqrt{(w_f - y_1)^2 + (t - y_{s2} + y_{s1})^2} + n_0 y_{s2} \qquad (4.57)$$

Once the unknown quantities are determined using these four equations, the radius of curvature values are calculated using Equation 4.38. For S_1 surface, the object distance value of $s_1 = d$ and the image distance value of $s_2 = -(q_1 + y_{s1})$, are used. For S_2 surface, the object distance value of $s_1 = (q_1 + y_{s1} + t)$ and the image distance value of $s_2 = \inf$, are used. The conic constant values are calculated from aspherical surface equation (without any aspherical polynomial terms) for the both surfaces are determined as follows.

The radius of curvature for the front and the back surfaces respectively:

$$R_{1y} = \frac{0.5095(q_1 + y_{s1})d}{(q_1 + y_{s1}) - 1.5095d}, \qquad (R_{1y} = R_{1(\parallel)}) \qquad (4.58)$$

$$R_{2y} = 0.5095(q_1 + y_{s1} + t), \qquad (R_{2y} = R_{2(\parallel)}) \qquad (4.59)$$

The conic constants for the front and back surfaces respectively:

$$y_{s1} = \frac{C_{1y} y_1^2}{1 + \sqrt{1 - C_{1y}^2 y_1^2 (1 + K_{1y})}}, \qquad (C_{1y} = 1/R_{1y}) \qquad (4.60)$$

70

$$y_{s2} = \frac{C_{2y} w_f^2}{1 + \sqrt{1 - C_{2y}^2 w_f^2 \left(1 + K_{2y}\right)}}, \qquad (C_{2y} = 1/R_{2y}) \qquad (4.61)$$

The conic constant values for the two surfaces are determined solving Equation 4.60 for K_{1y} and Equation 4.61 for K_{2y}.

4.6 Reshaping an Elliptically Diverging Gaussian Laser Beam into a Circular, Collimated, and Expanded Uniform Beam with Aspherical Lens Design

4.6.1 Overview and Design Approach

As mentioned before, high divergence and elliptical profile of edge-emitting semiconductor lasers is undesirable for many LIDAR applications. In addition to high divergence and elliptical beam shape drawback of such lasers, Gaussian irradiance distribution is also undesirable for several applications such as display technology, lithography, laser printing, and material processing because these applications require uniform illumination of an extended area. Therefore, in this section, an optical system design method, which utilizes two aspherical lenses to circularize and collimate an edge-emitting semiconductor laser beam and to transform its irradiance distribution from Gaussian to a uniform-square distribution, is presented. Circularization term is commonly used in the literature for correcting ellipticity in the semiconductor laser beams. In this section, circularization term is still used even though the beam has a uniform-square profile at the output of the system.

As discussed in Section 3.2, there are several studies in the literature developed to transform the beam's irradiance profile to a different profile. However, in most of these

71

studies, the input beam is assumed to be a collimated Gaussian beam and the irradiance distribution is converted to uniform distribution. Moreover, the refractive systems discussed in these studies assume that the input beam has a circular profile. The method discussed in this section is based on the same beam shaping principle [7, 27- 29], but it assumes that the input beam is radiated by an edge-emitting semiconductor laser. Astigmatism in μm levels is neglected in this study since the output beam is collimated at cm level beam radius, but if needed, the model can easily be modified to correct it. As a result, in this section, a specific optical beam shaping system is designed to circularize, collimate, and expand the beam of an edge-emitting semiconductor laser to a desired diameter and to transform its irradiance distribution from Gaussian to uniform.

A square pulse function is chosen as the output beam distribution function for simplicity. As explained in section 3.2, the abrupt change in the output irradiance distribution function causes diffraction effects, which are neglected in this chapter. Geometrical optics methods such as ray tracing, conservation of energy within a bundle of rays, and constant optical path length of all rays are used to design this beam shaper. It is quantitatively shown that geometrical method ray optics approach is a good approximation to physical optics propagation of the beam for this design method by the dimensionless β parameter calculations, as explained in section 4.1. To accomplish the design, the source beam profile is decoupled into two independent beam profiles represented in two transverse directions, i.e. the perpendicular and parallel transverse directions.

4.6.2 Design Method

As mentioned in the previous section, the beam profile is modeled as two independent 2-D Gaussian beams propagating along the two orthogonal planes (the *x-z* and the *y-z* planes). Therefore, the beam shaper is designed separately in these two orthogonal planes to achieve a circular, collimated, and uniform beam at the output plane.

All surfaces, but the back surface of the second lens, are designed as aspheric surfaces. The front surface of the first lens is chosen as a rotationally symmetric aspheric surface and surface function is derived such that it collimates the beam in both transverse directions at different beam radius values. The back surface of the first lens and the front surface of the second lens are designed to circularize the beam and transform its irradiance distribution simultaneously. The front surface of the second lens further collimates the beam. The back surface of the second lens is flat in both transverse directions and does not participate in beam shaping since at this surface the beam already has the desired profile. A sketch of the beam shaper is illustrated only in the x-z plane in Figure 4.19. The *y-z* plane sketch is not presented here because the surfaces and their parameter designations used in *y-z* plane are the same with only difference of the *y*-coordinate parameters of the surfaces.

The designed optical system is assumed to reshape the beam without power loss and the conservation of energy principle along a bundle of rays is used to establish mapping of the ray coordinates between the "input reference" and the "output reference" planes, as shown in Figure 4.19 [27]. In order to employ this energy conservation, the input and output beams must have the same planar phase-front. Therefore, the input reference

plane is defined after the front surface of the first lens where the beam is collimated by this surface in both transverse directions (see Figure 4.19).
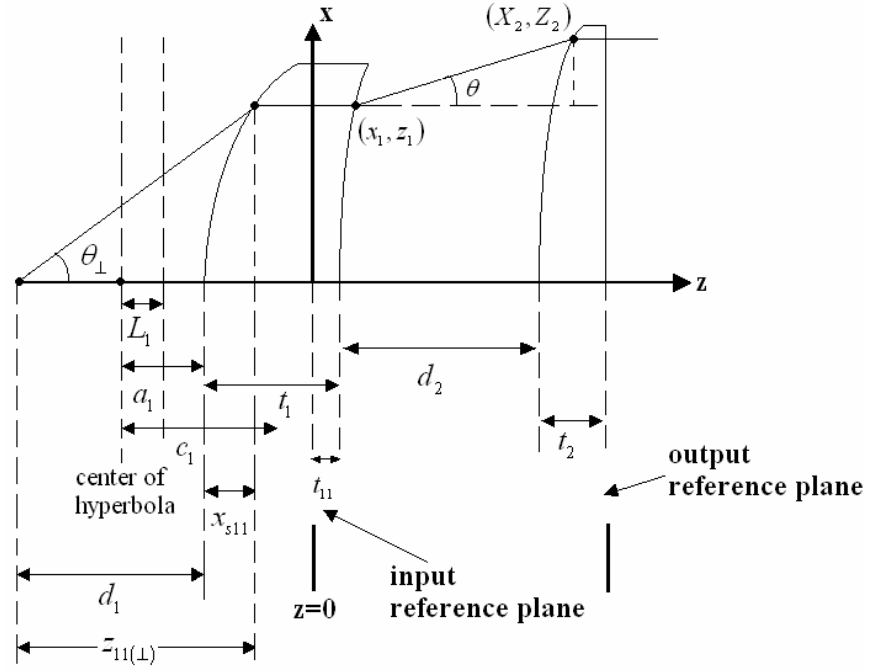
Figure 4.19: Illustration of the general design approach in the x-z plane.

The input beam has a fundamental Gaussian irradiance distribution and the output beam is desired to have a uniform distribution represented by a "square-pulse" beam profile which has a non-zero constant value within a region along x and y coordinates, and zero outside this region. The input irradiance distribution function is given by:

$$I_{in} = I_0 e^{-2\left(\frac{x}{x_0}\right)^2} e^{-2\left(\frac{y}{y_0}\right)^2} \tag{4.62}$$

The desired output irradiance distribution function is chosen as:

$$I_{out} = A_X A_Y \tag{4.63}$$

74

where I_0 is the arbitrary amplitude of input beam and A_X and A_Y are the constant values of the square-pulse function in the perpendicular and parallel transverse directions. I_0 is chosen to be unity (1) in this design method.

For these input and output beam profiles, conservation of energy principle provides a relationship for any arbitrary ray between the ray heights x_1 and X_2, which are designated as the height coordinates in the perpendicular direction for the back surface of the first lens and the front surface of the second lens respectively (see Figure 4.19), as applied in [27]. Lower case x and z are used for the first lens and upper case X and Z are used for the second lens coordinates. The energy conservation between the input reference plane and output reference plane used in the design is given in Equations 4.64 and 4.65:

$$I_{in}\,dxdy = I_{out}\,dXdY \qquad \Rightarrow \qquad E_{in} = E_{out} \tag{4.64}$$

$$E_{in} = \int_{-xmax}^{xmax} e^{-2\left(\frac{x}{x_0}\right)^2} dx \int_{-ymax}^{ymax} e^{-2\left(\frac{y}{y_0}\right)^2} dy = E_{out} = \int_{-Xmax}^{Xmax} A_X dX \int_{-Ymax}^{Ymax} A_Y dY \tag{4.65}$$

where E_{in} and E_{out} are the input and output energies, xmax and ymax are the "working aperture" values of the first lens, Xmax and Ymax are the "working aperture" values of the second lens, x_0 and y_0 are the radii of the beam after being collimated at the front surface of the first lens in the perpendicular and parallel transverse directions, respectively. Because the x and y coordinates are independent of each other and the beam propagation is decoupled to two orthogonal planes, the x and y coordinate variables are calculated independently in Equation 4.65.

75

Power transmission was given by $\dfrac{P_a}{P_T} = 1 - e^{-2a^2/w^2(z)}$ in Equation 4.37 earlier. In this

design method, the aperture radius of the first lens is chosen such that the lens collects

99.78% of the input energy. $a = \mathrm{xmax}$ and $w(z) = x_0$ values are substituted in Equation

4.37. From this, $\mathrm{xmax} = 1.75x_0$ and $\mathrm{ymax} = 1.75y_0$ values are found for 99.78% energy

transmission. Xmax must be equal to Ymax for a square output beam profile. Thus,

$\mathrm{Xmax} = \mathrm{Ymax} = 2x_0$ is arbitrarily chosen in this study.

Once y_0, xmax, ymax, Xmax, and Ymax values are determined, A_X and A_Y

values can be found as follows:

$$A_X = \frac{\sqrt{2\pi}}{4}\frac{x_0}{\mathrm{Xmax}}\,\mathrm{erf}\!\left(2\sqrt{2}\,\frac{\mathrm{xmax}}{x_0}\right) \tag{4.66}$$

$$A_Y = \frac{\sqrt{2\pi}}{4}\frac{y_0}{\mathrm{Ymax}}\,\mathrm{erf}\!\left(2\sqrt{2}\,\frac{\mathrm{ymax}}{y_0}\right) \tag{4.67}$$

As a result, the output beam irradiance profile constant value (I_{out}) that satisfies the

conservation of energy principle can be found as:

$$I_{out} = A_X A_Y = \frac{\pi}{8}\frac{x_0}{\mathrm{Xmax}}\frac{y_0}{\mathrm{Ymax}}\,\mathrm{erf}\!\left(2\sqrt{2}\,\frac{\mathrm{xmax}}{x_0}\right)\mathrm{erf}\!\left(2\sqrt{2}\,\frac{\mathrm{ymax}}{y_0}\right) \tag{4.68}$$

For these input and output beam profiles, conservation of energy principle also

provides a relationship for any arbitrary ray between the ray heights x_1 and X_2, which

are designated as the height coordinates in the perpendicular direction for the back

surface of the first lens and the front surface of the second lens respectively (also see

Figure 4.19), as in [27]. This relationship can be determined with the following

equations:

$$\int_0^{x_1} e^{-2\left(\frac{x}{x_0}\right)^2} dx = \int_0^{X_2} A_X \, dX \qquad (4.69)$$

$$\int_0^{y_1} e^{-2\left(\frac{y}{y_0}\right)^2} dy = \int_0^{Y_2} A_Y \, dY \qquad (4.70)$$

Solving Equations 4.69 and 4.70 for X_2 and Y_2 provide the functions of $X_2(x_1)$ and $Y_2(y_1)$, as seen in Equations 4.71 and 4.72. As a result of these functions, for each x_1 and y_1 values, the corresponding X_2 and Y_2 values are found.

$$X_2(x_1) = \text{Xmax} \frac{\text{erf}\left(2\sqrt{2}\,\frac{x}{x_0}\right)}{\text{erf}\left(2\sqrt{2}\,\frac{\text{xmax}}{x_0}\right)} \qquad (4.71)$$

$$Y_2(y_1) = \text{Ymax} \frac{\text{erf}\left(2\sqrt{2}\,\frac{y}{y_0}\right)}{\text{erf}\left(2\sqrt{2}\,\frac{\text{ymax}}{y_0}\right)} \qquad (4.72)$$

It is assumed that the front surface of the first lens collimates the beam at a beam radius of $x_0 = w_f/2$ cm (x-z plane derivation). The distance d_1 is found solving following equations (Equations 4.73 and 4.74 are obtained from a trigonometric relationship and the constant optical path length condition, respectively):

$$z_{11(\perp)} = \frac{x_0}{\tan(\theta_\perp)} \qquad (4.73)$$

$$n_0\left(z_{11(\perp)} - x_{s11}\right) + n x_{s11} = n_0 \sqrt{w_f^2 + z_{11(\perp)}^2} \qquad (4.74)$$

$$d_1 = z_{11(\perp)} - x_{s11} \qquad (4.75)$$

77

Based on the chosen x_0 value, the y_0 value is found solving following equations:

$$n_0 d_1 + n y_{s11} = n_0 \sqrt{y_0^2 + (d_1 + y_{s11})^2} \qquad (4.76)$$

$$\tan(\theta_\parallel) = \frac{y_0}{d_1 + y_{s11}} \qquad (4.77)$$

The radius of curvature value of the first lens front surface is found using the general refraction equation that is only valid for paraxial rays for a given refractive index for spherical surfaces given by Equation 4.38. Once the radius of curvature is determined, the conic constant of this surface is determined using the hyperbola definition. As stated earlier, this surface collimates the beam under the condition that the astigmatism is neglected. As shown in Figure 4.19 (also in the equations below), L is designated as the directrix of the conic section, e is eccentricity of the conic section, a is the semi-major axis parameter, b is the semi-minor axis parameter, $c = \sqrt{a^2 + b^2}$, and the subscript 1 in the variables refers to "first lens" parameters.

$$\frac{\sqrt{(z_{11(\perp)} - (d_1 - a_1) - c_1)^2 + x_0^2}}{(a_1 - L_1 + x_{s11})} = e_1 \qquad (4.78a)$$

$$R_1 = \frac{b_1^2}{a_1} \qquad (4.78b)$$

$$c_1 = \sqrt{a_1^2 + b_1^2} = \sqrt{a_1^2 + a_1 R_1} \qquad (4.78c)$$

$$e_1 = \frac{c_1}{a_1} = \frac{\sqrt{a_1^2 + a_1 R_1}}{a_1} \qquad (4.78d)$$

$$L_1 = \frac{a_1^2}{c_1} = \frac{a_1^2}{\sqrt{a_1^2 + a_1 R_1}} \qquad (4.78e)$$

78

Substituting Equations 4.78b – 4.78e in Equation 4.78a, the following equation is obtained:

$$\frac{\sqrt{\left(x_{s11} + a_1 - \sqrt{a_1^2 + a_1 R_1}\right)^2 + x_0^2}}{\left(a_1 - \dfrac{a_1^2}{\sqrt{a_1^2 + a_1 R_1}} + x_{s11}\right)} = \frac{\sqrt{a_1^2 + a_1 R_1}}{a_1} \qquad (4.79)$$

a_1 is determined solving the above equation. Then, b_1 is found solving Equation 4.78b. Then the conic constant of the hyperbola is found using Equation 4.80:

$$K_1 = -1 - \frac{b_1^2}{a_1^2} \qquad (4.80)$$

The next step is to determine the parameters of the back surface of the first lens and the front surface of the second lens.

In order for the output reference plane to have the same phasefront as the input reference plane, it is necessary for all the rays traced between these planes to have the same optical path length according to Fermat's Principle [78]. Using this fact, the following equations are only derived in terms of perpendicular transverse direction because they are the same for the parallel direction. The origin of the z-axis is fixed at the reference input plane, as seen in Figure 4.19.

The optical path length of a ray passing along the optical axis is:

$$\text{OPL}_o = n(t_{11}) + n_0 d_2 + nt_2 \qquad (4.81)$$

The optical path length of an arbitrary ray crossing the x-coordinate at a point, x_1, is given by:

$$\text{OPL}_x = nz_1 + n_0 \left[(X_2 - x_1)^2 + (Z_2 - z_1)^2\right]^{1/2} + n(t_{11} + d_2 + t_2 - Z_2) \qquad (4.82)$$

79

where, (x_1, z_1) and (X_2, Z_2) are the coordinates of an arbitrary ray location at the back surface of the first lens and the front surface of the second lens, respectively. The constant optical path length condition requires that $OPL_0 = OPL_x$. Using this, an equation for $(Z_2 - z_1)$ in terms of $(X_2 - x_1)$ is obtained, as in [27] and it is given by:

$$(Z_2 - z_1) = \frac{nd_2(n - n_0) \mp n_0 \left[d_2^2(n - n_0)^2 + (n^2 - n_0^2)(X_2 - x_1)^2 \right]^{1/2}}{n^2 - n_0^2} \tag{4.83}$$

According to Snell's Law the rays are refracted at the back surface of the first lens. Also using geometrical relation shown in Figure 4.20, the following equations are obtained:

$$\theta_r = \arcsin\left(\frac{n}{n_0} \sin\theta_i \right) \tag{4.84}$$

$$\tan\theta = \tan(\theta_r - \theta_i) = \frac{X_2 - x_1}{Z_2 - z_1} \tag{4.85}$$

By substitution, Equation 4.86 is obtained:

$$\theta_i = \arctan\left[\frac{n_0(X_2 - x_1)}{n\left[(X_2 - x_1)^2 + (Z_2 - z_1)^2 \right]^{1/2} - d_2 n_0} \right] \tag{4.86}$$
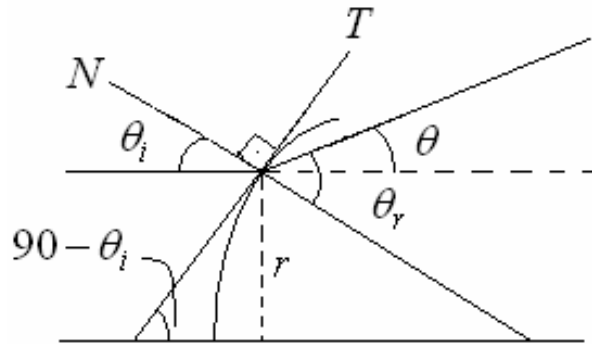
Figure 4.20: Illustration of the back surface of the first lens, together with its tangent and normal lines and the incident and refracted angle definitions.

80

This method allows determining the angle θ_i and the slope of any tangent line (m_T) on this surface for the coordinates x_1 of each ray on the x-axis by sampling between 0 and xmax coordinate points. The slope equation is given by:

$$m_T = \tan(90 - \theta_i) \tag{4.87}$$

Once the m_T values between each ray point are calculated with the equations presented above, these points are connected to form the surface function of the back surface of the first lens. If the number of traced rays is increased sufficiently, the tangent lines of the surface between these points become an accurate representation of the surface. Using regular slope equation of a line, z_1 coordinates of these traced rays are calculated. After this, the Z_2 coordinates of these rays are calculated using Equation 4.83. The X_2 coordinates are calculated using Equation 4.71. As a result, a coordinate table for both the back surface of the first lens and the front surface of the second lens is determined, as applied in [27].

CHAPTER 5

DESIGN EXAMPLES AND RESULTS

This chapter provides design examples to the systems discussed in Section 4.4, Section 4.5, and Section 4.6. The parameters of each design example are calculated with MATLAB codes developed separately for each design method. The MATLAB and ZEMAX results are presented and discussed separately for each design method in Section 5.1, Section 5.2, and Section 5.3.

5.1 Off-Axis Mirror-Based Optical System Design for Circularization, Collimation, and Expansion of Elliptical Laser Beams

5.1.1 Calculated Parameters of the Examples for the First Design Method

Two examples are presented for the first design method. First one utilizes a laser source with 10° and 30° divergence angles in the parallel and perpendicular transverse directions. Such laser beam is named as 10° - 30° beam. Second example utilizes a laser source with 12° and 46° divergence angles and the beam is named as 12° - 46° beam. Table 5.1 shows the calculated values for the first example of this design method.

These calculated parameters are input in a ray tracing MATLAB code to check if the system is feasible for the 1.4 rays. A MATLAB generated plot tracing 1.4 rays for the system with the parameters in Table 5.1 is displayed in Figure 5.1.

Table 5.1: Parameters of the first example designed with the first mirror-based design method

$\theta_{\parallel}$	$\theta_{\perp}$	α	a (cm)	b (cm)	d (cm)	e (cm)	g (cm)	w_f (cm)
5°	15°	5°	0.96	1.04	0.96	3.96	34.49	10
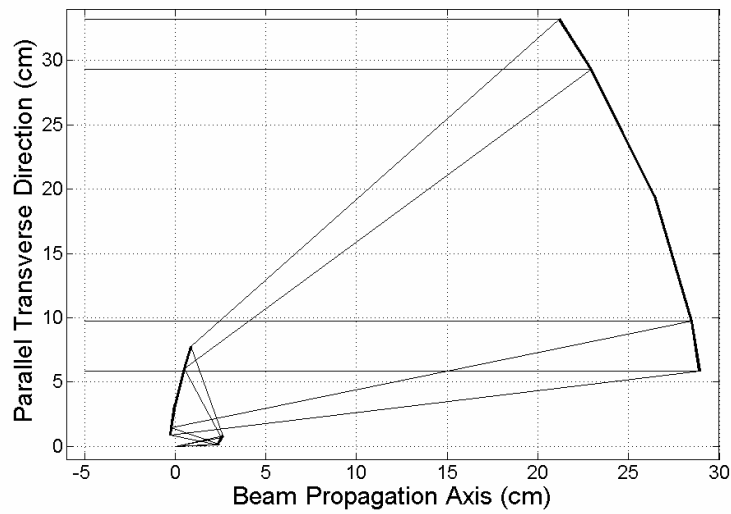
Figure 5.1: MATLAB plot demonstrating the representative beam propagation in the y-z plane for the first design method first example.

In Figure 5.1, the second mirror seems to obscure a portion of the beam reflected from the third mirror. One can increase the field angle to reduce the mirror obscuration. However, this might also increase the aberration level. Displacing the parabolic mirror around the virtual point source at the focal point of this mirror is another method to prevent obscuration on the second mirror. The latter method is preferred in this method to prevent obscuration providing an option to keep the overall system size small rather than changing the system parameters that may increase the system size.

The calculated parameters for the 12° - 46° beam are presented in Table 5.2.

Table 5.2: Parameters of the second example designed with the first mirror-based design method

$\theta_{\parallel}$	$\theta_{\perp}$	α	a (cm)	b (cm)	d (cm)	e (cm)	g (cm)	w_f (cm)
6°	23°	3°	0.75	0.75	0.75	4.89	20.51	10.00

5.1.2 Calculated Parameters of the Example for the Second Design Method

Only a laser beam with $46°$ divergence angle in the perpendicular transverse direction and $12°$ divergence angle in the parallel transverse direction is used as a design example for this design method. The parameters found for this system are given in Table 2-8. Obscuration problem does not exist for the design example using these tabulated parameters. In case of obscuration, rotation and tilt of any mirror is also an option in this design method as in the first design method.

Table 5.3: Parameters of the example designed with the second mirror-based design method

$\theta_{\parallel}$	$\theta_{\perp}$	α	g_1 (cm)	g_2 (cm)	g_3 (cm)	w_f (cm)
6°	23°	5°	2.42	9.36	95.41	10.00

5.1.3 Results

As explained in Section 4.1, geometrical ray optics design approach must be validated that it is a good and valid approximation to physical propagation of a laser

beam through the considered optical system. For this purpose, the dimensionless parameter, β, which provides a quantitative measure of the diffraction effects and the validity of the geometrical ray optics design, is used. As long as the $\beta \gg 1$ condition is satisfied separately in both transverse directions for the first and second mirrors, the geometrical rays are valid to use for design and analysis purposes. Geometrical rays reflected from the third mirror are not used for design or analysis purposes so that the β parameter is not calculated for this collimating mirror. Calculated values of β for the first and second mirrors in each design example are presented in Table 5.4. These values validate the geometrical ray optics approach for these examples.

Table 5.4: β parameter calculations of each studied mirror-based design example, separately for perpendicular and parallel transverse directions

		Design Method I				Design Method II	
		10° - 30° beam		12° - 46° beam		12° - 46° beam	
		x-axis	y-axis	x-axis	y-axis	x-axis	y-axis
First mirror	w_0 (cm)	0.67	0.22	0.80	0.21	1.03	0.26
	w_f (cm)	1.67	1.65	3.15	3.07	1.03	1.00
	d (cm)	3.75	3.75	5.54	5.54	7.08	7.37
	β	2.15e4	7.05e3	3.29e4	8.20e3	1.08e4	2.53e3
Second mirror	w_0 (cm)	1.67	1.65	3.15	3.07	1.03	1.00
	w_f (cm)	10.00	9.94	10.36	10.10	10.34	10.12
	d (cm)	31.08	31.08	17.75	17.75	86.76	86.76
	β	3.88e4	3.81e4	1.33e5	1.25e5	8.86e3	8.42e3

The wavelength and the total power of the laser beam are chosen to be 870 nm. The beam diameter of the laser beam after collimation at the third mirror is chosen to be 20 cm. The beam characteristic values for $10°$ - $30°$ and $12°$ - $46°$ laser beams are also calculated analytically and given in Table 5.5 (where w_f, z_{0f}, θ_f are the expected beam waist, the expected Rayleigh range, and the expected divergence half angle of the final beam circularized and collimated beam respectively).

Table 5.5: Analytical Calculations of the input and output beam for both $10°$ - $30°$ and $12°$ - $46°$ beam examples

	$10°$ - $30°$ beam	$12°$ - $46°$ beam
$w_{0\parallel}$	3.18 µm	2.64 µm
$w_{0\perp}$	1.06 µm	0.69 µm
$z_{0\parallel}$	36.32 µm	25.30 µm
$z_{0\perp}$	4.04 µm	1.72 µm
$w_{f(\parallel,\perp)}$	10.00 cm	10.00 cm
$z_{0f(\parallel,\perp)}$	36.11 km	36.11 km
$\theta_{f(\parallel,\perp)}$	2.77 µrad	2.77 µrad

"Physical Optics Propagation" tool results for the first design method $10°$ - $30°$ and the $12°$ - $46°$ beam examples, and the second design method $12°$ - $46°$ beam example are displayed in Figure 5.2, Figure 5.3, and Figure 5.4 respectively. In these figures, the input beam spots are determined at the laser source exit. The output beam spots are determined after reflection from the collimating parabolic mirror (the "exit plane"),

0.5km away from the exit plane, and 1km away from the exit plane respectively. The figure image sizes are 4 μm x 10 μm for the input beams and 40 cm x 40 cm for the output beams for each example.

The quantitative results are presented in Table 5.6. These values are given separately for the two transverse directions because there is no such thing as perfect circularization. Thus, this table also summarizes the circularization and collimation effectiveness for each design example when compared to Table 5.5. The results presented in these tables reveal that the beams are circularized and collimated satisfactorily.

Table 5.6: Output beam results of all studied mirror-based design examples

	10° - 30° beam first design method	12° - 46° beam first design method	12° - 46° beam second design method
$w_{f\parallel}$	9.94 cm	10.10 cm	10.12 cm
$w_{f\perp}$	10 cm	10.36 cm	10.34 cm
$z_{0f\parallel}$	35.70 km	36.49 km	38.56 km
$z_{0f\perp}$	36.12 km	37.46 km	36.79 km
$\theta_{f\parallel}$	2.79 μrad	2.74 μrad	2.74 μrad
$\theta_{f\perp}$	2.77 μrad	2.67 μrad	2.68 μrad

87

Figure 5.2: First mirror-based design method 10°- 30° beam example for the stated image sizes a) input (4 μm x 10 μm) b) output (40 cm x 40 cm) c) output at 0.5 km distance (40 cm x 40 cm) d) output at 1 km distance (40 cm x 40 cm).
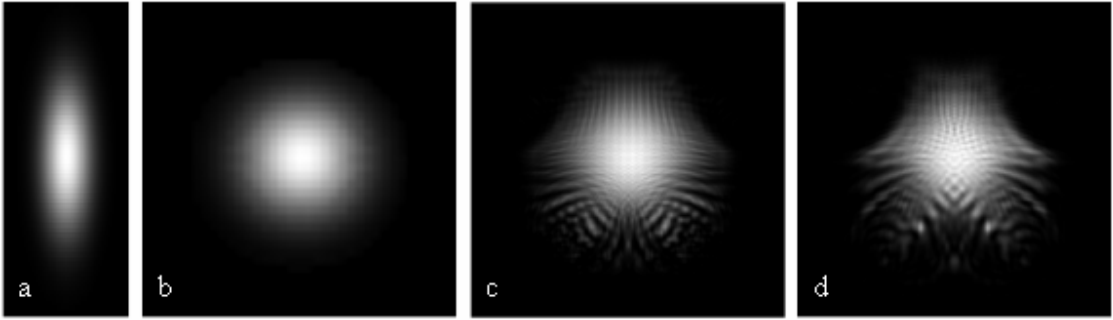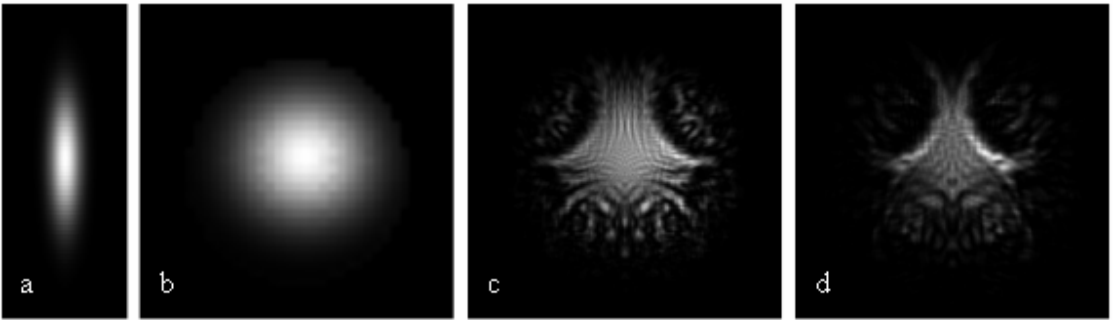

Figure 5.3: First mirror-based design method 12°- 46° beam example for the stated image sizes a) input (4 μm x 10 μm) b) output (40 cm x 40 cm) c) output at 0.5 km distance (40 cm x 40 cm) d) output at 1 km distance (40 cm x 40 cm).
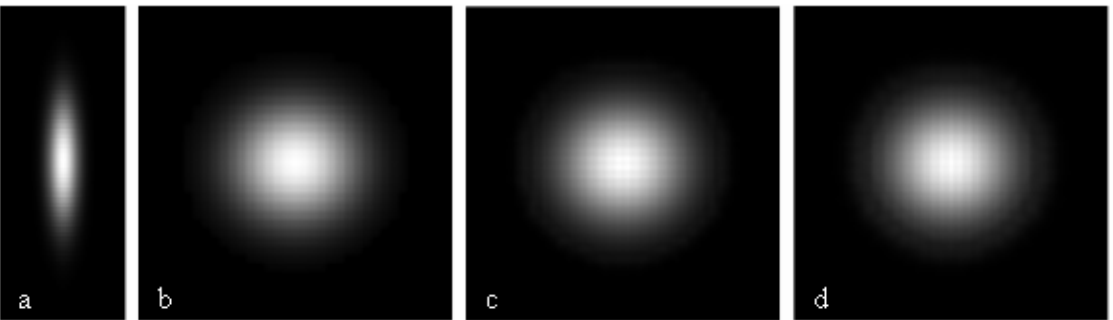

Figure 5.4: Second mirror-based design method 12°- 46° beam example for the stated image sizes a) input (4 μm x 10 μm) b) output (40 cm x 40 cm) c) output at 0.5 km distance (40 cm x 40 cm) d) output at 1 km distance (40 cm x 40 cm).

As stated earlier, in the first design, the beam reflected at the second mirror propagates to the collimating parabolic mirror with a divergence angle that is equal to the input beam perpendicular divergence angle. Thus, one can expect that the level of aberrations introduced by the optical system to increase with the increasing values of $\theta_\perp$, as seen comparing Figure 5.2 and Figure 5.3. These results reveal that the first design method can not be efficiently used in the far field region for large $\theta_\perp$ values. This problem is less significant in the second design method because the beam reflected at the second mirror propagates to the collimating parabolic mirror with a divergence angle that is equal to the input beam parallel divergence angle. Given that generally $\theta_\parallel$ is quite low compared to $\theta_\perp$, the aberrations introduced by the second method are less significant in the second method. This is proved with the results displayed in Figure 5.4.

5.2 Aspherical Lens-Based Optical System Design for Circularization, Collimation, and Expansion of Elliptical Laser Beams

5.2.1 Calculated Parameters of the Example for the Two-Lens Design Method

One example is presented for the first design method utilizing a 12° - 46° beam. The beam (waist) radius w_f at the exit of the optical system is a design constraint and chosen as 2.0 cm. The other variables, namely the initial divergence angles, $\theta_\parallel$, $\theta_\perp$, are the known quantities, and are based on the characteristics of a laser commercially available. The lens thicknesses t_1, t_2, and w_f are analytically calculated values, and are the input parameters of the MATLAB code calculating d_1, d_2, $R_{11\perp}$, $R_{12\perp}$, $R_{21\parallel}$. The

remaining radii of curvatures are not calculated since the corresponding surfaces are optically flat. All parameters are presented in Table 5.7.

Table 5.7: Two-lens system design example parameters

Given Quantities		Calculated quantities						Constraints	
$\theta_\perp$	$\theta_\parallel$	t_1 (cm)	t_2 (cm)	d_1 (cm)	$R_{11\perp}$, $R_{11\parallel}$ (cm)	$R_{12\parallel}$ (cm)	$R_{21\parallel}$ (cm)	d_2 (cm)	w_f (cm)
23°	6°	2.00	0.70	3.91	1.99	2.01	9.65	15.00	2.00
					$K_{11\perp}$, $K_{11\parallel}$	$K_{12\parallel}$	$K_{21\parallel}$		
					-2.28	-2.28	-2.28		

5.2.2 Calculated Parameters of the Example for the Single-Lens Design Method

One example is presented for the first design method utilizing a $12°$ - $46°$ beam. The beam (waist) radius w_f at the exit of the optical system is again a design constraint and chosen as 2.0 cm. All parameters are presented in Table 5.8.

Table 5.8: Single-lens system design example parameters

Given Quantities		Calculated quantities				Constraints	
$\theta_\perp$	$\theta_\parallel$	d(cm)	$R_{1\perp}$ (cm)	$R_{1\parallel}$ (cm)	$R_{2\parallel}$ (cm)	t (cm)	w_f (cm)
23°	6°	3.91	1.99	-2.48	-5.49	13.00	2.00
			$K_{1\perp}$	$K_{1\parallel}$	$K_{2\parallel}$		
			-2.28	0.04	-0.44		

5.2.3 Results

To verify that the $\beta \gg 1$ condition is satisfied, the β parameters for each surface, separately in the *x-z* and *y-z* planes, are calculated based on the calculated surface parameters and the surface distances for both design methods. These values are given in Table 5.9 and 5.10 for the two-lens and single-lens systems, respectively. From the values presented in these tables, it is conformed that the use of the geometrical ray optics approach for these examples is a valid approximation.

Both design methods circularize and collimate an elliptical laser beam satisfactorily. This can also be seen in ray tracing results in *x-z* and *y-z* planes for the first and second design methods, presented in Figure 5.5 and Figure 5.6, respectively. These figures are determined with a MATLAB code developed to simulate the beam propagation with the ray tracing method. The ray tracing results obtained using ZEMAX are presented in Figure 5.7 for two-lens system and in Figure 5.8 for single-lens system.

The wavelength and the total power of the laser beam are chosen to be 870 nm and 30 W respectively. This is a commercially available semiconductor laser with approximately 2.64 x 0.69 μm beam spot size at the laser output. The beam diameter of the laser beam after collimation at the optical system output for both designs is chosen to be 2.0 cm as stated earlier. Based on this laser beam, the system parameters are calculated analytically and presented in Table 5.11 where w_f, z_{0f}, θ_f are the expected beam waist, the expected Rayleigh range, and the expected divergence half angle of the final circularized and collimated beam respectively. $\theta_{f(\|,\perp)} = 13.89$ μrad is the diffraction limit for a beam with a radius of 2.0 cm.

91

Table 5.9: β parameter calculations for the first lens-based design method example separately for perpendicular and parallel transverse directions

		x-axis	y-axis
First lens front surface	w_{i11} (cm)	2.00	0.42
	w_{o12} (cm)	2.00	0.42
	d (cm)	2.00	2.00
	β	1.44e5	6.25e3
First lens back surface	w_{i12} (cm)	2.00	0.42
	w_{o21} (cm)	2.00	2.00
	d (cm)	15.00	15.00
	β	1.92e4	4.00e3
Second lens front surface	w_{i21} (cm)	2.00	2.00
	w_{o22} (cm)	2.00	2.00
	d (cm)	0.70	0.70
	β	4.12e5	4.12e5

Table 5.10: β parameter calculations for the second lens-based design method example separately for perpendicular and parallel transverse directions

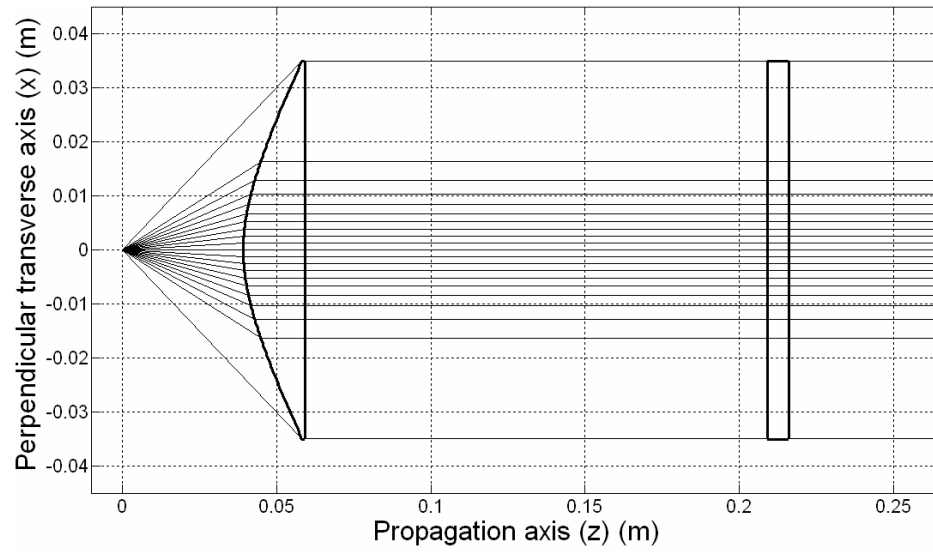|		x-axis	y-axis
Front surface	w_{i1} (cm)	2.00	0.41
	w_{o2} (cm)	2.00	2.00
	d (cm)	13.00	13.00
	β	2.22e4	4.53e4

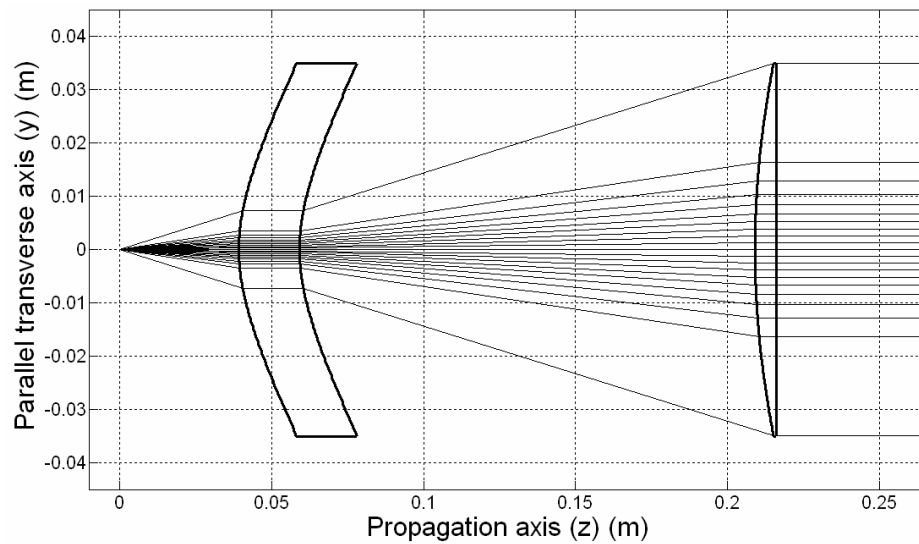Figure 5.5(a): Ray tracing results for the first lens-based design method in the x-z plane.

Figure 5.5(b): Ray tracing results for the first lens-based design method in the y-z plane.

Figure 5.6(a): Ray tracing results for the second lens-based design method in the x-z plane.

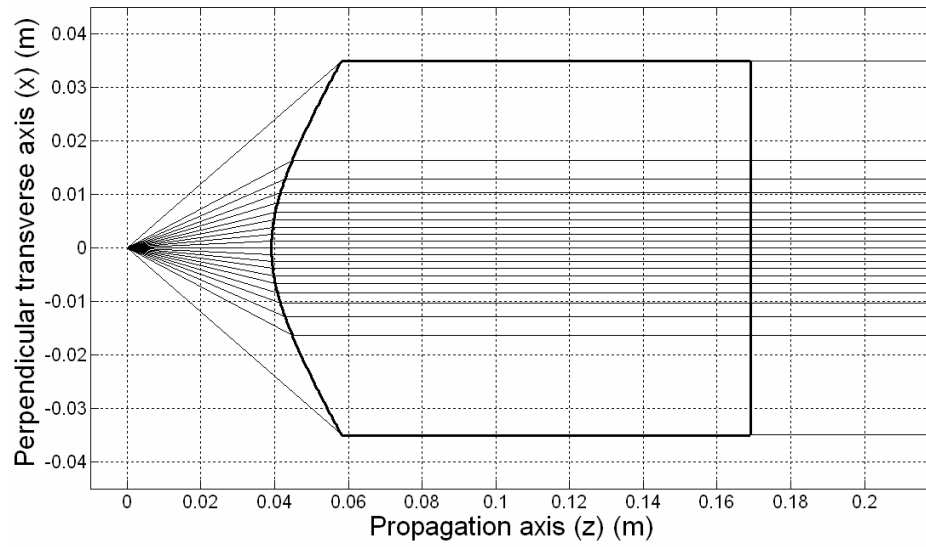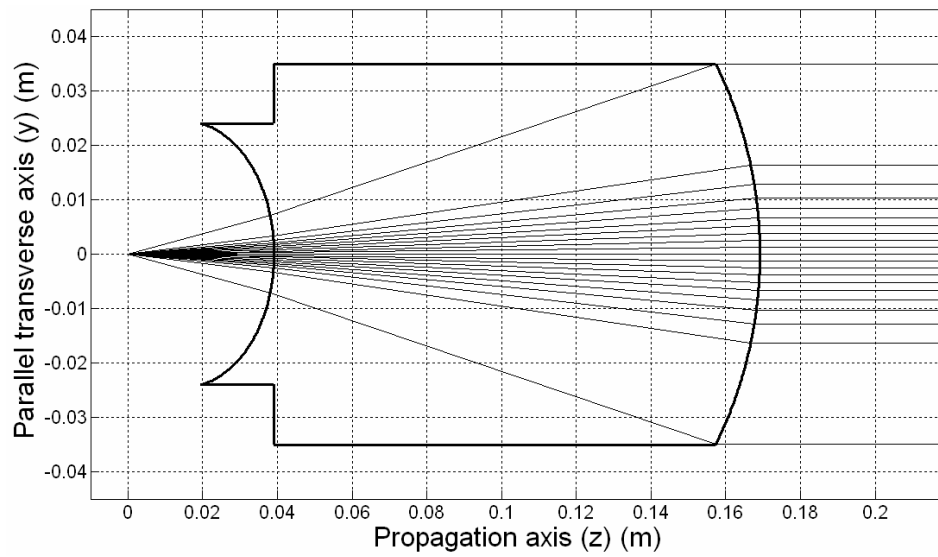Figure 5.6(b): Ray tracing results for the second lens-based design method in the y-z plane.
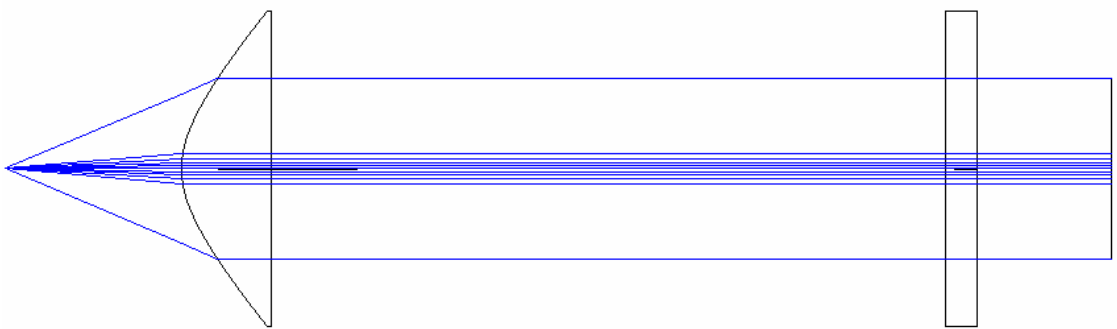
94

Figure 5.7(a): Ray tracing results obtained with ZEMAX for the two-lens system in the x-z plane.
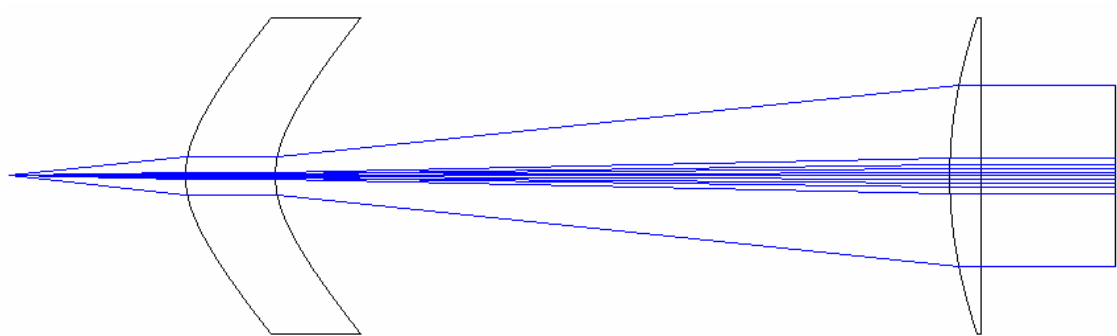

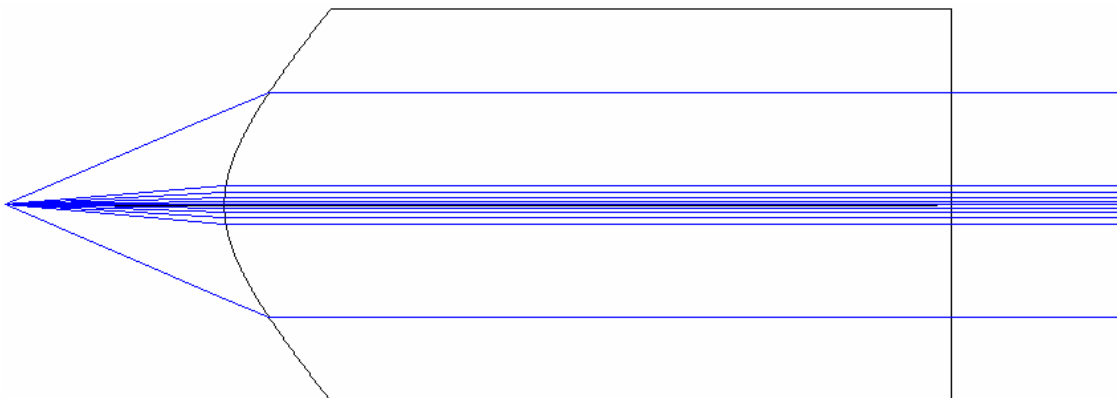Figure 5.7(b): Ray tracing results obtained with ZEMAX for the two-lens system in the y-z plane.

Figure 5.8(a): Ray tracing results obtained with ZEMAX for the single-lens system in the x-z plane.
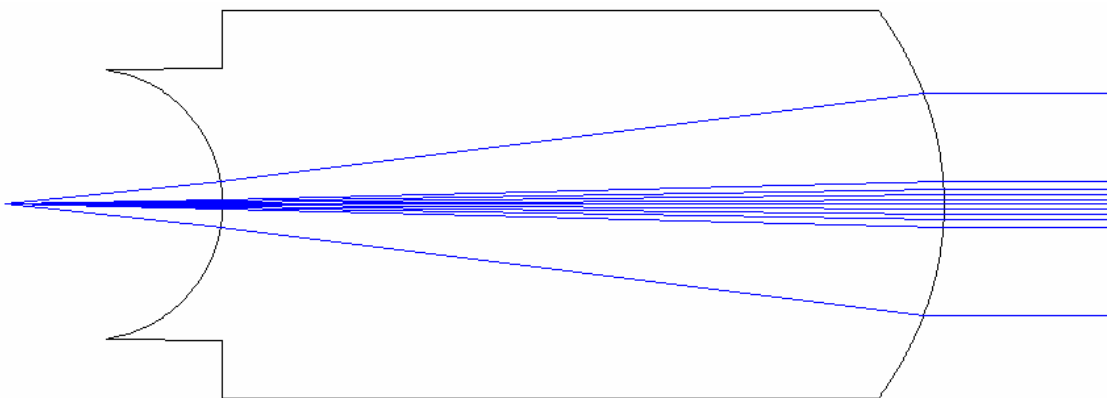
Figure 5.8(b): Ray tracing results obtained with ZEMAX for the single-lens system in the y-z plane.

ZEMAX physical beam propagation results are presented in Figure 5.9 and Figure 5.10. In these figures, the input beam spots are determined at the laser source exit and the output beam spots are determined at the optical system exit plane and 1 km away from the exit plane. The figure image sizes are 4 μm x 10 μm for the input beam and 8 cm x 8 cm for the output beams. One important note is that the ZEMAX Physical Optics Propagation tool may not provide precise results for large beam divergence angles and highly curved refractive surfaces. For such design examples, the beam spots recommended to be analyzed together with ray tracing results. In this design example, the beam divergence angle is 46° in the perpendicular transverse direction and the surfaces are highly curved. Therefore, the beam spots seem to be slightly elliptical in Figure 5.9 and Figure 5.10, which are slightly different than the ray tracing results presented in Figure 5.5 and Figure 5.6. The author believes that this minor difference is attributed to the ZEMAX code's limitations for highly divergent beams and highly

curved surfaces. Regardless of the minor deviations, MATLAB results and ZEMAX results are in agreement.

In comparison, second design method seems to be more practical than the first one since there is only one lens and it might be easier to align a single-lens system than to align a two-lens system in a laboratory environment. However, two-lens system has more degrees of freedom and, therefore, the optical parameters can be more widely adjusted. Also considering the size of it, it may get bulky and hard to use in the laboratory environment. The overall system length is smaller (21.61 cm for the two-lens example, where as 16.91 cm for the single lens example) for the second method for these particular examples. However, this does not have a significant meaning since the distance between the lenses in the two-lens system is an input parameter and can be selected differently, if desired.

On the other hand, the two-lens system becomes more practical for large difference between the transverse divergence angles and large output beam spot, w_f. If such scenario is present, then, the lens thickness in the single-lens system method needs to be increased to accommodate the requirements. The beam can be further expanded if required in both design methods. Increasing the output beam's diameter reduces the divergence angle and increases the Rayleigh range of the output beam.
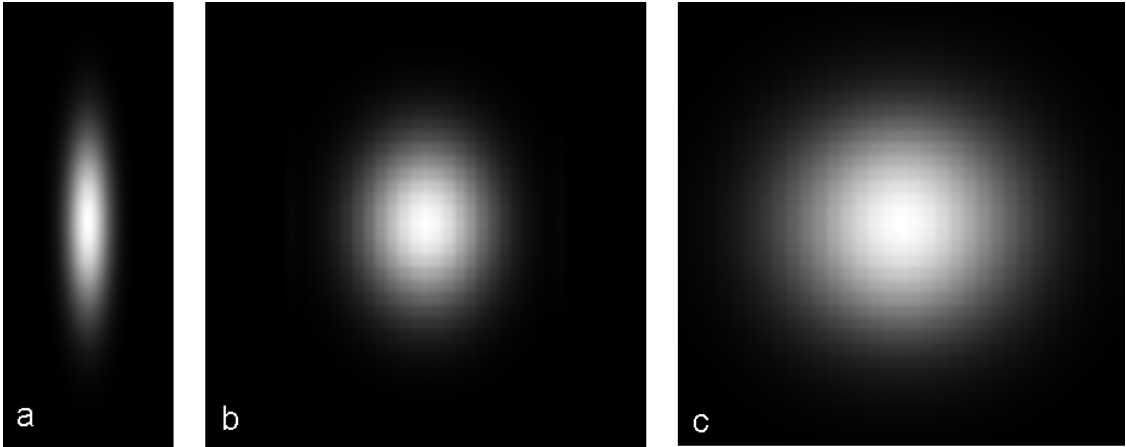
Figure 5.9: Two-lens system ZEMAX plots a) input beam (window size: 4 μm x 10 μm) b) output beam at the system exit plane (window size: 8 cm x 8 cm) c) output beam at 1 km distance (window size: 8 cm x 8 cm).
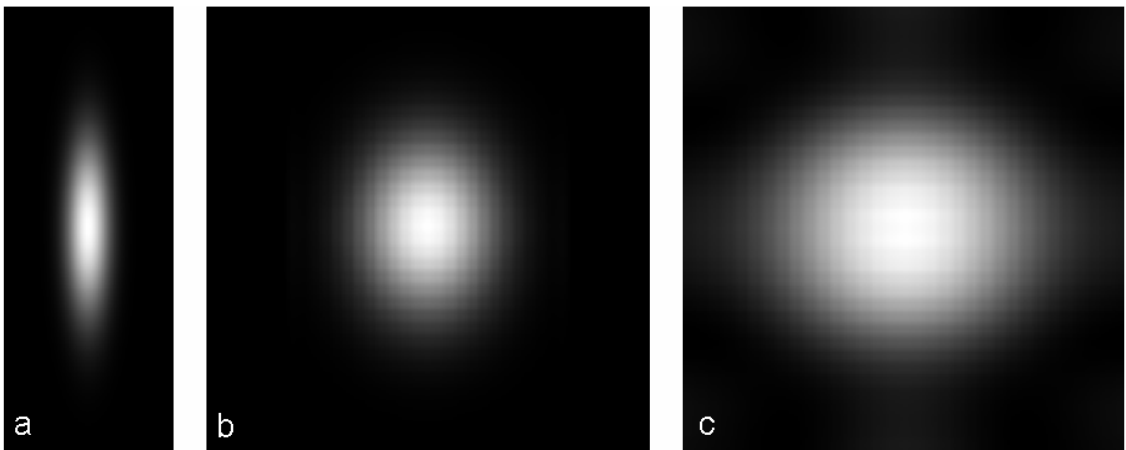

Figure 5.10: Single-lens system ZEMAX plots a) input beam (window size: 4 μm x 10 μm) b) output beam at the system exit plane (window size: 8 cm x 8 cm) c) output beam at 1 km distance (window size: 8 cm x 8 cm).

5.3 Reshaping an Elliptically Diverging Gaussian Laser Beam into a Circular, Collimated, and Expanded Uniform Beam with Aspherical Lens Design

5.3.1 Calculated Parameters of the Design Example

Table 5.11 displays the β parameter calculations of the studied design example separately for the perpendicular and parallel transverse directions design proving that the geometrical ray optics is a good approximation to physical optics propagation. The input values of the lenses and the beam characteristics are also pre-determined as shown in Table 5.12.

Table 5.11: β parameter calculations of the studied design example separately for perpendicular and parallel transverse directions

	w_0 (cm)	w_f (cm)	d (cm)	β
Perpendicular transverse direction	1.00	2.00	10.00	14444
Parallel transverse direction	0.21	2.00	10.00	3033

Table 5.12: Input variables and values used in the design example.

Laser Parameters		Lens Parameters		Beam Size at Reference Planes	
Wavelength	Divergence Angles	Lens Material	Lens Thickness Values	Input Plane	Output Plane
870 nm	$\theta_\perp = 23°$	BK7 glass n=1.5095 at 870 nm	$t_1 = 1.50$ cm	$x_0 = 1.00$ cm	Xmax $= 2.00$ cm
	$\theta_\parallel = 6°$		$t_2 = 1.50$ cm	$y_0 = 0.21$ cm	Ymax $= 2.00$ cm

The distance $d_1 = 1.96$ cm is determined by choosing $x_0 = 1$ cm after the beam is being collimated at the front surface of the first lens. Also the distance between the two lenses is chosen as $d_2 = 10$ cm. Based on the pre-determined x_0 and y_0 values, the

$xmax = 1.75$ cm and $ymax = 0.37$ cm values are calculated as the working aperture values of the first lens in the two transverse directions. The calculated values of the front surface of the first lens parameter are $R = 1.0$ cm (the radius of curvature value) and $K = -2.28$ (the conic constant value) in both transverse directions. The back surface of the second lens is flat, as mentioned earlier. In Table 5.13, the calculated parameters of the first lens back surface and the second lens front surface are tabulated for this design example.

Table 5.13: Calculated first lens front surface and second lens back surface function parameters

	First Lens – Back Surface		Second Lens – Front Surface	
	x-direction	y-direction	x-direction	y-direction
Radius (cm)	2.34	0.36	7.43	5.47
Conic Constant	-1.50	-7.70	-1.50	-2.50
4th order term (cm^{-3})	-9.06e-2	n/a	-2.89e-4	n/a
6th order term (cm^{-3})	1.16e-4	n/a	-1.12e-5	n/a
8th order term (cm^{-3})	1.42e-6	n/a	2.98e-8	n/a
10th order term (cm^{-3})	-7.29e-9	n/a	9.35e-12	n/a
12th order term (cm^{-3})	1.02e-11	n/a	-1.06e-13	n/a

5.3.2 Results

Once the surface characteristics of both lenses are determined, the ray tracing is computed by the MATLAB code. Figure 5.11(a) and Figure 5.11(b) display the two lenses and the rays traced in x-z and y-z planes based on the model. Total of 21 rays are traced, as in the previous section. As it can be seen in these figures, the input beam has

Gaussian irradiance distribution; whereas, the output beam has uniform beam with a constant coordinate difference between each traced ray.

In Figure 5.12(a), Figure 5.12(b), and Figure 5.12(c), the beam profiles at the laser output, the beam shaper input reference plane, and the output reference planes are plotted using MATLAB. To test the design model, the normalized irradiance distribution of the beam at five different locations in between the two lenses using the "coordinate" maps of the traced rays is plotted, as shown in Figure 5.13. These distributions are obtained back-tracing the rays from the output reference plane to the input reference plane with the help of coordinate transformation equations derived in Section 4.6. Because the model is developed in two independent transverse directions, the irradiance distributions are also plotted in these two transverse coordinates for positive values only.
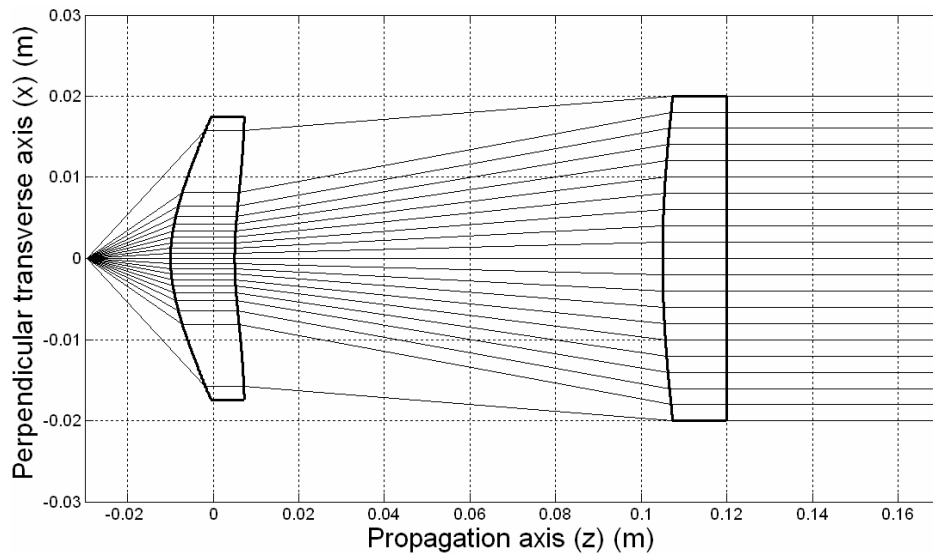
Figure 5.11(a): Ray tracing results in x-z plane.
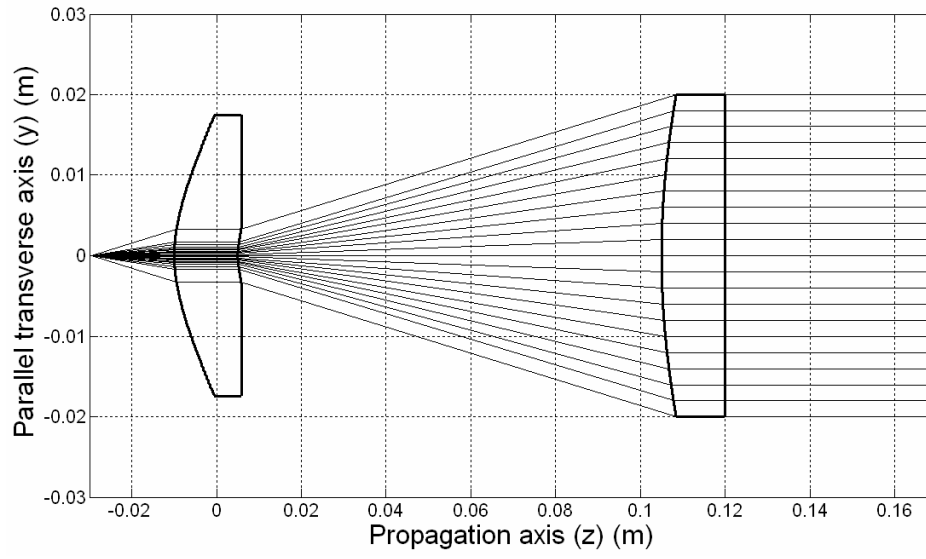
Figure 5.11(b): Ray tracing results in the y-z plane.
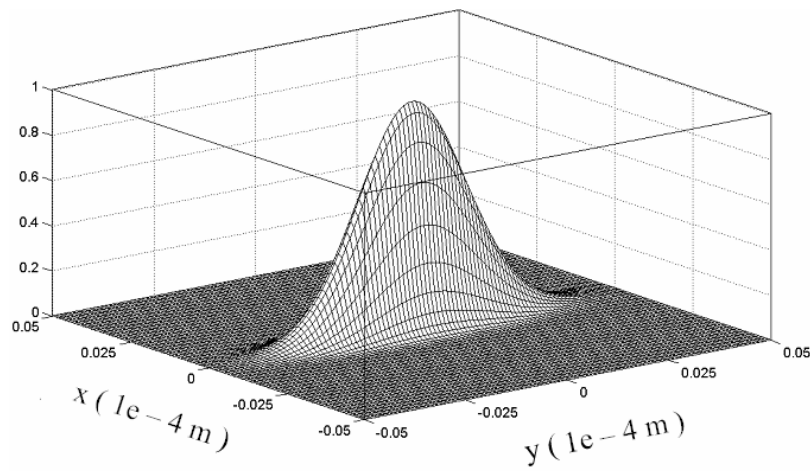
Figure 5.12(a): Irradiance distribution at the laser output plane.
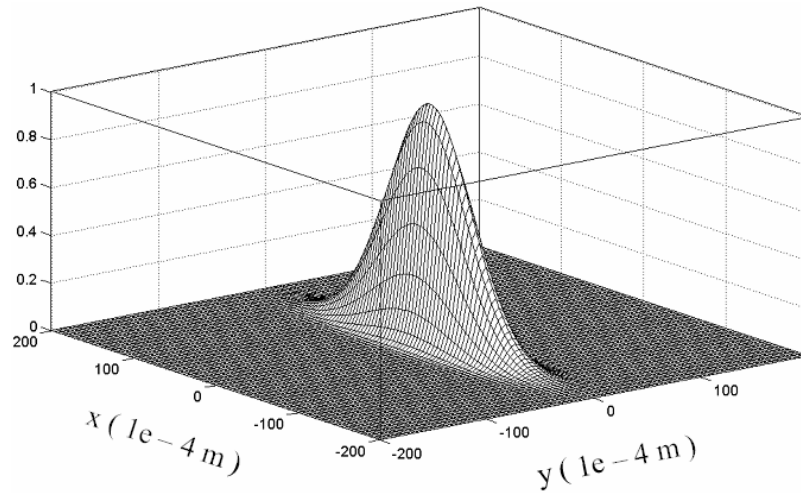
Figure 5.12(b): Irradiance distribution at the input reference plane.
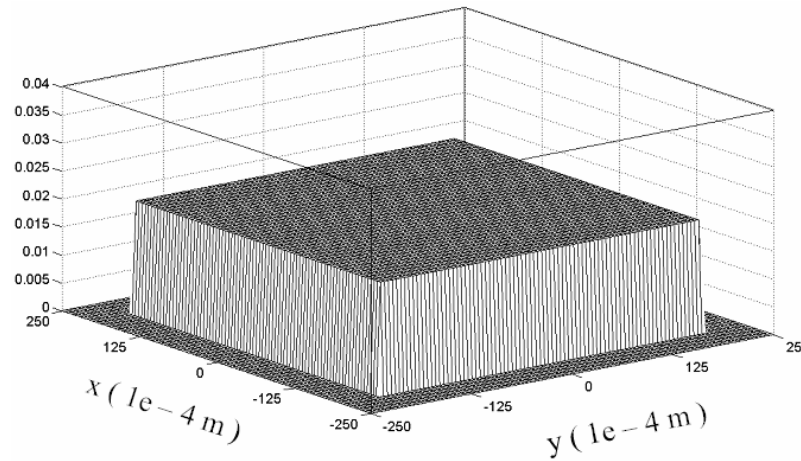
Figure 5.12(c): Irradiance distribution at the output reference plane.

Parallel Direction (y)	Perpendicular Direction (x)
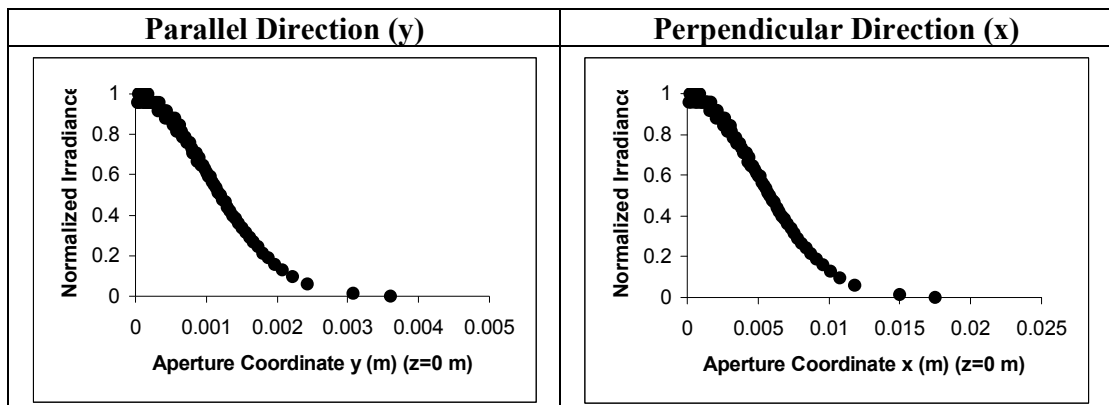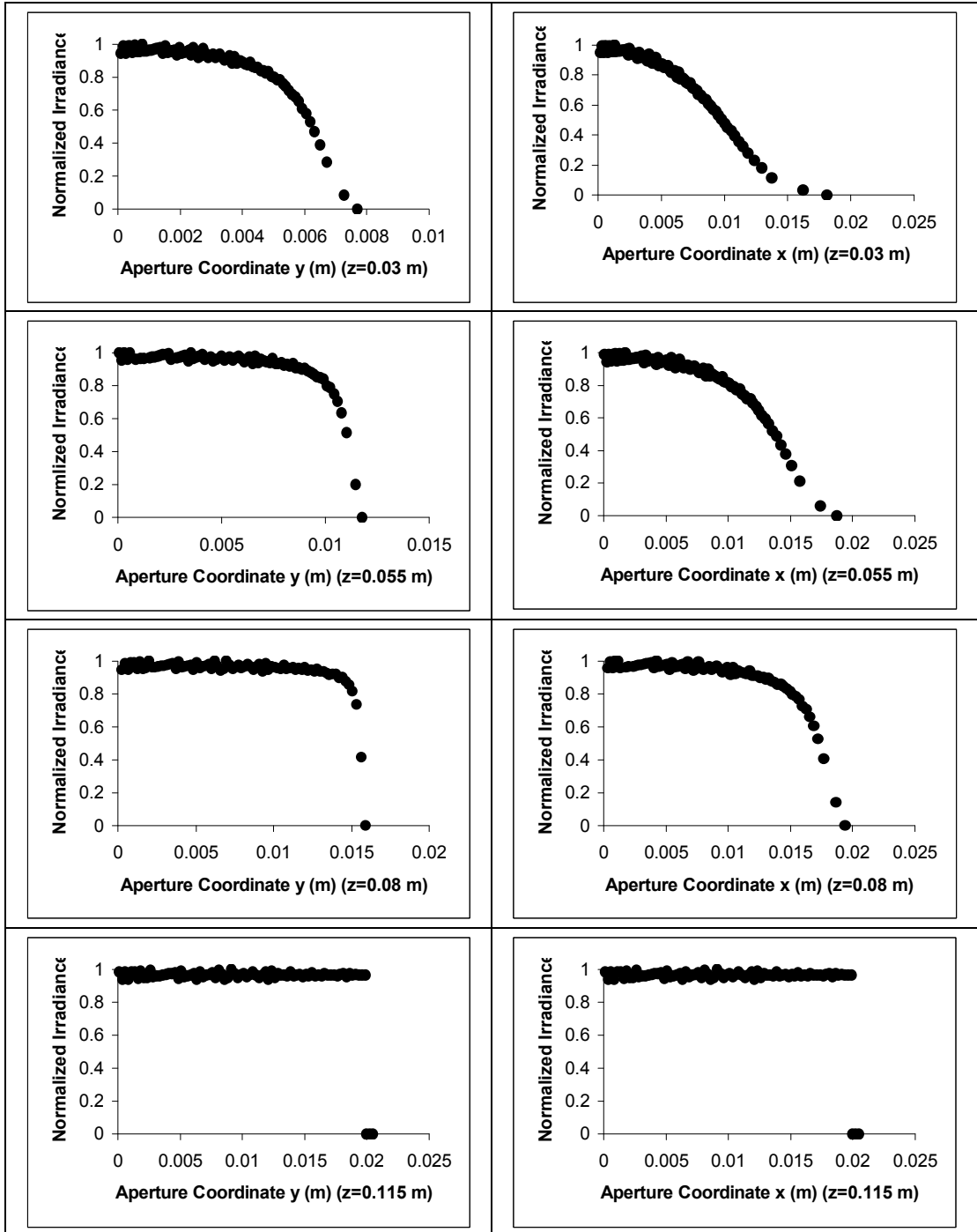
Figure 5.13: Irradiance distributions at five different locations in between the two lenses in the parallel and the perpendicular directions.

As seen in Figure 5.13, the input-plane and the output-plane beam profiles have the same shape as the ones in Figure 5.12b and Figure 5.12c. Figure 5.13 also reveals that the beam changes its profile from Gaussian to uniform faster in the parallel direction (y-z plane) than in the perpendicular direction (x-z plane). Finally, it is seen that the beam profile is transformed to a uniformly distributed beam in both directions at the exit plane of the system.

CHAPTER 6

CONCLUSIONS

Edge-emitting semiconductor lasers have advantages over other lasers (i.e. CO_2 and Nd-YAG) such as low cost, compactness, electronic compatibility, broad range of wavelengths, and high Pulse Repetition Frequency (PRF) values. However, they have different origins and angles of divergence in the two transverse directions, resulting in the inherent astigmatism and elliptical beam shape.

For most LIDAR systems, a circular beam profile is required. Besides, some optical components such as fiber optics require a circular beam profile. In addition to this, LIDARs might be used at high altitudes so that the laser beam is propagated over long distances. This raises the need for collimating the beam to reduce the beam spread. Moreover, the collimated beam allows the receiver to have a low FOV value, which reduces background noise and susceptibility to multiple scattering. In addition to circularization and collimation, the laser beam might be expanded to reduce the beam divergence due to diffraction. This also allows the designed system to achieve eye-safety without significantly reducing the transmitted pulse power.

This dissertation discusses two mirror-based and two lens-based beam shaping optical system designs that circularize, collimate, and expand edge-emitting semiconductor laser beams with elliptical profile for possible application in LIDAR systems.

106

All the design methods are based on geometrical ray optics approach rather than physical optics propagation calculations. It is shown quantitatively that this approach is a good and valid approximation to physical beam propagation for all the designs. In addition, astigmatism in μm levels is neglected since the beam is expanded to cm to m levels and collimated in these designs.

Two examples of mirror-based design methods are developed. The first method uses two cylindrical hyperbolic mirrors to circularize and expand the beam simultaneously. The second one uses two cylindrical parabolic mirrors for the same purpose. The circularized and expanded beam is collimated with a rotationally symmetric parabolic mirror in both methods. The main difference between the two methods is that the first one further increases the beam divergence angle in the parallel transverse direction to be equal to the angle in perpendicular direction while the second one reduces the divergence angle in the perpendicular direction to be equal to the angle in the other direction. The design equations are derived analytically and presented in Section 4.4. A MATLAB code is developed to solve the equations system for the parameters of the mirrors. ZEMAX simulation results are presented in Section 5.1 to analyze the output beam for both design methods. The output beam images, which are derived by physically propagating the beam through the optical systems, reveal that the elliptical input beam is circularized, expanded, and collimated effectively and the results are consistent with the analytical calculations. It is further shown that the second design method provides more satisfactory results than the first one especially for large beam divergence angle values in the perpendicular transverse direction.

Two examples of lens-based design methods are developed. First method consists of two lenses; whereas, the second one is a single-lens system. The design equations are derived analytically and a MATLAB code is used to solve for the unknown quantities of the optical systems. MATLAB and ZEMAX software programs are used to analyze these systems for particular design examples. The output beam images, which are derived by physically propagating the beam through the optical systems, reveal that the elliptical input beam is circularized, expanded, and collimated effectively and the results are only slightly different with the analytical calculations. The author believes that this minor difference is attributed to the ZEMAX software's limitations for highly divergent beams and highly curved surfaces. Regardless of the minor deviations, MATLAB results and ZEMAX results are in agreement. In author's opinion, ZEMAX physical optics propagation results for reflective surfaces are more accurate than for refractive surfaces. Hence, this limitation is negligible for the mirror-based design method results. It is shown that the lens thickness in the second method needs to be increased with the increasing difference of the beam divergence angles and / or increasing final beam diameter, which also increases the overall system size. In this case, first design method becomes a more practical approach.

In addition to high divergence and elliptical beam shape drawback of the edge-emitting semiconductor lasers, Gaussian irradiance distribution is also undesirable for several applications such as display technology, lithography, laser printing, and material processing because these applications require uniform illumination of an extended area. An optical system design method, which utilizes two aspherical lenses to circularize and collimate an edge-emitting semiconductor laser beam and to transform its irradiance

distribution from Gaussian to a uniform-square distribution, is presented in Section 4.6. A square pulse function is chosen as the output beam distribution function for simplicity. The abrupt change in the output irradiance distribution functions (such as in the square pulse function) causes diffraction effects, which are neglected in this chapter. Geometrical optics methods such as ray tracing, conservation of energy within a bundle of rays, and constant optical path length of all rays, are used to design this beam shaper. Results of a particular design example are presented in Section 5.3. A specific optical beam shaping system is designed to circularize, collimate, and expand the beam of an edge-emitting semiconductor laser to a desired diameter and to transform its irradiance distribution from Gaussian to uniform. This is the main difference of this study with the studies that are based on the same beam shaping principle in the literature since most of those studies assume that the input beam is a circular and collimated beam. The distance between the laser source and the vertex of the first surface of the beam shaper is also an unknown quantity and solved for in the design.

To summarize, in this dissertation several optical systems are presented to reshape an edge-emitting semiconductor laser beam as required by a particular application. The main application type that the author concentrates on is LIDAR systems. A coherent Doppler LIDAR system is discussed briefly in section 3.3.2. The detailed design considerations of this and other LIDAR systems are left for future study.

As mentioned in Chapter 2, there is ample room for scientific studies about edge-emitting semiconductor laser-based LIDAR systems. Such LIDAR systems require beam shaping optics design for several applications such as atmospheric studies. Therefore, the specific beam shapers designed for such LIDARs will be a strong contribution to the

scientific community. The discussed systems are developed by solving analytical equations. Another strong contribution of this dissertation is the means that the equations are derived and solved. The design methods will create a guideline for the ones that will work on similar topics. Besides, the author uses ZEMAX software both in design and analysis steps. Therefore, the author presents information about the usage of ZEMAX for similar purposes.

Generally in optics, the spherical surfaces are preferred to manufacture lenses and mirrors due to simplicity. However, the aberrations that these surfaces introduce increase with increasing divergence angles of the laser sources. In order to define the optical surfaces accurately with minimal aberrations, aspheric surfaces are chosen. These surfaces are defined with radius of curvature and conic constant quantities. In order to define these surfaces even more accurately, polynomial deformation terms might be defined. The weakness of using such surfaces is that it is hard to physically manufacture them. However, with advances in optical manufacturing technology, this will not be a problem any more in the near future.

The off-axis mirror systems are comparatively harder to realize in a laboratory environment than the on-axis lens systems due to the probable alignment problems in 3-D space. Besides, those systems can be applied in LRF systems but not in coherent LIDAR systems without modification. Therefore, the first system that the author plans to realize as a future study is the two-lens system. This system, then, will be employed in a coherent Doppler LIDAR system, as discussed in section 3.3.2.

Once, this system and required optics design is accomplished, the next step will be to develop the signal processing unit to produce the LIDAR images of test target objects.

After successful data processing techniques are developed, necessary scanning mechanism is designed depending on the application type, laser type, and system operation altitude.

In conclusion, this dissertation introduces beam shaping optical system design methods to circularize/collimate/expand an elliptically divergent beam of an edge-emitting semiconductor laser and/or to transform such beam's irradiance distribution from Gaussian to uniform.

BIBLIOGRAPHY

[1] A. V. Jelalian, *Laser Radar Systems*, pp. 121-206, Artech House, Massachusetts, 1992.

[2] M. K. Rao and C. C. Goh, "A Low-Cost Near-IR Laser Radar", Photon. Tech. Let., vol. 2, no 9, pp. 683-685, 1990.

[3] S.M. Beck, J.A. Gelbwachs, D.A. Hinkley, D.W. Warren, and J.E. Wessel, "Aerospace applications of optical sensing with lidar**,"** in Proc. IEEE Aerospace Applications Conference, Aspen, CO, vol. 2, pp. 91-96, 1996.

[4] K. Tatsuno and A. Arimoto, "Optical System for Semiconductor Laser", United States Patent # 4564268, 1986.

[5] H. M. Presby and C. R. Giles, "Asymetric Fiber Microlenses for Efficient Coupling to Elliptical Laser Beams", IEEE Photon. Tech. Let., vol. 5, no.2, pp. 184-186, 1993.

[6] S.-Y. Huang and C. Gaebe, "Astigmatic Compensation for an Anamorphic Optical System", United States Patent # 6301059 2001.

[7] J. A. Hoffnagle and C. M. Jefferson, "Design and Performance of A Refractive Optical System That Converts A Gaussian to A Flattop Beam", Appl. Opt., vol. 39, no. 30, pp. 5488- 5499, 2000.

[8] A. B. Gschwendtner, R. C. Harney, and R. J. Hull, "Coherent IR Radar Technology" in *Optical and Laser Remote Sensing*, Springer-Verlag, New York, 1983.

[9] ZEMAX Optical Design program, *User's Guide,* ZEMAX Development Corporation, California, 2004.

[10] www.zemax.com, ZEMAX Development Corporation website

[11] D. C. O'Shea, *Elements of Modern Optical Design*, Wiley, New York, 1985.

[12] A. E. Siegman, *Lasers,* University Science Books, Mill Valley, 1986.

[13] T. Numai, *Fundamentals of Semiconductor Lasers*, Springer, New York, 2004.

[14] K. J. Kuhn, *Laser Engineering*, Prentice Hall, New Jersey, 1998.

[15] C.-L. Chen, *Elements of Optoelectronics And Fiber Optics*, Times Mirror Higher Education Group, Chicago, 1996.

[16] P. W. Milonni and J. H. Eberly, *Lasers*, Wiley, New York, 1988.

[17] http://en.wikipedia.org/wiki/Transverse_mode

[18] P. Hello and C. N. Man, "Design of a Low-Loss Off-Axis Beam Expander", Appl. Opt., vol. 35, no. 15, pp. 2534-2536, 1996.

[19] M. Serkan, H. Kirkici, and H. Cetinkaya, "Off-Axis Mirror Based Optical System Design for Circularization, Collimation, And Expansion of Elliptical Laser Beams", Appl. Opt., vol. 46, no. 22, pp. 5489-5499, 2007.

[20] C. E. Gaebe, S. Huang, K. A. Miller, T. Stanley, and G. T. Wiand, "Cruciform Cylindrical Lens for Elliptical Beam Transformation", United States Patent #5973853, 1999.

[21] K. J. Scheibengraber, "Optical System for Generating Lines of Light Using Crossed Cylindrical Lenses", United States Patent #5095386, 1992.

[22] Z. Xiao-qun, B. N. K. Ann, and K. S. Seong, "Single Aspherical Lens for Deastigmatism, Collimation, and Circularization of A Laser Beam", Appl. Opt., vol. 39, no. 7, pp. 1148-1151, 2000.

[23] M. Serkan and H. Kirkici, "Optical beam Shaping Design Based on Aspherical Lenses for Circularization and Collimation of Elliptical Laser Beams", Appl. Opt., *Accepted to be Published*, 2007.

[24]. H. Hanada, "Beam Shaping Optical System", United States Patent #4318594, 1982.

[25] P. W. Scott and W. H. Southwell, "Reflective Optics for Irradiance Redistribution of Laser Beams: Design", Appl. Opt., vol. 20, no. 9, pp. 1606- 1610,1981.

[26] P. H. Malyak, "Two-Mirror Unobscured Optical System for Reshaping The Irradiance Distribution of A Laser Beam", Appl. Opt., vol. 31, no. 22, pp. 4377-4383, 1992.

[27] D. L. Shealy and S.-H. Chao, "Geometric Optics-Based Design of Laser Beam Shapers", Opt. Eng., vol. 42, no. 11, pp. 3123- 3128, 2003.

[28] P. W. Rhodes and D. L. Shealy, "Refractive Optical Systems for Irradiance Redistribution of Collimated Radiation: Their Design And Analysis", Appl. Opt., vol. 19, no. 20, pp. 3545- 3553, 1980.

[29] J. A. Hoffnagle and C. M. Jefferson, "Beam Shaping with A Plano-Aspheric Lens Pair", Opt. Eng., vol. 42, no. 11, pp. 3090- 3099, 2003.

[30] M. Serkan and H. Kirkici, "Reshaping A Divergent Elliptical Gaussian Laser Beam into A Circular, Collimated, and Uniform Beam with Aspherical Lens Design", *Manuscript under Preparation*, 2007.

[31] D. L. Shealy and J. A. Hoffnagle, "Laser Beam Shaping Profiles And Propagation", Appl. Opt., vol. 45, no. 21, pp. 5118- 5131, 2006.

[32] R. M. Measures, *Laser Remote Sensing*, Wiley, New York, 1984.

[33] J. C. Sentell, "Dual-use DIAL applications and performance prediction," in Proc. SPIE vol. 2271, Industrial Applications of Laser Radar, pp. 2-12, 1994.

[34] http://asd-www.larc.nasa.gov/lidar/concept.html, DIAL Concept Description website

[35] R. M. Hardesty, R. M. Banta, M. J. Post, and W. L. Eberhard, "A decade of atmospheric studies using a pulsed CO_2 Doppler lidar," in Proc. IEEE International Geoscience and Remote Sensing Symposium, Vol. 2, pp. 926-928, 1994.

[36] G. D. Emmitt, "SPARCLE: an approved shuttle mission to demonstrate tropospheric wind sensing using a coherent 2 μm Doppler lidar," in Proc. SPIE vol. 3439, Earth Observing Systems III, pp. 31-38, 1998.

[37] J. W. Bilbro, C. A. Dimarzio, D. Fitzjarrald, S. Johnson, and W. Jones, "Airborne Doppler Lidar Measurements", Appl. Opt., vol. 25, no. 21, pp. 3952- 3960, 1986.

[38] H. W. Mocker and P. E. Bjork, "High Accuracy Laser Doppler Velocimeter Using Stable Long-Wavelength Semiconductor Lasers", Appl. Opt., vol. 28, no. 22, pp. 4914- 4919, 1989.

[39] J. M. Vaughan, R. P. Callan, D. A. Bowdle, and J. Ruthermel, "Spectral Analysis, Digital Integration and Measurement of Low Backscatter in Coherent Laser Radar", Appl. Opt., vol. 28, no. 15, pp. 3008-3014, 1989.

[40] M. J. Post, "Development of Coherent Laser Radar", in Proc. IEEE International Geoscience and Remote Sensing Symposium, vol.2, pp. 923- 925, 1994.

[41] S. W. Henderson, C. P. Hale, J. R. Magee, M. J. Kavaya, and A. V. Huffaker, "Eyesafe Coherent Laser Radar System at 2.1 μm using Tm,Ho:YAG Lasers", Optics Letters, vol. 16, no 10, pp.773-775, 1991.

[42] A. Masdea, G. B. Michelangeli, and A. Cosentino, "Receiver and Transmitter Design Criteria in Coherent Doppler Wind Lidar", in Proc. SPIE vol. 2310, Lidar Techniques for Remote Sensing, pp. 174- 184, 1994.

[43] M. P. McCormick and C. A. Hostetler, "LITE-the first spaceborne lidar," in Proc. IEEE Combined Optical-Microwave Earth and Atmosphere Sensing Symposium, Vol. 3, pp. 163-166, 1995.

114

[44] http://www-lite.larc.nasa.gov , LITE website

[45] A., I. Carswell, "Lidar measurement of clouds" in *Optical and Laser Remote Sensing*, Springer-Verlag, New York, 1983.

[46] W. L. Eberhard, "CO_2 lidar: a somewhat different view of clouds," in Proc. IEEE International Geoscience and Remote Sensing Symposium, vol. 2, pp. 929-931, 1994.

[47] W. L. Eberhard, "CO_2 lidar technique for observing characteristic drop size in water clouds", IEEE Transactions on Geoscience and Remote Sensing, vol. 31, no 1, pp. 56-63, 1993.

[48] N. Takeuchi, H. Shimizu, Y. Sasano, N. Sugimoto, I. Matsui, and H. Nakane, "Wide-Area Air Pollution Measurement by the NIES Large Lidar" in *Optical and Laser Remote Sensing*, Springer-Verlag, New York, 1983.

[49] A.P. Chaikovksy, I.S. Hutko, A.P. Ivanov, F.P. Osipenko, V.N. Shcherbakov, and, S.B. Tauroginskaya, "Studying background and industrial aerosols by multi-wavelength lidar," in Proc. IEEE International Geoscience and Remote Sensing Symposium, vol. 3, pp. 2329-2331, 1995.

[50] A. V. Jelalian, W. H. Keene, and E. F. Pearson, "Tactical and atmospheric coherent laser radar technology" in *Optical and Laser Remote Sensing*, Springer-Verlag, New York, 1983.

[51] M. A. Samuels, S. W. Patterson, J. A. Eppstein, and R. L. Fowler, "Low-cost hand-held lidar for automotive speed detection and law enforcement," in Proc. SPIE vol. 1633, Laser Radar VII: Advanced Technology for Applications, pp. 147-159, 1992.

[52] R. L. Gustavson and T. E. Davis, "Diode laser radar for low-cost weapon guidance," in Proc. SPIE vol. 1633, Laser Radar VII: Advanced Technology for Applications, pp. 21-32, 1992.

[53] A. Samman, L. Rimai, J. R. McBride, R. O. Carter, W. H. Weber, C. Gmachl, F. Capasso, A. L. Hutchinson, D. L. Sivco, and A. Y. Cho, "Potential use of near, mid and far infrared laser diodes in automotive LIDAR applications," in Proc. IEEE Vehicular Technology Conference, vol. 5, pp. 2084-2089, 2000.

[54] K. Takagi, K. Morikawa, T. Ogawa, and M. Saburi, "Road environment recognition using on-vehicle LIDAR," in Proc. IEEE Intelligent Vehicles Symposium, pp. 120-125, 2006.

[55] T. V. Tuong, M. Matsuoka, and F. Yamazaki, "LIDAR-based change detection of buildings in dense urban areas," in Proc. IEEE International Geoscience and Remote Sensing Symposium, vol. 5, pp. 3413-3416, 2004.

[56] V. K. Verma and S. R. Hsu, "3D building detection and modeling from aerial LIDAR data," in Proc. IEEE Computer Vision and Pattern Recognition Conference, vol. 2, pp. 2213-2220, 2006.

[57] C. S. Lin, "Airborne lidar remote sensing of terrain and ocean," in Proc. IEEE International Geoscience and Remote Sensing Symposium, vol. 3, pp. 2316-2318, 1995.

[58] R. A. Smith and G. R. West, "Airborne lidar: a surveying tool for the new millennium," in Proc. IEEE OCEANS Conference, vol. 3, pp. 1290-1299, Sep 1999.

[59] J. M. Wozencraft, "Complete coastal mapping with airborne lidar," in Proc. IEEE OCEANS Conference, vol. 2, pp. 1194-1198, 2002.

[60] M. B. Rivas, J. A. Maslanik, J. G. Sonntag, and P. Axelrad, "Sea ice roughness from airborne LIDAR profiles" IEEE Transactions on Geoscience and Remote Sensing, vol. 44, no 11, pp. 3032-3037, 2006.

[61] F. Stetina, D. S. Friedman, W. B. Krabill, T. D. Kunz, J. M. Hill, D. DiRosa, D. L. Michaels, and J. A. Schmidt, "Progress on the Airborne Lidar Topographic Mapping System (ALTMS) Sensor," in Proc. IEEE International Geoscience and Remote Sensing Symposium, vol. 2, pp. 656-658, 1993.

[62] G. Sun and K. J. Ranson, "Modeling lidar returns from forest canopies", IEEE Transactions on Geoscience and Remote Sensing, vol. 38, no 6, pp. 2617-2626, 2000.

[63] G. Cecchi, M. Bazzani, V. Raimondi, and L. Pantani, "Fluorescence lidar in vegetation remote sensing: system featuresand multiplatform operation," in Proc. IEEE International Geoscience and Remote Sensing Symposium, vol. 1, pp. 637-639, 1994.

[64] M. Lennon, N. Thomas, V. Mariette, S. Babichenko, and G. Mercier, "Operational quantitative mapping of oil pollutions at sea by joint use of an hyperspectral and fluorescence lidar system on-board a fixed wing aircraft," in Proc. IEEE OCEANS Conference, vol. 2, pp. 848-853, 2005.

[65] F. Girard-Ardhuin, G. Mercier, F. Collard, and R. Garello, "Oil slick detection and characterization by satellite and airborne sensors: experimental results with SAR, hyperspectral and lidar data" IEEE Journal of Oceanic Engineering, vol. 30, no. 3, pp. 19-27, 2005.

[66] J. A. Reagan, H. Liu, and J.F. McCalmont, "Laser Diode Based New Generation Lidars", in Proc. IEEE International Geoscience and Remote Sensing Symposium, pp. 1535-1537, 1996.

[67] R. T. Menzies and D. K. Killinger, "IR Lasers Tune In to the Environment", IEEE Circuits and Devices Magazine, vol. 10, no.2, pp.24- 29, 1994.

[68] J. D. Spinhirne, "Micro Pulse Lidar", IEEE Transactions on Geoscience and Remote Sensing, vol. 31, no 1, pp. 48-55, 1993.

[69] J. A. Reagan, "New Generation Lidars to Support Aerosol Radiation / Climate Forcing Studies", in Proc. IEEE International Geoscience and Remote Sensing Symposium, vol. 3, pp. 2313-2315, 1995.

[70] I. Britvitch, K. Deiters, Q. Ingram, A. Kuznetsov, Y. Musienko, D. Renker, S. Reucroft, T. Sakhelashvili, and J. Swain, "Avalanche Photodiodes Now and Possible Developments", Nuclear Instruments and Methods in Physics Research A, vol. 535, no 1-2, pp. 523-527, 2004.

[71] C. Niclass, A. Rochas, P. A. Besse, and E. Charbon, "Design and Characterization of a CMOS 3-D Image Sensor Based on Single Photon Avalanche Diodes", IEEE Journal of Solid-State Circuits, vol. 40, no. 9, pp. 1847-1854, 2005.

[72] M. Henriksson, "Detection Probabilities for Photon-Counting Avalanche Photodiodes Applied to A Laser Radar System", Appl. Opt., vol. 44, no. 24, pp. 5140-5147, 2005.

[73] W. J. Kindt, N. H. Shahrjerdy, and H. W. van Zeijl, "A Silicon Avalanche Photodiode for Single Optical Photon Counting in The Geiger Mode", Sensors and Actuators A, vol. 60, no. 1-3, pp.98-102, 1997.

[74] R. M. Heinrichs, B. F. Aull, D. G. Fouche, R. Hatch, A. K. McIntosh, R. M. Marino, M. E. O'Brien, G. Rowe, and J. J. Zayhowski, "3-D Laser Radar Development with Arrays of Photon-Counting Detectors", IEEE Conference on Lasers and Electro-Optics, CTUK1, 2003.

[75] F. M. Dickey, S. C. Holswade, and D. L. Shealy, *Laser Beam Shaping Applications* CRC Press, Inc., 2006.

[76] F. M. Dickey and S. C. Holswade, *Laser Beam Shaping Theory and Techniques*, Marcel Dekker, New York, 2000.

[77] S. A. Self, "Focusing of Spherical Gaussian Beams", Applied Optics, vol. 22, no 5, pp. 658-661, 1983.

[78] E. Hecht, *Optics*, Addison-Wesley, Reading, 1988.

[79] R. R. Shannon, "Aspheric Surfaces", Appl. Opt. and Opt. Eng., vol. 8, pp. 55-85, 1980.

[80] C. H. Edwards and D. E. Penney, Calculus and Analytic Geometry, pp. 504-548, Prentice Hall, Inc., New Jersey, 1988.

[81] M. Geary, Introduction to Lens Design: With Practical ZEMAX Examples, Willmann-Bell, 2002.

[82] http://www.zemax.com/kb, ZEMAX Users' Knowledge Base website

[83] K. Moore, "What is a Point Spread Function", *ZEMAX Users' Knowledge Base*, 2005.

[84] A. Locke, "Exploring Physical Opics Propagation in ZEMAX", *ZEMAX Users' Knowledge Base*, 2005.

[85] A. Locke, "Exploring Non-Sequential Mode in ZEMAX", *ZEMAX Users' Knowledge Base*, 2005.

APPENDIX

ZEMAX is a software program, which can be used to design and analyze optical systems. This appendix section is prepared as a ZEMAX tutorial for the first time users based on the author's experiences and on [82- 84]. It does not cover the details for designing and analyzing an optical system or all of the tools and capabilities of ZEMAX. For such purposes, the reader is encouraged to refer to the ZEMAX Manual [9]. Another source to get used to design and analysis with ZEMAX is the ZEMAX Users' Knowledge Base [82]. This resource contains articles written by ZEMAX specialists, instructors, and users.

This tutorial is based on Sequential mode ZEMAX. In sequential mode, rays are traced through a sequence of surfaces from the object surface to the image surface in the defined order and each ray hits a surface only once. Non-sequential ZEMAX is out of the scope of this tutorial and introductory information about this mode can be found in [9, 85].

Entering the System and Surface Parameters:

ZEMAX uses a spreadsheet format called the Lens Data Editor (LDE). Most of the surface parameters are entered in this editor. The main parameters, as seen in Figure A.1, are:
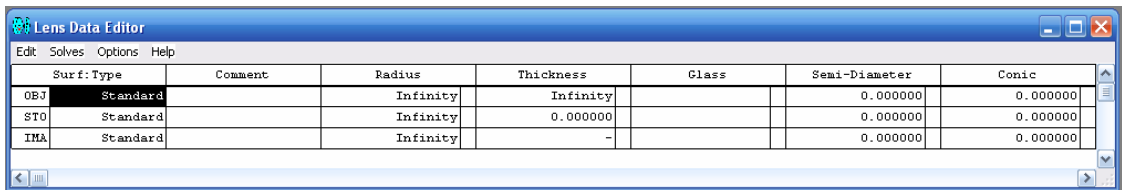
Surf: Type - the type of surface

Radius - surface radius of curvature in lens units

Thickness - thickness between the vertex of the currently entered surface to the vertex of the following surface in lens units

Glass - the material type (glass type, MIRROR, etc.) between the vertex of the currently entered surface and the vertex of the following surface

Semi-Diameter - size of the surface aperture in lens units

Conic - the conic constant of the surface (zero for spherical surfaces)

Figure A.1: Lens Data Editor display

By default, three surfaces exist in the LDE window: the object surface (OBJ), stop surface (STO), and image surface (IMA).

It is a better approach to enter the system parameters before entering any surface parameter. The first system parameter is the system aperture that defines the size of the beam that will be propagated through the system. System aperture can be defined by different aperture types: Entrance Pupil Diameter (EPD), Image Space F/#, Object Space NA, Float By Stop Size, Paraxial Working F/#, Object Cone Angle. The most common one is the EPD, which is the diameter of the pupil in lens units as seen from object space.

The second issue that needs to be addressed is the illumination of the entrance pupil. By default, the entrance pupil is always illuminated uniformly. This can be changed using the Apodization Type. For instance, Gaussian apodization imparts an amplitude variation over the pupil that is Gaussian in form. The Apodization Factor refers to the

120

rate of decrease of the beam amplitude as a function of radial pupil coordinate and the beam amplitude is normalized to unity at the center of the pupil.

Analysis of systems that collimates the input beam needs special attention. If Afocal Image Space box is checked, ZEMAX will perform most analysis features in a manner appropriate for optical systems with output beams in image space that are nominally collimated.

Another system parameter that needs to be set is the field of view value. The field of view is set on the Field Data dialog box. The default field entry is on-axis only. ZEMAX supports 4 different models for defining fields: Angle, Object Height, Paraxial Image Height, Real Image Height. The most common one is Angle that is entered in degrees unit that the chief ray makes with respect to the object space z-axis. The wavelengths are set on the Wavelength Data dialog box.

Lens unit must also be chosen before entering the parameters. There are four choices for lens units in ZEMAX: millimeters, centimeters, inches, or meters. Lens unit defines the unit of measure for dimensions in most of the spreadsheet editors. These dimensions apply to data such as radii, thickness, entrance pupil diameters, and most other parameters in ZEMAX. Afocal mode units may be microradians, milliradians, radians, arc-seconds (1/3600 of a degree), arc-minutes (1/60 of a degree), or degrees.

Once the system settings have been defined, surface parameters can be entered into the LDE. Each row in the LDE contains data that belong to a single surface. Stop Surface can be chosen later by checking the Make Surface Stop box in the Surface Properties dialogue box, as seen in Figure A.2. It is important to define the stop surface

such that the entrance pupil is on the same axis as the object surface. This is specifically of importance when designing off-axis systems.
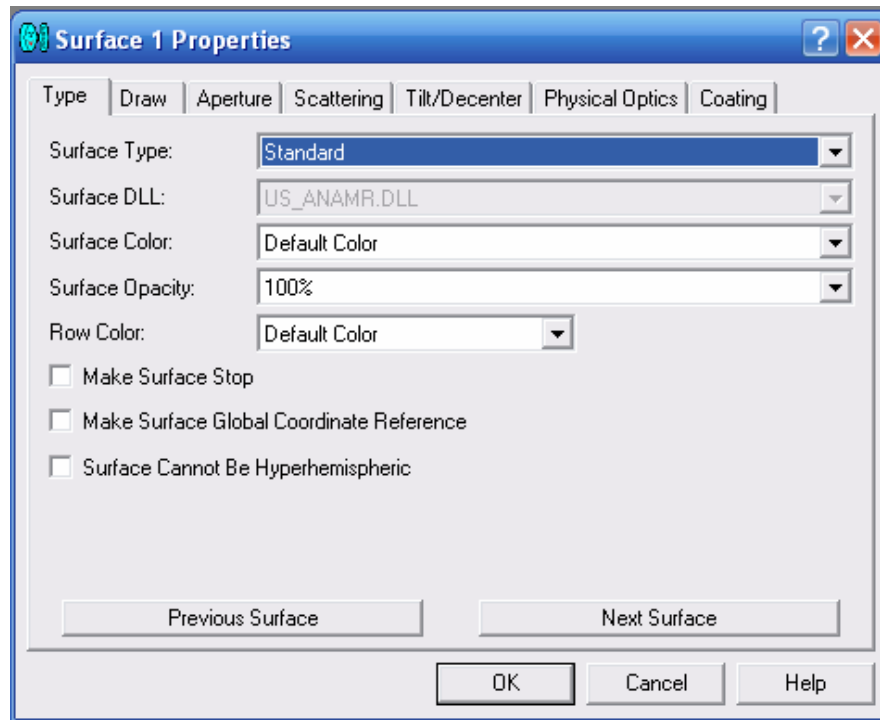

Figure A.2: Surface Properties dialogue box display

Surface properties can be set by double clicking on the left most column of a surface row, which invokes the Surface Properties dialogue box, as seen in Figure A.2. The previous/next surface buttons in this box allow rapid navigation through all surfaces.

An aperture on a surface can be defined using the Aperture tab in this dialogue box. Surface apertures are used to account for the effects of vignetting. The supported types of surface apertures in ZEMAX are: no aperture, circular aperture, circular obscuration, rectangular aperture, rectangular obscuration, elliptical aperture, elliptical obscuration, spider obscuration, user defined aperture, user defined obscuration, and floating aperture. The aperture and obscuration types define regions, which pass or stop rays, respectively.

More than one aperture may be described at a given optical element by inserting a dummy surface with zero thickness at the desired location, and then setting additional apertures on that surface. This is useful for constructing complex apertures. For instance, a circular aperture defines an annular region, which vignettes all rays striking the surface inside of the minimum radius, and outside of the maximum radius. If a ray is between the minimum and maximum radii, then the ray will be allowed to proceed. A circular obscuration is the complement of the circular aperture such that if a ray is between the minimum and maximum radii, then the ray will not be allowed to proceed.

After setting the surface specific settings, glass type for optical components such as lenses and mirrors must be entered. ZEMAX automatically recognizes the entered glass type as one of the many glasses that are compiled into the built-in Glass Catalog. For mirrors, glass type is entered as MIRROR.

A Standard surface can be a plane, spherical, or conic aspheric surface. The only parameters required besides the glass type are a radius (infinite value corresponds to a planar surface), a thickness, and a conic constant (zero value corresponds to a sphere). Other surface types use these same basic data, as well as other values. For instance, the Even Asphere surface uses all the Standard surface parameters with additional values describing the coefficients of a polynomial used to represent the deformation terms of the surface. These values are called Parameters. Parameter meaning changes depending upon the surface type selected. Another example is the Biconic surface. This surface has different refractive power values in the two transverse directions. For this surface, entered radius and conic constant parameters are designated values for the y direction. Radius and conic constant values for the x direction are entered in the Parameter 1 and

Parameter 2 boxes. Some surfaces such as the Binary Optic 1 surface type cannot be described by only a few parameter values. This surface type requires up to several hundred additional parameters. For such surfaces, a separate editor is used for the extra data values. The extra data meaning is also different for each surface type.

Basic Analysis Tools:

ZEMAX has various analysis tools. The ones that will briefly be covered in this tutorial are: 3D Layout diagram, Spot diagram, FFT PSF, and Physical Optics Propagation tools.

3D Layout: To create the 3D Layout, ZEMAX projects the 3D coordinates of the rotated optical model onto the 2D plane of the plot. Conceptually, the optical model is first rendered in an unrotated 3D space, with +z oriented to the right, +y up, and +x away from the viewer into the page. The coordinates and orientations of all surfaces and objects are defined by the Global Coordinate Reference Surface. Global Reference Surface is chosen by checking the Make Surface Global Coordinate Reference box in the Surface Properties dialogue box. This 3D model is then rotated by the Rotation About X, Y, and Z values specified in the settings. The resulting 3D model is then projected onto a 2D plane. 3D Layout settings are specified with the dialogue box, seen in Figure A.3.

Ray pattern can be chosen as XY fan, X fan, Y fan, Ring, List, Random or Grid. Here with the List choice, a pre-defined set of rays are traced through the system. These rays can be defined with a notepad file in the main ZEMAX directory called "RAYLIST.txt". Some of the rays might vignet while propagating through the system.

These might be omitted in the layout by checking the Delete Vignetted box. Number of rays that will be traced is also chosen in the settings menu.

Spot Diagram: The spot diagram reveals information about the aberrations of the system imaging a point source. ZEMAX launches several rays from a point source, traces them through the optical system, and plots the (x, y) coordinates of all the rays relative to some common reference. If no aberrations are present, the image of the point source also appears as a perfect image point. The spot diagram is a collection of points, with each point representing a single ray. There is no interaction or interference between the rays. Therefore, the spot diagram is very effective at showing the effects of the geometric or ray aberrations.
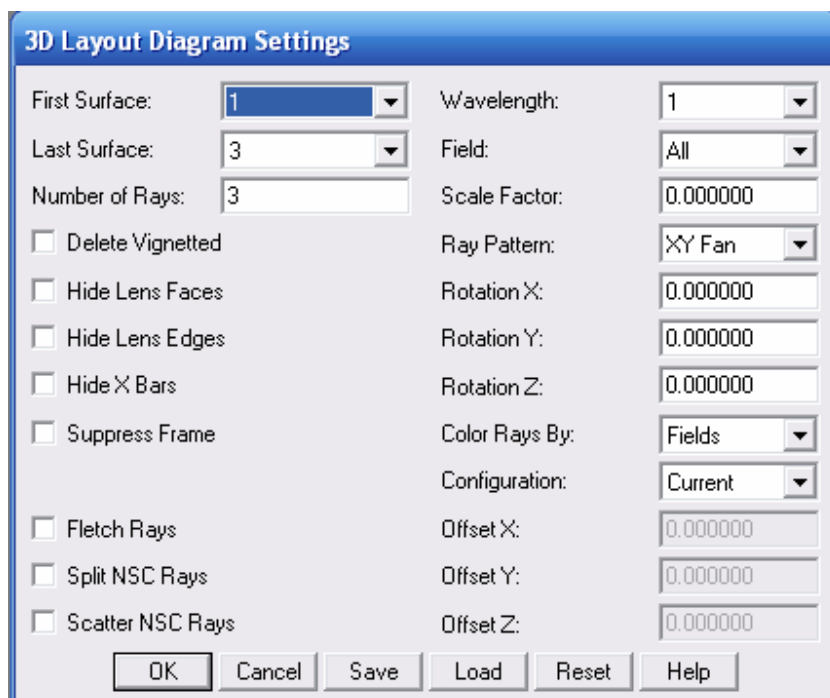

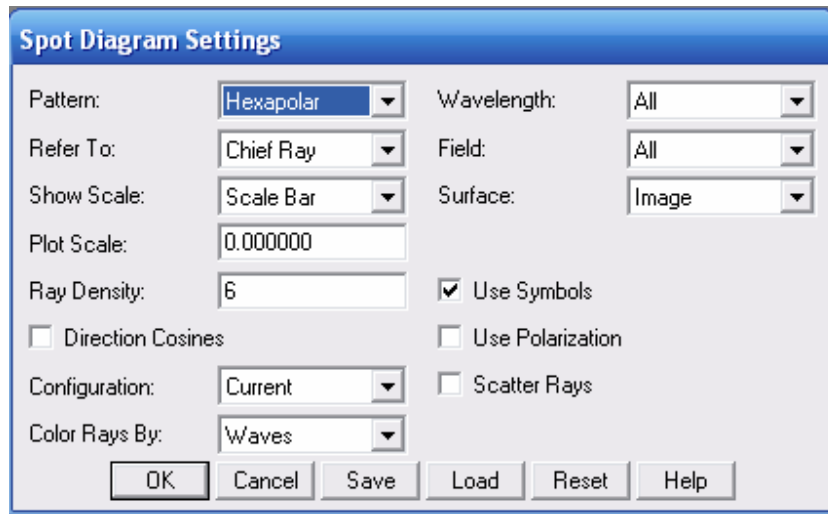Figure A.3: 3D Layout Diagram Settings dialogue box display

Figure A.4: Spot Diagram Settings dialogue box display

The pattern of the traced rays and the ray density can be chosen in the Settings Dialogue box, as seen in Figure A.4. The pattern may be either hexapolar, square, or dithered. These terms refer to the pattern of rays as they appear in a pupil plane. There is no "best" pattern to use since each shows a different character of the spot diagram. The ray density specifies the number of hexapolar rings to be traced if a hexapolar or dithered pattern is selected, or the number of rays across the width and height if a rectangular pattern is selected.

The GEO spot radius listed on the plot for each field point is the distance from the reference point (which is either the chief ray at the primary wavelength, the centroid of all the rays traced, or the middle of the spot cluster) to the ray, which is farthest away from the reference point. On the other hand, the RMS spot radius is the root-mean-square radial size. The distance between each ray and the reference point is squared, and averaged over all the rays, and then the square root is taken. The RMS spot radius gives a rough idea of the spread of the rays, since it depends upon every ray. The GEO spot

radius only gives information about the one ray, which is farthest from the reference point.

FFT PSF: The PSF of an optical system is the irradiance distribution that results from a point source. Aberrations and diffraction effects caused by truncation spread the image of this point source. The FFT decomposes a spatial distribution into a frequency domain distribution. A grid of rays is traced from the source point to the exit pupil [83]. For each ray, the amplitude and optical path difference is used to compute the complex amplitude of a point on the wavefront grid at the exit pupil. The FFT of this grid, appropriately scaled, is then squared to yield the real valued PSF. Settings of this tool are set in the dialogue box, as seen in Figure A.5.
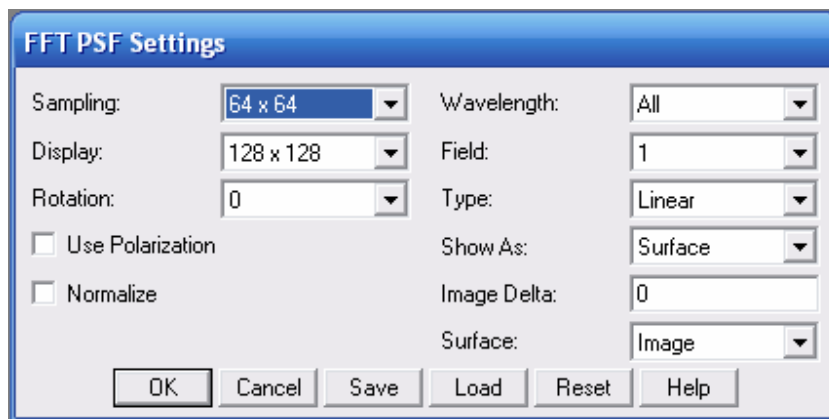

Figure A.5: FFT PSF Settings dialogue box display

The size of the ray grid used to sample the pupil is set with Sampling value. The Display size indicates what portion of the computed data will be drawn when a graphic display is generated. The Display grid can be any size from 32 x 32 up to twice the Sampling grid size. Smaller Display sizes will show less data, but at higher magnification for better visibility. The Image Delta can be selected manually if a different sampling distance is required. If the Image Delta is zero, ZEMAX uses the

default spacing and sampling grids. If the Image Delta is greater than zero, then ZEMAX scales the pupil sampling to yield the desired Image Delta size.

Physical Optics Propagation: Geometrical ray tracing is an incomplete description of light propagation since propagation of the light is coherent [84]. Geometrical ray tracing cannot model the interference of the rays and the diffraction effects. Rays propagate along straight lines without interfering with one another; whereas; wavefronts propagate while coherently interfering with themselves. ZEMAX has some ray based diffraction computations, such as the diffraction MTF or PSF. However, these diffraction computations make a simplifying approximation: that all the important diffraction effects occur going from the exit pupil to the image. This is sometimes called the "single step" approximation. Geometrical optics and the single step approximation work quite well for the majority of traditional optical designs, where the beam is not near focus anywhere except the final image. However, this model does not work accurately for several important cases:

- When the beam comes to an intermediate focus, especially near optics that truncate the beam (rays by themselves do not predict the correct distribution near focus).

- When the diffraction effects far from focus are of interest (rays remain uniform in amplitude and phase, wavefronts develop amplitude and phase structure).

- When the propagation length is long and the beam is nearly collimated (collimated rays will remain collimated over any distance, real beams diffract and spread).

With Physical Optics Propagation tool, the wavefront of a beam is modeled using an array of points. Each point in the array stores complex amplitude information about the beam. The analysis computes the beam irradiance or phase on a plane tangent to the chief ray at the point where the chief ray intercepts the surface. The data is shown after the beam refracts into, or reflects from, the end surface. To propagate the beam from one surface to another, either a Fresnel diffraction propagation or an angular spectrum propagation algorithm is used. ZEMAX automatically chooses the algorithm that yields the highest numerical accuracy. Beams in ZEMAX are always centered on the chief ray for the selected field and wavelength.

Parameters necessary to use this tool are set in the POP Settings dialogue box, as seen in Figure A.6. X-Width and Y-Width values specify the initial width in lens units, whereas X-Sampling and Y-Sampling values specify the number of points used to sample the beam. Sampling system of this tool uses a constant spacing near the waist, and a linearly scaled spacing far from the waist. Although the total number of array points remains constant, the array size and point spacings change as the beam propagates. If the array width is very large at the beam waist relative to the waist size, then there are relatively few points across the beam waist. This results in a smaller array size far from the waist, with a relatively large number of points across the beam size. On the contrary, if the array size is small at the waist, the array size grows large compared to the beam far from the waist, leaving few sample points to represent the beam. This inverse relationship is a necessary but frequently inconvenient product of the Fourier transform theory used to model the diffraction. Therefore width and sample values must be carefully adjusted as the beam propagates through the system. It must be checked that

the beam is not under-sampled at any surface. If this is the case, width and sampling values can be changed at appropriate intermediate surfaces in order to provide sufficient data points.
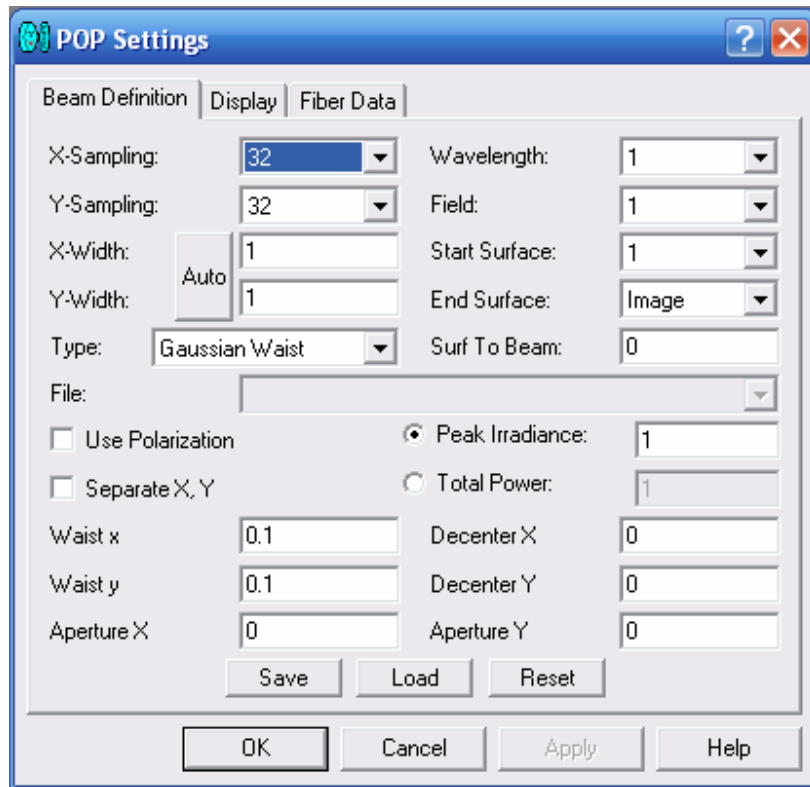

Figure A.6: Physical Optics Propagation Settings dialogue box display

For rotationally symmetric systems, a single rotationally symmetric pilot beam and propagation method is appropriate. When the beam is astigmatic or anamorphic, and/or the optical components are cylindrical or toroidal, then the beam must be separated in the X and Y propagation. Separation of X and Y direction propagation is accomplished by checking Separate X, Y box in the Settings dialogue box.

The initial beam may be defined using any of these options:

Gaussian Waist - Beam waist radius and decenter values are entered.

Gaussian Angle – Beam far-field half divergence angle and decenter values are entered.

Gaussian Size+Angle – Beam size at any arbitrary point, far-field half divergence angle and decenter values are entered.

Top Hat – Beam waist radius and decenter values are entered. The irradiance distribution is uniform rather than Gaussian.

User defined initial beam profiles are also possible.

In this tutorial, a quick start tutorial for ZEMAX software program is presented. Basic analysis tools are also explained briefly. This tutorial is prepared based on the author's experiences using ZEMAX and [82- 84].